Title

An Isogeometric Analysis Framework for Progressive Damage Modeling of Multi-Layer Composite Materials

Permalink

https://escholarship.org/uc/item/0774d7kh

Author

Pigazzini, Marco Simone

Publication Date

2018

UNIVERSITY OF CALIFORNIA SAN DIEGO

An Isogeometric Analysis Framework for Progressive Damage Modeling of Multi-Layer Composite Materials

A dissertation submitted in partial satisfaction of the
requirements for the degree
Doctor of Philosophy

in

Structural Engineering

by

Marco Simone Pigazzini

Committee in charge:

Professor Yuri Bazilevs, Chair
Professor Jiun–Shyan Chen
Professor Hyonny Kim
Professor Pui–Shum Benson Shing
Professor Frank E. Talke

2018

The dissertation of Marco Simone Pigazzini is approved, and it is acceptable in quality and form for publication on microfilm and electronically:

Chair

University of California San Diego

2018

DEDICATION

To Claudio and Milena, my parents. Because I am nothing more than what you taught me. (Plus a good amount of perseverance).

EPIGRAPH

Ora tu pensa: un pianoforte.

I tasti iniziano. I tasti finiscono.

Tu sai che sono 88, su questo nessuno può fregarti.

Non sono infiniti, loro. Tu, sei infinito, e dentro quei tasti, infinita è la musica che puoi fare.

—Alessandro Baricco

Novecento: Un monologo teatrale

Adapted translation from Italian:

Now, think about this: a piano.

The keyboard starts. And it ends.

You know that there are 88 keys, no-one can fool you on this.

The keyboard is not infinite. You are infinite, and with those keys you can play infinite music.

TABLE OF CONTENTS

LIST OF FIGURES

LIST OF TABLES

ACKNOWLEDGEMENTS

Personal

I want to start by saying that an additional dissertation would probably be required in order to properly acknowledge all the persons that, through all these years, helped and supported me. I cannot say where I would be without you, but for sure I know that I would not be here. And for this I will always be grateful. To *ANY* of you.

I will never be thankful enough to my parents, *Claudio* and *Milena*, who have always supported my decisions and taught me that sacrifice and perseverance are the key ingredients to achieve almost anything in life. Without you, I would not be the person that I am proud to be.

I also would like to express my sincere gratitude to my Advisor, Professor *Yuri Bazilevs*, for being an exceptional mentor and a role model for professional excellence. Since the very first day I began to work with him, I felt inspired and pushed to give always the best.

I want to acknowledge all the members of my doctoral committee, professors *Jiun–Shyan Chen, Pui–Shum Benson Shing* and *Frank E. Talke*, for their support and guidance. I want to express my gratitude in particular to Professor *Hyonny Kim*, who has been a second Advisor to me, for providing priceless mentorship and expertise during these years.

Of course, research is a team-work, and through these years several people helped and guided me while working toward common results. I want to express my sincere gratitude to *Andrew Ellison*, for providing exceptional support to my work, and to *Dennis van Iersel*, for his precious help and collaboration. I really want to thank all the current and past members of our research group, for sharing difficulties and, most of all, for sharing great achievements. Thank you to *Artem Korobenko, Georgios Moutsanidis, Jinhui Yan* and *Xiaowei Deng*. A special thank to *David Kamensky* for being an exceptional mentor.

My first thought in the morning and the last one at night goes to my girlfriend *Liz*, with whom I shared the most beautiful memories. I am thankful to have her in my life, thankful for making every day a better day.

And finally, I cannot express how thankful I am to all my friends. Starting from Cinghia (*Riccardo*) and Eggio (*Claudio*), with whom I built a friendship that has been lasting for almost twenty years and it is still growing. I want to thank all the friends I met in San Diego for being like a family to me. So I want to express my gratitude, in mixed order, to Marianz (*Stefano*), Ross (*Lorenzo*), Sabba (*Riccardo*), Tosone (*Simone*), Frat (*Francesco*), Cugnetto (*Andrea*), Franca (*Francesca*), Belli (*Martina*) and Mulas (*Francesca*), Pasito (*Marco*), *Pardis*, *Gloria*, *Giorgio*, *Christian*, *Andreas*, *Arpit*. A special thank to all the people from the SME building for brighting up long working days: *Leticia*, *Ritvik*, *Mike*, *Morgan*, *Ashish*, *Ernesto*, *Ricardo*, *Konstantinos*. A big thank also to *Yvonne* and *Lindsay* for the countless times they helped me.

Many friends I met along the way, so I want to apologize if I forgot to mention anyone. I will always be grateful to any of you.

Co-authors of published material and publishers

Chapters of this dissertation represent and edited reprint, or copy, of material that has already been published or, by the time this dissertation has been drafted, is in preparation for submission to a peer-reviewed journal.
Chapter 1 is, in full, an edited reprint of the material as it appears in:

- *"A new multi-layer approach for progressive damage simulation in composite laminates based on isogeometric analysis and Kirchhoff–Love shells. Part I: basic theory and modeling of delamination and transverse shear"*, published on-line in *"Computational Mechanics"* on November 30th 2017 and co-authored by *Marco S. Pigazzini, Yuri Bazilevs, Andrew C. Ellison, and Hyonny Kim*. This article is currently in press. The author of this dissertation *(Marco S. Pigazzini)* is one of the primary investigators and authors of this paper.
- *"A new multi-layer approach for progressive damage simulation in composite laminates based on isogeometric analysis and Kirchhoff–Love shells. Part II: impact modeling"*, published on-line in *"Computational Mechanics"* on November 24th 2017 and co-authored by *Marco S. Pigazzini, Yuri Bazilevs, Andrew C. Ellison, and Hyonny Kim*. This article is currently in press. The author of this dissertation *(Marco S. Pigazzini)* is the primary investigator and author of this paper.
- *Isogeometric analysis for simulation of progressive damage in composite laminates*, published on-line on April 22nd 2018 in *Journal of Composite Materials* and co-authored by *Marco S. Pigazzini, Yuri Bazilevs, Andrew C. Ellison, and Hyonny Kim*. This article is currently in press. The author of this dissertation *(Marco S. Pigazzini)* is the primary investigator and author of this paper.
- *"Gradient-enhanced damage modeling in Kirchhoff–Love shells: Application to isogeometric analysis of composite laminates"*. This manuscript is in preparation and is co-authored by *Marco S. Pigazzini, David Kamensky, Dennis A. P. van Iersel, Joris J.C. Remmers, and Yuri Bazilevs*. The author of this dissertation *(Marco S. Pigazzini)* is the primary investigator and author of this paper.

Chapter 2 is, in part, an edited reprint of the material as it appears in:

- *"A new multi-layer approach for progressive damage simulation in composite laminates based on isogeometric analysis and Kirchhoff–Love shells. Part I: basic theory and modeling of delamination and transverse shear"*, published on-line in *"Computational Mechanics"* on November 30th, 2017 and co-authored by *Marco S. Pigazzini, Yuri Bazilevs, Andrew C. Ellison, and Hyonny Kim*. This article is currently in press. The author of this dissertation *(Marco S. Pigazzini)* is one of the primary investigators and authors of this paper.
- *"A new multi-layer approach for progressive damage simulation in composite laminates based on isogeometric analysis and Kirchhoff–Love shells. Part II: impact modeling"*, published on-line in *"Computational Mechanics"* on November 24th, 2017 and co-authored by *Marco S. Pigazzini, Yuri Bazilevs, Andrew C. Ellison, and Hyonny Kim*. This article is currently in press. The author of this dissertation *(Marco S. Pigazzini)* is the primary investigator and author of this paper.

Chapter 3 is, in full, an edited reprint of the material as it appears in:

- *"A new multi-layer approach for progressive damage simulation in composite laminates based on isogeometric analysis and Kirchhoff–Love shells. Part I: basic theory and modeling of delamination and transverse shear"*, published on-line in *"Computational Mechanics"* on November 30th 2017 and co-authored by *Marco S. Pigazzini, Yuri Bazilevs, Andrew C. Ellison, and Hyonny Kim*. This article is currently in press. The author of this dissertation *(Marco S. Pigazzini)* is one of the primary investigators and authors of this paper.
- *"A new multi-layer approach for progressive damage simulation in composite laminates based on isogeometric analysis and Kirchhoff–Love shells. Part II: impact modeling"*, published on-line in *"Computational Mechanics"* on November 24th 2017 and co-authored by *Marco S. Pigazzini, Yuri Bazilevs, Andrew C. Ellison, and Hyonny Kim*. This article is currently in press. The author of this dissertation *(Marco S. Pigazzini)* is the primary investigator and author of this paper.

Chapter 4 is, in full, an edited reprint of the material as it appears in:

- *“A new multi-layer approach for progressive damage simulation in composite laminates based on isogeometric analysis and Kirchhoff–Love shells. Part I: basic theory and modeling of delamination and transverse shear”*, published on-line in *“Computational Mechanics”* on November 30th 2017 and co-authored by *Marco S. Pigazzini, Yuri Bazilevs, Andrew C. Ellison, and Hyonny Kim*. This article is currently in press. The author of this dissertation *(Marco S. Pigazzini)* is one of the primary investigators and authors of this paper.

- *“A new multi-layer approach for progressive damage simulation in composite laminates based on isogeometric analysis and Kirchhoff–Love shells. Part II: impact modeling”*, published on-line in *“Computational Mechanics”* on November 24th 2017 and co-authored by *Marco S. Pigazzini, Yuri Bazilevs, Andrew C. Ellison, and Hyonny Kim*. This article is currently in press. The author of this dissertation *(Marco S. Pigazzini)* is the primary investigator and author of this paper.

- *Isogeometric analysis for simulation of progressive damage in composite laminates*, published on-line on April 22nd 2018 in *Journal of Composite Materials* and co-authored by *Marco S. Pigazzini, Yuri Bazilevs, Andrew C. Ellison, and Hyonny Kim*. This article is currently in press. The author of this dissertation *(Marco S. Pigazzini)* is the primary investigator and author of this paper.

Chapter 5 is, in full, an edited copy of material included in the manuscript in preparation: *“Gradient-enhanced damage modeling in Kirchhoff–Love shells: Application to isogeometric analysis of composite laminates”*. This manuscript is in preparation and is co-authored by *Marco S. Pigazzini, David Kamensky, Dennis A. P. van Iersel, Joris J.C. Remmers, and Yuri Bazilevs*. The author of this dissertation *(Marco S. Pigazzini)* is the primary investigator and author of this paper.

Funding

The development of the multi-layer model presented in Chapter 2 and 3 was supported by NASA Advanced Composites Project No. 15-ACP1-0021. The co-authors of the articles [14, 84, 85] and I thank Dr. F. Leone, Dr. C. Rose, and Dr. C. Davila from NASA Langley Research Center for their valuable comments and suggestions. The co-authors and I would like to thank Mr. W. Jackson of NASA Langley for providing the CT scan data used in Chapter 4.

The research related to the LCAAT UAV prototype, presented in Chapter 4, was supported by the AFOSR within the Dynamic Data Driven Application System project, Award No. FA9550-16-1-0131. The co-authors of the article [85] and I thank Dr. E. Blasch and Dr. F. Darema for the their support. I want to express out gratitude to C. Kays of Aurora Flight Sciences for providing technical support in the development of the UAV structural model. Finally, I would like to thank Prof. A. Korobenko at the University of Calgary, Canada, for providing the exterior CAD model of the LCAAT UAV prototype.

VITA

2009	Laurea (B. S.) in Aerospace Engineering Polytechnic University of Milan, Milan, Italy
2012	Laurea Magistrale (M. S.) in Aeronautical Engineering Polytechnic University of Milan, Milan, Italy
2014	M. S. in Structural Engineering University of California San Diego, La Jolla, CA, USA
2014–2017	Graduate Teaching Assistant University of California San Diego, La Jolla, CA, USA
2018	Ph. D. in Structural Engineering University of California San Diego, La Jolla, CA, USA

PUBLICATIONS

Marco S. Pigazzini, Yuri Bazilevs, Andrew C. Ellison, and Hyonny Kim; Isogeometric analysis for simulation of progressive damage in composite laminates, *Journal of Composite Materials*, 2018, In press.

Marco S. Pigazzini, Yuri Bazilevs, Andrew C. Ellison, and Hyonny Kim; A new multi-layer approach for progressive damage simulation in composite laminates based on isogeometric analysis and Kirchhoff–Love shells. Part II: impact modeling, *Computational Mechanics*, 2017, In press.

Marco S. Pigazzini, Yuri Bazilevs, Andrew C. Ellison, and Hyonny Kim; A new multi-layer approach for progressive damage simulation in composite laminates based on isogeometric analysis and Kirchhoff–Love shells. Part I: basic theory and modeling of delamination and transverse shear, *Computational Mechanics*, 2017, In press.

Chiara Bisagni, and Marco S. Pigazzini; Modelling strategies for numerical simulation of aircraft ditching, *International Journal of Crashworthiness*, 2017, In press.

Michael C. H. Wu, David Kamensky, Chenglong Wang, Austin J. Herrema, Fei Xu, Marco S. Pigazzini, Aekaansh Verma, Alison L. Marsden, Yuri Bazilevs Yuri, and Ming-Chen Hsu; Optimizing fluid-structure interaction systems with immersogeometric analysis and surrogate modeling: Application to a hydraulic arresting gear, *Computer Methods in Applied Mechanics and Engineering*, 316:668–693, 2017.

Marco S. Pigazzini, and Chiara Bisagni; Modeling and testing of a weft knitted textile composite, *Tesi di Laurea Magistrale (M. S. Thesis)*, (2012)

ABSTRACT OF THE DISSERTATION

An Isogeometric Analysis Framework for Progressive Damage Modeling of Multi-Layer Composite Materials

by

Marco Simone Pigazzini

Doctor of Philosophy in Structural Engineering

University of California San Diego, 2018

Professor Yuri Bazilevs, Chair

Fiber-reinforced composite materials have become increasingly popular in the past few decades for lightweight applications, in particular in the aerospace industry where high strength-to-weight and high stiffness-to-weight ratio are considered key design parameters. At the same time, new computational technologies are required to support the design process of increasingly complex structural components and to predict damage growth under non-standard loading conditions. However, the development of accurate and computationally efficient analysis tools, capable of predicting the response of laminated composite structures from the elastic regime to the failure point and beyond, is a complex task. Difficulties stem from the inherent heterogeneous nature of fiber-reinforced polymer composite materials and from their multi-modal failure mechanisms. Composite structures optimized for low weight applications are often laminates, consisting of several layers of fiber-reinforced material, called laminae, bonded together. Intra-laminar damage may occur within a given lamina, and inter-laminar damage, or delamination, may occur when bonds between laminae break down. The unique challenges associated with modeling damage in these structures may be addressed by means of thin-shell formulations which is naturally developed in the context of Isogeometric Analysis.

This dissertation presents a novel multi-layer modeling framework based on Isogeometric Analysis, where each ply or lamina is represented by a Non-Uniform Rational B-Spline (NURBS) surface, and it is modeled as a Kirchhoff–Love thin shell. A residual stiffness approach is used to model intra-laminar damage in the framework of Continuum Damage Mechanics. A new zero-thickness cohesive interface formulation is introduced to model delamination as well as permitting laminate-level transverse shear compliance. The gradient-enhanced continuum damage model is then introduced to regularize material instabilities, which are typically associated with strain-softening damage models. This nonlocal regularization technique aims to re-establish mesh objectivity by limiting the dependence of damage predictions on the choice of discrete mesh. To account for the anisotropic damage modes of laminae, the proposed formulation smooths a tensor-valued strain field by solving an elliptic partial differential equation system on each lamina.

The proposed approach has significant accuracy and efficiency advantages over existing methods for modeling impact damage. These stem from the use of IGA-based Kirchhoff–Love shells to represent the individual plies of the composite laminate, while the compliant cohesive interfaces enable transverse shear deformation of the laminate. Kirchhoff–Love shells give a faithful representation of the ply deformation behavior, and, unlike solids or traditional shear-deformable shells, do not suffer from transverse-shear locking in the limit of vanishing thickness. This, in combination with higher-order accurate and smooth representation of the shell midsurface displacement field, allows to adopt relatively coarse in-plane discretizations without sacrificing solution accuracy. Furthermore, the thin-shell formulation employed does not use rotational degrees of freedom, which gives additional efficiency benefits relative to more standard shell formulations.

1 Introduction and Literature Review

This dissertation summarizes the research work focused on the development of novel analysis methodologies for progressive damage simulation of composite laminates. The literature review proposed in this introductory chapter defines the state-of-the-art of computational technologies for damage analysis of composites.

Different modeling approaches for intralaminar and interlaminar damage are discussed in Section 1.1. Applications of the multi-layer modeling technique for impact simulations are presented and in Section 1.2. Nonlocal regularization methodologies for strain–softening damage models are discussed in Section 1.3.

1.1 Modeling techniques for damage simulation of multi-layer composites

Rapid growth in the use of fiber-reinforced composite materials for high-performance and lightweight applications drives the demand for new computational technologies that are aimed at supporting the increasingly complex design process and testing of structures and structural components. For this purpose, the concept of Isogeometric Analysis (IGA) [58, 32] was recently introduced to ease the data flow between Computer-Aided Design (CAD) and computational analysis. Besides having a more direct link with CAD, the use of Non-Uniform Rational B-Splines (NURBS) [83], and their more advanced versions like T-Splines [12], as basis functions proved to be beneficial for the accuracy of numerical simulations due to the high-order continuity of the discretized fields, the variation diminishing property of NURBS, and a more accurate (and, in many cases, exact) representation of the analysis geometry. The inherent properties of higher-order accuracy and smoothness of spline functions, and the fact that splines were developed as a technology for representing surfaces, have led to rapid development of IGA for shell structures [68, 67, 16, 17, 69], including the introduction of a new thin-shell formulation based on the Kirchhoff–Love theory discretized using only displacement degrees of freedom [68]. This formulation, often combined with the bending-strip technique [67] to handle geometrically complex multi-patch structures, was successfully adopted in the framework of the Fluid–Structure Interaction (FSI) analysis [15] to efficiently simulate the dynamics of wind-turbine structures [70, 110], pulsatile ventricular assist devices [73], foil-based propulsion [109], hydraulic arresting gears [106], bioprosthetic heart valves [55], and parachutes [99]. In the present work, we extend the Kirchhoff–Love shell formulation to include, for an arbitrary number of plies, models that track damage initiation and progression at the individual ply level, and delamination at the ply interfaces.

The development of accurate and computationally efficient formulations capable of predicting the response of large-scale structures from the linear regime to the failure point, is a complex task. Indeed, the simulation of progressive damage propagation in fiber-reinforced polymer matrix composite laminates poses several challenges due to the stratified and non-homogeneous nature of the material. Major modeling challenges stem from the inherently complex mechanics of damage, which occurs at spatial scales that are often orders of magnitude smaller than the structural components analyzed. Damage in laminated composites is typically classified into two categories, namely, intralaminar and interlaminar damage. Intralaminar damage includes all the types of damage confined to the level of a single ply, such as fiber breaking, matrix cracking and fiber-matrix debonding. Interlaminar damage, conversely, occurs at the ply interfaces, and involves physical separation of the initially connected plies. For this reason, it is commonly referred to as delamination.

Various modeling approaches have been adopted for intralaminar and interlaminar damage. In recent years, the research has focused on the development of high-fidelity models capable of reproducing, at the meso-macro scale, the effects of the intralaminar damage. In this context, the introduction of the Continuum Damage Mechanics (CDM) [64, 27] gave rise to significant progress toward the unification of continuum mechanics and discrete representation of damage evolution, which is typically described in terms of discrete fracture mechanics. The purpose of the CDM is to simulate, at the continuum level, the equivalent effects of the various intralaminar damage modes. Several intralaminar damage models have been developed in the framework of the CDM. Ladeveze and Le Dantec [71] used the CDM to describe the effects of matrix cracking and matrix/fiber debonding at a macroscopic and continuum level. Matzenmiller et al. [75] proposed a progressive damage model for fiber-reinforced composites formulated in terms of the degradation of the original elastic properties. The model made use of the Hashin [46] failure criteria to determine the initiation of damage. Many studies were conducted in order to enhance this progressive damage model by introducing sophisticated failure criteria, in particular, for matrix-dominated damage modes. Puck and Schürmann [89] and Dàvila and Camanho [33] included the nonlinearity of the material and the effect of fiber kinking, while Pinho et al. [87] developed 3D criteria including nonlinear matrix shear behavior. The use of CDM was recently extended to IGA by Deng et al. [36], who proposed to use the residual-stiffness approach in order to predict failure loads of composite laminates, mainly under in-plane loading conditions.

While models based on the reduction of material stiffness are routinely adopted to account for the intralaminar damage in large-scale computations, modeling and simulation of the delamination process is a more delicate task, and represents an attractive research area. Solid-like shell elements, for example, were developed in the framework of the Extended Finite Element Method (XFEM) [91] and IGA [54] in order to simulate delamination by introducing kinematics discontinuities in the through-the-thickness direction. The Floating Node Method (FNM) was recently proposed by Carvalho et al. [26] in combination with the Virtual Crack Closure Technique (VCCT) in order to allow the actual splitting of elements in the FEM mesh. An alternative approach for the simulation of delamination involves the use of cohesive interfaces in combination with multi-layer modeling procedures [1, 2]. In this framework, the laminate is modeled at the level of each single ply, or a group of plies. For example, contiguous plies with the same fiber orientation are typically grouped into a single, thicker, ply for modeling purposes. Cohesive interfaces are introduced to connect the lamina and to enforce the appropriate traction-separation relationships between them. The definition of proper criteria for the degradation of the ply-interface stiffness allows for a continuous simulation of the delamination process, from damage initiation to complete separation. For this purpose, several cohesive laws have been proposed in recent years. The

Single-Mode Cohesive Model [8, 24], for example, considers the contribution of each opening mode as independent, and the delamination is complete only if the interface fails in all directions. Conversely, Mixed-Mode Cohesive Models [24, 103, 61] are formulated under the assumption that the delamination is triggered by the interaction of the openings in all directions. The deterioration of the interface is therefore described in terms of a single damage variable that grows under the combined action of normal and tangential opening modes.

While cohesive interfaces have been mostly applied in combination with solid elements, Dávila et. al [34] proposed a cohesive formulation for thick-shell elements. More recently, Nguyen et al. [79] presented a first example of the application of cohesive interfaces for thin shell elements in the framework of IGA. However, the purpose of the work in [79] was to present potential uses of IGA for applications involving cohesive-zone modeling rather than to propose, verify, and validate a cohesive-interface modeling framework, which we do here.

1.2 Isogeometric multi-layer modeling for progressive damage simulation

Fiber reinforced composite materials show great promise in applications requiring both high strength and low weight. However, the use of these materials in safety-critical applications is still limited, due to ongoing difficulties with prediction of damage. These difficulties stem from the complex, multi-modal failure mechanisms of fiber-reinforced composites [100]. Structures optimized for low weight frequently take the geometrical form of thin shells. Composite shells are often *laminates*, consisting of several layers of fiber-reinforced material, called *laminae*, or *plies*, bonded together. *Intra*laminar damage may occur within a given lamina, and *inter*laminar damage, or *delamination* may occur when bonds between laminae break down.

Because of the inherent heterogeneous nature of fiber-reinforced polymer composite materials and the complexity of their failure mechanisms, damage can occur at different length scales and often involves a simultaneous deterioration of the matrix material and separation of the layers that constitute the laminate, i.e., delamination. This damage mode, which often leads to a significant loss of strength of a structural component, may be difficult, if not impossible, to detect by visual inspection.

For these reasons, the response of composite laminates subjected to low velocity impact presents an important research direction. Experimental studies of Choi et al. [30] and a literature review from Richardson et al. [92] identified delamination as a critical factor, which, owing to local instabilities of the disconnected lamina, severely affects post-impact behavior of structures subjected to compressive loads. These authors also stressed the fact that failure modes in composite laminates are interrelated, and that the development of comprehensive modeling approaches that can simultaneously and accurately capture intralaminar failure and delamination is of primary importance.

Several models have been proposed, starting from the early 1990's, to predict damage growth in laminated composites subjected to low-velocity impact. Choi et al. [30, 29] developed finite element procedures to predict the extension of the delamination front based on the analysis of stresses in the plies. The references focused their attention on the interaction between matrix cracking and propagation of delamination. A prototype of a multi-layer modeling approach, where the plies are modeled as individual parts connected through discrete interfaces, was proposed in Allix et al. [1, 2] who developed a cohesive damage model in order to predict delamination under Mode I, Mode II, and mixed-mode openings. Several authors investigated the use of cohesive interfaces [77, 34] and cohesive elements [24, 111] to simulate the interaction between discrete plies in laminated structures, while Turon et al. [103, 104] developed a cohesive damage model in order to accurately predict delamination in composite laminates under multi-mode loading conditions. The use of discrete, connected interfaces, implemented either by means of surfaces or solid elements, allows for the development of multi-layer modeling techniques. As a result, a multi-layer representation combined with intralaminar damage modeling has become increasingly popular in recent years for progressive damage simulations of laminated composites.

A phenomenological Residual Stiffness Approach (RSA) [71, 75] is widely used as an intralaminar damage model. The RSA, which is developed in the framework of the Continuum Damage Mechanics (CDM), is based on a progressive reduction of the elastic properties of material as a function of the damage state, which is described in terms of the so-called damage variables that are evolved according to specific damage initiation and evolution criteria. Recent advances in the modeling of intralaminar damage include the introduction of the material nonlinearities [33] such as fiber kinking [87, 88] and nonlinear shear behavior [37]. Some authors [21, 101] also investigated the use of matrix plasticity to predict post-impact permanent indentation of the laminates. Several enhancements have been proposed in the past years for the intralaminar and interlaminar damage models. The proposed models make use of 3D solid linear [113, 37, 21, 101] and higher-order [43] Finite Elements (FE) for the discretization of the continuum. Faggiani et al. [41] proposed a mixed model where, in order to reduce the problem size, solid elements were used in the impact region while continuum shell elements were employed elsewhere. Davila et al. [34] developed a 2D cohesive interface for the Reissner–Mindlin shell elements and applied it to simulate delamination in aerospace structural components under quasi-static loading conditions.

Nevertheless, despite these enhancements, simulation of impact on laminated composite structures is dominated by 3D linear hexahedral elements. While the computational costs can be kept at a manageable level (i.e., $\mathcal{O}(10^5)$ elements) for coupon-scale simulations, 3D solid element technology becomes prohibitively expensive for larger-size structural components. This was one of the motivating factors for the development of a computational approach based on Isogeometric Analysis (IGA) [58, 32] in the framework of the multi-layer shell modeling presented in detail in Part I of this paper. Because the individual plies of a laminate are sufficiently thin to be reasonably described using the Kirchhoff–Love shell theory, we took the work of [68, 67] on rotation-free shells, and its extension to CDM in [36], as the starting point. The individual lamina, modeled as thin shells and discretized using spline-based IGA with only displacement degrees of freedom, were connected with cohesive interfaces resulting in an accurate and efficient methodology that is able to simultaneously model intralaminar damage and delamination. The use of IGA has an added benefit of a natural connection to Computer-Aided Design (CAD), allowing the use of CAD or other geometric modeling software to model structural components and directly analyze them using the same geometry representation, without the need to generate FE meshes [56]. We note that an alternative approach to delamination modeling using IGA may be found in the recently proposed continuum or solid-like shell formulations [52, 53].

1.3 Nonlocal regularization of strain–softening damage model for thin shells

We recently developed an approach for predicting damage in composite laminates that models laminae as a Kirchhoff–Love thin shells and interlaminar bonds as cohesive zones [14, 84]. Intralaminar damage in this framework evolved according to a continuum damage law accounting for various failure modes of fiber-reinforced composites. The cited references demonstrated the validity of this model by replicating several laboratory experiments.

Despite these promising initial results, it is not assured that the approach of [14, 84] will reliably work as-is for predicting damage in objects with general geometries and/or highly non-uniform or unstructured discretizations. The model of [14] relied on a local damage law, in which the strength of material at a point depends on the strain history at that point. This leads to the well-known strain-localization phenomenon, in which strains become concentrated, non-uniquely, in sets of measure zero. Finite element function spaces are unable to represent such deformations, and, as such, strains localize in mesh-dependent ways, and predictions may not converge under mesh refinement. This ill-posedness of local models is attributable to loss of ellipticity of the governing partial differential equation (PDE) system [80, 81]. The use of mesh-dependent computational models that do not correspond to well-posed mathematical models is at odds with the principles for verification and validation articulated by Babuška and Oden [7], in particular, their assertions that mathematical models should be well-posed, that exact solutions should be recoverable under refinement, and that "any validation process in which computational parameters, such as mesh size, are varied to bring experimental observations into closer agreement with numerical results are fundamentally flawed" [7, Footnote 4].

A way to improve the well-posedness of damage models is to introduce non-locality, so that the damage state at a material point depends on the strain history of not just that point, but neighboring points as well. A variety of non-local models have been proposed over the past several decades, including integral convolutions [86, 11], peridynamics [98], phase-field fracture models [3], and gradient-enhanced continuum damage [82]. In this work, we focus on the last of these, in which non-locality is introduced by solving an elliptic PDE. Gradient-enhanced damage (or, simply, "gradient damage") models may involve a PDE smoothing strains, damage indexes, or other quantities. Models smoothing a damage index are closely related to phase-field fracture models [35], and, in some publications, the terms "gradient-enhanced damage" and "phase-field fracture" are even used interchangeably. Phase-field fracture has recently attracted much attention, and a number of authors have proposed such damage-smoothing formulations for thin shell structures [78, 4, 66, 5]. However, in the present work, we focus on the strain-smoothing family of gradient-enhanced damage models. Our reasons for this are the following. We wish to adapt an existing, validated damage model that we studied in [14, 84]. When damage indices degrade material stiffness in the way stipulated by this model, damage smoothing may result in a phenomenon called stress locking, in which the model is unable to represent full material failure [62, 9]. [1]

A previous study adapted strain-smoothing gradient-enhanced damage modeling to continuum shell elements [51]. However, to our knowledge, very little (if any) prior work has applied this type of gradient damage modeling to thin shell structures. This is in part due to the fact that computational analysis of thin shell structures has only recently gained popularity, with the rise of *isogeometric analysis* (IGA). Isogeometric analysis is an emerging paradigm for computational mechanics, in which approximate solutions to PDEs are represented in the same function space as the geometry of their domains [58, 32]. Geometries of engineered objects are frequently designed by specifying surfaces using spaces of smooth spline functions such as NURBS [83], or T-splines [96]. This makes IGA appealing for analysis of thin shells for two reasons. First, the PDE domain for thin shell theory is itself a surface, and thus IGA may be applied directly to surface-based geometrical designs of shells. Second, the spline spaces used to design surfaces typically have C^1 or higher continuity, which, unlike traditional C^0 finite element function spaces, allows for standard Bubnov–Galerkin-type discretizations of fourth-order thin shell theories. IGA of thin shells began with the influential work of Kiendl and collaborators [68], on whose foundation the present study builds.

---

[1] Although the non-local model analyzed in [62] is not a gradient-enhanced model, our preliminary computations reported in A.5 indicate that some of the conclusions of [62] carry over.

1.4 Outline of the dissertation

The dissertation is organized as follow:

- *Chapter 2*: The concept of Isogeometric analysis is introduced and Non-Uniform Rational B-Spline surfaces are presented. The chapter focuses on a model reduction technique typically adopted to represent a solid structure in the three-dimensional space in terms of its reference midsurface. This technique is based on a kinematic assumption that relates the position of a material point of a continuum solid to its projection on the thin solid reference plane. Other relevant quantities for computational mechanics are derived starting from the kinematic description of the continuum.

- *Chapter 3*: This chapter introduces the basis of the multi-layer modeling approach developed for damage simulation of composite laminates. The Residual Stiffness Approach is introduced in the framework of Continuum Damage Mechanics for intralaminar damage modeling. A novel zero-thickness cohesive interface for thin-shell elements is presented for interlaminar damage modeling. Three numerical examples are presented: Two standard delamination benchmark test are simulated to validate the cohesive interface formulation; A ply-by-ply model of a thick laminate is simulated to verify that transverse-shear deformability is correctly reproduced by the proposed multi-layer modeling approach.

- *Chapter 4*: Several application of the multi-layer modeling approach for progressive damage simulations are presented in this chapter. Two low-velocity impact scenario on flat composite plates are simulated and results are compared with experimental results for validation purposes. An additional low-velocity impact scenario on a stiffened composite panel is presented. Finally, an hard-landing simulation of a Unmanned Aerial Vehicle is presented in order to illustrate an application of the design-to-analysis concept.

- *Chapter 5*: This chapter addresses the issue of strain-localization instability which typically affects strain-softening damage models. The gradient-enhanced formulation, a nonlocal regularization technique, is developed for Kirchhoff–Love shells. Several benchmark simulations are presented in order to verify the proposed gradient-enhanced formulation. Finally, low-velocity impact simulations are revisited in the framework of nonlocal damage modeling.

1.5 Acknowledgments

Chapter 1 is, in full, an edited reprint of the material as it appears in:

- *"A new multi-layer approach for progressive damage simulation in composite laminates based on isogeometric analysis and Kirchhoff–Love shells. Part I: basic theory and modeling of delamination and transverse shear"*, published on-line in *"Computational Mechanics"* on November 30th 2017 and co-authored by *Marco S. Pigazzini, Yuri Bazilevs, Andrew C. Ellison, and Hyonny Kim*. This article is currently in press. The author of this dissertation *(Marco S. Pigazzini)* is one of the primary investigators and author of this paper.
- *"A new multi-layer approach for progressive damage simulation in composite laminates based on isogeometric analysis and Kirchhoff–Love shells. Part II: impact modeling"*, published on-line in *"Computational Mechanics"* on November 24th 2017 and co-authored by *Marco S. Pigazzini, Yuri Bazilevs, Andrew C. Ellison, and Hyonny Kim*. This article is currently in press. The author of this dissertation *(Marco S. Pigazzini)* is the primary investigator and author of this paper.
- *Isogeometric analysis for simulation of progressive damage in composite laminates*, published on-line on April 22nd 2018 in *Journal of Composite Materials* and co-authored by *Marco S. Pigazzini, Yuri Bazilevs, Andrew C. Ellison, and Hyonny Kim*. This article is currently in press. The author of this dissertation *(Marco S. Pigazzini)* is the primary investigator and author of this paper.
- *"Gradient-enhanced damage modeling in Kirchhoff–Love shells: Application to isogeometric analysis of composite laminates"*. This manuscript in preparation is co-authored by *Marco S. Pigazzini, David Kamensky, Dennis A. P. van Iersel, Joris J.C. Remmers, and Yuri Bazilevs*. The author of this dissertation *(Marco S. Pigazzini)* is the primary investigator and author of this paper.

2 Foundation of Isogeometric Analysis for the structural analysis of thin shells

The Isogeometric concept for structural analysis applications is presented in this chapter. Non-Uniform Rational B-Spline surfaces are presented in Section 2.1, while Section 2.2 focuses on a model reduction technique, which is typically adopted to represent thin solid structures in the three-dimensional space a function of their reference midsurface planes. This technique is based on a kinematic assumption that relates the position of a material point of a continuum solid to its projection on the thin solid reference plane. In Section 2.3, other relevant quantities for computational mechanics are derived starting from the kinematic description of the continuum.

Remark The convention used in this chapter is that lower-case indices correspond to covariant components of tensor-valued variables, while upper-case indices correspond to contravariant components of tensor-valued variables.

2.1 B-Spline and NURBS surfaces

The concept of Isogeometric Analysis for computational mechanics stems from the use of smooth Non Uniform Rational B-Spline (NURBS) for geometry representation and discretization of unknowns. NURBS curves are derived from Basis Spline (B-Spline) curves, which posses superior approximation properties compared to traditional Lagrange polynomials typically adopted for Finite Elements analysis. See for example the extensive description reported in Piegl and Tiller [83]. Starting from the definition of B-Spline basis functions, this section summarizes the derivation of NURBS surfaces in terms of their parametric coordinates.

2.1.1 B-Spline basis functions

B-Spline basis function are defined in the parametric domain, which is defined by the knot vector $\boldsymbol{\xi} = \left[\xi_1, ..., \xi_{n+p+1}\right]$. B-Spline basis functions are C^{∞} on a knot span sub-domain $\xi \in [\xi_i, \xi_{i+1}]$ (i.e., between two distinct knots). Continuity of B-Spline basis functions at knots is a function of the knot multiplicity: a B-Spline basis functions of degree p is C^{p-k} continuous at a knot with multiplicity k.

B-Spline curves are constructed in the parametric domain though the Cox–De Boor recursive algorithm [83]. Starting from the analytical expression of the *0-th* degree $\mathrm{N}_{i,0}$ B-Spline basis function (order = p+1=1) in the domain $\xi \in [\xi_i, \xi_{i+1}]$:

$$\mathrm{N}_{i,0}\left(\xi\right) = \begin{cases} 1 & \text{if} \quad \xi_i \geq \xi \geq \xi_{i+1} \quad , \\ 0 & \text{otherwise} \quad . \end{cases} \tag{2.1}$$

Higher degree B-Spline basis functions in the domain $\xi \in [\xi_i, \xi_{i+1}]$ are computed straightforwardly as:

$$\mathrm{N}_{i,p}\left(\xi\right) = \frac{\xi - \xi_i}{\xi_{i+p} - \xi_i} \mathrm{N}_{i,p-1}\left(\xi\right) + \frac{\xi_{i+p+1} - \xi}{\xi_{i+p+1} - \xi_{i+1}} \mathrm{N}_{i+1,p-1}\left(\xi\right) \ . \tag{2.2}$$

B-Spline of degree p is non-null over *p+1* knot spans of the parametric domain. Parametric derivatives of B-Spline basis functions can also be computed analogously using a recursive expression [83]:

$$\mathrm{N}'_{i,p}\left(\xi\right) = \frac{\xi - \xi_i}{\xi_{i+p} - \xi_i} \mathrm{N}_{i,p-1}\left(\xi\right) + \frac{\xi_{i+p+1} - \xi}{\xi_{i+p+1} - \xi_{i+1}} \mathrm{N}_{i+1,p-1}\left(\xi\right) \ . \tag{2.3}$$

2.1.2 B-Spline curves and surfaces

B-Spline curves are defined as a linear combination of B-Spline basis functions:

$$\mathbf{C}\left(\xi\right) = \sum_{i=1}^{n} \mathrm{N}_{i,p}\left(\xi\right) \mathbf{B}_i \ , \tag{2.4}$$

where the coefficients of the linear combination $\mathbf{B}_i$ are the called “control points”. A B-Spline curve in the $\mathbb{R}^{\mathrm{NSD}}$ space, can be expressed in terms of components ad:

$$\mathrm{C}_k\left(\xi\right) = \sum_{i=1}^{n} N_{i,p}\left(\xi\right) \mathrm{B}_{i_k} \ , \tag{2.5}$$

where $k = 1, ..., \mathrm{NSD}$. It is worth noting that B-Spline curves do not interpolate, in general, control points at their location. A B-Spline curve interpolates a control point only if the multiplicity of the knot is $k = p$, in which case the B-Spline curve is only C^0 continuous at that knot.

B-Spline surfaces are constructed from the tensor product of B-Spline basis functions of degree p and q, which are constructed on their respective parametric domain $\boldsymbol{\xi}_1 = \left[\xi_{1_1}, ..., \xi_{1_{n+p+1}}\right]$ and $\boldsymbol{\xi}_2 = \left[\xi_{2_1}, ..., \xi_{2_{m+q+1}}\right]$:

$$\mathbf{C}\left(\xi_1, \xi_2\right) = \sum_{i=1}^{n} \sum_{j=1}^{m} \mathrm{N}_{i,p}\left(\xi_1\right) \mathrm{N}_{j,q}\left(\xi_2\right) \mathbf{B}_{i,j} \, . \tag{2.6}$$

2.1.3 NURBS basis functions, curves and surfaces

The construction of Non Uniform Rational B-Spline basis functions requires the additional definition of "weight", which stems from the concept of projection of the control points from a higher-dimensional space. Consider, for example, the control point $\mathbf{B}_i^{\mathrm{w}}$ for the *i-th* B-Spline curve in $\mathbb{R}^{\mathrm{NSD}+1}$. Then, the *k-th* component of the control point in $\mathbb{R}^{\mathrm{NSD}}$ is defined by projecting :

$$\mathrm{B}_{i_k} = \frac{\mathrm{B}_{i_k}^{\mathrm{w}}}{\mathrm{B}_{i_{\mathrm{NSD+1}}}^{\mathrm{w}}} = \frac{\mathrm{B}_{i_k}^{\mathrm{w}}}{w_i} \; ; \; k = 1, ..., \mathrm{NSD} \, , \tag{2.7}$$

where x_i is the weight of the *i-th* B-Spline in $\mathbb{R}^{\mathrm{NSD}+1}$. NURBS basis functions of degree p are defined as:

$$\mathrm{R}_{i,p}\left(\xi\right) = \frac{\mathrm{N}_{i,p}\left(\xi\right) w_i}{\sum_{t=1}^{n} \mathrm{N}_{t,p}\left(\xi\right) w_t} \, , \tag{2.8}$$

while NURBS curves are computed from the linear combination of NURBS basis functions:

$$\mathbf{C}\left(\xi\right) = \sum_{i=1}^{n} \mathrm{R}_{i,p}\left(\xi\right) \mathbf{B}_i \, , \tag{2.9}$$

Similarly to B-Spline, basis function of NURBS surfaces are constructed from the tensor product of NURBS basis functions of degree p and q, which are constructed on their respective parametric domain $\boldsymbol{\xi}_1 = \left[\xi_{1_1}, ..., \xi_{1_{n+p+1}}\right]$ and $\boldsymbol{\xi}_2 = \left[\xi_{2_1}, ..., \xi_{2_{m+q+1}}\right]$:

$$\mathrm{R}_{(i,j),(p,q)}\left(\xi_1, \xi_2\right) = \frac{N_{i,p}\left(\xi_1\right) M_{j,q}\left(\xi_2\right) w_{i,j}}{\sum_{t=1}^{n} \sum_{s=1}^{m} N_{t,p}\left(\xi_1\right) M_{s,q}\left(\xi_2\right) w_{t,s}} \, , \tag{2.10}$$

where $N_{i,p}$ and $M_{j,q}$ are basis functions of B-spline curves. Finally, NURBS surfaces are computed from a linear combination of NURBS surface basis functions:

$$\mathbf{S}\left(\xi_1, \xi_2\right) = \sum_{i=1}^{n} \sum_{j=1}^{m} \mathrm{R}_{(i,j),(p,q)}\left(\xi_1, \xi_2\right) \mathbf{B}_{i,j} \, . \tag{2.11}$$

For purposes of numerical analysis, "finite elements" are taken to be knot spans, namely,

$[\xi_i, \xi_{i+1}] \times [\eta_j, \eta_{j+1}]$. A comprehensive analysis of approximation properties of NURBS as shape functions is reported in [58], where refinement techniques are also discussed.

2.2 Shell modeling: differential geometry of manifolds

The point of departure of this work is the derivation of the kinematic equations of a continuum thin solid in the three-dimensional space as a function of NURBS in-plane parametric coordinates ξ_1 and ξ_2. Following a commonly adopted approach, see i.e. Bischoff et al. [19], the kinematics of a thin continuum solid is described in terms of its midsurface displacement and shell director. This model is based on the Kirchhoff assumption, which posits that a shell director remains normal to the shell midsurface during the deformation. It follows that the position vectors of a material point in the reference and current configuration, denoted respectively by $\mathbf{X}$ and $\mathbf{x}$, are expressed as:

$$\begin{aligned} \mathbf{X}(\xi_1,\xi_2,\xi_3) &= \mathrm{X}_0^{\zeta}(\xi_1,\xi_2)\,\mathbf{j}_{\zeta} + \xi^3 \mathrm{G}_3^{\zeta}(\xi_1,\xi_2)\,\mathbf{j}_{\zeta}\,, \\ \mathbf{x}(\xi_1,\xi_2,\xi_3) &= \mathrm{x}_0^{\zeta}(\xi_1,\xi_2,)\,\mathbf{j}_{\zeta} + \xi^3 \mathrm{g}_3^{\zeta}(\xi_1,\xi_2)\,\mathbf{j}_{\zeta}\,, \end{aligned} \tag{2.12}$$

where $\mathbf{X}_0$ and $\mathbf{x}_0$ are the position vectors of a material point on the shell midsurface in the reference and current configuration, $\xi^3 \in \left[-\frac{h_{th}}{2}, \frac{h_{th}}{2}\right]$ and h_{th} denotes the shell thickness. The vector $\mathbf{j}_{\zeta}$ is a basis of the global Cartesian coordinate system and ζ = 1, 3 in the three dimensional space. The covariant in-plane basis vectors $\mathbf{G}_{\alpha}$ and $\mathbf{g}_{\alpha}$ are obtained by taking a partial derivative of the midsurface position vectors with respect to the NURBS parametric coordinates ξ_1 and ξ_2 as:

$$\begin{aligned} \mathbf{G}_{\alpha} &= \mathrm{X}^{\zeta}_{0,\xi^{\alpha}}\mathbf{j}_{\zeta} = \frac{\partial \mathrm{X}_0^{\zeta}}{\partial \xi_{\alpha}}\mathbf{j}_{\zeta}\,, \\ \mathbf{g}_{\alpha} &= \mathrm{x}^{\zeta}_{0,\xi^{\alpha}}\mathbf{j}_{\zeta} = \frac{\partial \mathrm{x}_0^{\zeta}}{\partial \xi_{\alpha}}\mathbf{j}_{\zeta}\,, \end{aligned} \tag{2.13}$$

where index $\alpha = 1,2$. Since a NURBS surface is defined as function of two in-plane curvilinear parameters, the third basis vector orthogonal to the midsurface, namely $\mathbf{G}_3$ and $\mathbf{g}_3$ in Equation (2.12), is obtained from the cross-products of the in-plane basis vectors as:

$$\mathbf{G}_3 = \frac{\mathbf{G}_1 \times \mathbf{G}_2}{\|\mathbf{G}_1 \times \mathbf{G}_2\|}, \quad \mathbf{g}_3 = \frac{\mathbf{g}_1 \times \mathbf{g}_2}{\|\mathbf{g}_1 \times \mathbf{g}_2\|}\,. \tag{2.14}$$

It is also worth noting that, since the components of basis vectors are expressed with respect to the global Cartesian basis, the global Cartesian basis $\mathbf{j}$ is omitted in order to simplify the notation.

As illustrated in Figure 2.1, a local Cartesian coordinate system is also defined such that $\bar{\mathbf{e}}_1$

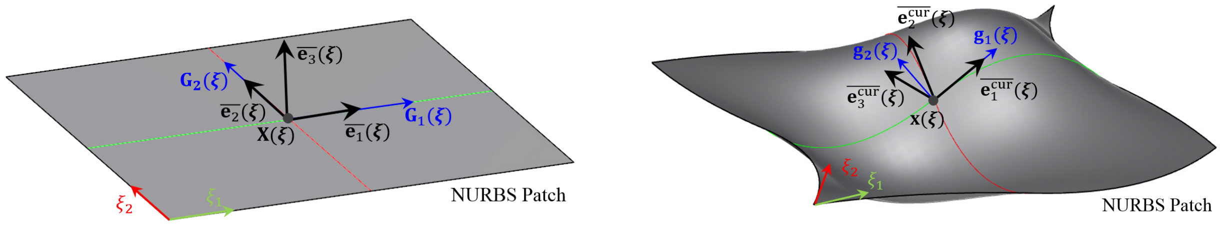

(a) (b)

Figure 2.1: Representation of curvilinear and Cartesian basis vectors on a NURBS patch in the (a) Reference and (b) Deformed configuration.

is parallel to the vector $\mathbf{G}_1$, namely:

$$\bar{\mathbf{e}}_1 = \frac{\mathbf{G}_1}{\|\mathbf{G}_1\|} , \tag{2.15}$$

while the second basis vector $\bar{\mathbf{e}}_2$ lies in the plane spanned by $\mathbf{G}_1$ and $\mathbf{G}_2$ and it is orthogonal to $\bar{\mathbf{e}}_1$ by construction:

$$\bar{\mathbf{e}}_2 = \frac{\mathbf{G}_2 - (\mathbf{G}_2 \cdot \bar{\mathbf{e}}_1)\,\bar{\mathbf{e}}_1}{\|\mathbf{G}_2 - (\mathbf{G}_2 \cdot \bar{\mathbf{e}}_1)\,\bar{\mathbf{e}}_1\|} . \tag{2.16}$$

The corresponding in-plane Cartesian basis vectors in the current configuration are denoted by $\bar{\mathbf{e}}_1^{\text{cur}}$ and $\bar{\mathbf{e}}_2^{\text{cur}}$ and are defined analogously. The out-of-plane vectors of the Cartesian basis coincides with the normal vectors defined in Equation (2.14), that is, $\bar{\mathbf{e}}_3 \equiv \mathbf{G}_3$ and $\bar{\mathbf{e}}_3^{\text{cur}} \equiv \mathbf{g}_3$.

Following the definition of the in-plane basis, it is convenient to introduce the metric tensor $\mathbf{M}$ of the reference midsurface:

$$\mathbf{M} = \left[G_{\alpha\beta}\right] \; ; \; G_{\alpha\beta} = \mathbf{G}_\alpha \cdot \mathbf{G}_\beta , \tag{2.17}$$

The contravariant in-plane basis vector $\mathbf{G}^\alpha$ is computed straightforwardly from the covariant basis vectors $\mathbf{G}_\beta$ and the components of the inverse midsurface metric:

$$\mathbf{G}^\alpha = \left[G^{\alpha\beta}\right] \mathbf{G}_\beta , \tag{2.18}$$

where $\left[G^{\alpha\beta}\right] = \left[G_{\alpha\beta}\right]^{-1}$.

2.3 Kinematic of the Kirchhoff–Love shell

The kinematic model underlying the thin-shell formulation is based on the Kirchhoff assumption. This hypothesis implies that, at the level of individual plies, transverse shear is neglected in the model. Furthermore, the kinematics of the shell can be described purely as a function of its midsurface displacements without introducing rotational Degrees of Freedom (DOF), and thus reducing the number of DOFs up to 50% compared to the more standard Reissner–Mindlin-type thick-shell formulation. In addition, because transverse shear is not present in the theory, the Kirchhoff–Love shell does not experience any shear locking in the limit of vanishing thickness. These factors greatly improve the computational efficiency of Kirchhoff–Love-shell-based formulation for laminated composite structures, especially in the context of layer-by-layer modeling using multiple shells to represent individual plies or ply groups.

In order formulate a structural model based on the thin shell theory, we introduce the Green–Lagrange strain measure, which is finite-strain and objective strain tensor, not affected by rigid body translations:

$$\mathbf{E} = \frac{1}{2}\left(\mathbf{F}^{\mathrm{T}}\mathbf{F} - \mathbf{I}\right) = \mathrm{E}_{\alpha\beta}\, \widetilde{\mathbf{G}}^{\alpha} \otimes \widetilde{\mathbf{G}}^{\beta} \,, \tag{2.19}$$

where $\mathbf{F}$ is the deformation gradient tensor and $\mathbf{I}$ is the second-order identity tensor. In Equation (2.19), $\widetilde{\mathbf{G}}^{\alpha}$ represent a contravariant basis vector at a material point $\mathbf{X}$.

Remark It is worth noting that a basis vector $\widetilde{\mathbf{G}}_{\alpha}$ coincide with an in-plane basis vector $\mathbf{G}^{\alpha}$, as defined in Equation (2.13), if the material point $\mathbf{X}$ lies on the shell midsurface (i.e., if $\mathbf{X} \equiv \mathbf{X}_0$).

In the framework of the Kirchhoff–Love shell kinematics assumptions, the Green–Lagrange strain tensor can be expressed by separating the membrane and bending contributions. The separation of the strain tensor into in-plane and curvature components can be justified based on the kinematic assumption of the thin shell model, as expressed by Equation (2.12). Consider, for instance, deformation gradient tensor:

$$\mathbf{F} = \widetilde{\mathbf{g}}_{\alpha} \otimes \widetilde{\mathbf{G}}^{\beta} \;;\; \mathbf{F}^{T} = \widetilde{\mathbf{G}}^{\alpha} \otimes \widetilde{\mathbf{g}}_{\beta} \,, \tag{2.20}$$

where $\widetilde{\mathbf{G}}_{\alpha}$ and $\widetilde{\mathbf{g}}_{\alpha}$ are the covariant basis vectors, obtained by differentiating the position vectors $\mathbf{x}$ and $\mathbf{X}$, as expressed in Equation (2.12), with respect to the NURBS in-plane parametric coordinate ξ_{α}:

$$\begin{aligned} \widetilde{\mathbf{G}}^{\alpha} &= \frac{\partial \mathrm{X}}{\partial \xi_{\alpha}} = \frac{\partial \mathbf{X}_0}{\partial \xi_{\alpha}} + \xi^{3}\frac{\partial \mathbf{G}_3}{\partial \xi_{\alpha}} \\ \widetilde{\mathbf{g}}^{\alpha} &= \frac{\partial \mathrm{x}}{\partial \xi_{\alpha}} = \frac{\partial \mathbf{x}_0}{\partial \xi_{\alpha}} + \xi^{3}\frac{\partial \mathbf{g}_3}{\partial \xi_{\alpha}} \,. \end{aligned} \tag{2.21}$$

It follows that the covariant components of strain tensor $\mathrm{E}_{\alpha\beta}$ can be expressed in terms of the metric coefficients as:

$$\mathrm{E}_{\alpha\beta} = \frac{1}{2}\left(\widetilde{\mathrm{g}}_{\alpha\beta} - \widetilde{\mathrm{G}}\alpha\beta\right) \,. \tag{2.22}$$

where the metric coefficients $\mathrm{g}_{\alpha\beta}$ and $\mathrm{G}_{\alpha\beta}$, are computed straightforwardly by taking the inner product of the basis vectors:

$$
\begin{aligned}
\widetilde{\mathrm{G}}_{\alpha\beta} &= \left(\frac{\partial \mathbf{X}_0}{\partial \xi_\alpha} + \zeta^3 \frac{\partial \mathbf{G}_3}{\partial \xi_\alpha}\right) \cdot \left(\frac{\partial \mathbf{X}_0}{\partial \xi_\beta} + \zeta^3 \frac{\partial \mathbf{G}_3}{\partial \xi_\beta}\right) \\
&= \left(\mathbf{G}_\alpha + \zeta^3 \frac{\partial \mathbf{G}_3}{\partial \xi_\alpha}\right) \cdot \left(\mathbf{G}_\beta + \zeta^3 \frac{\partial \mathbf{G}_3}{\partial \xi_\beta}\right) \\
\widetilde{\mathrm{g}}_{\alpha\beta} &= \left(\frac{\partial \mathbf{x}_0}{\partial \xi_\alpha} + \zeta^3 \frac{\partial \mathbf{g}_3}{\partial \xi_\alpha}\right) \cdot \left(\frac{\partial \mathbf{x}_0}{\partial \xi_\beta} + \zeta^3 \frac{\partial \mathbf{g}_3}{\partial \xi_\beta}\right) \\
&= \left(\mathbf{g}_\alpha + \zeta^3 \frac{\partial \mathbf{g}_3}{\partial \xi_\alpha}\right) \cdot \left(\mathbf{g}_\beta + \zeta^3 \frac{\partial \mathbf{g}_3}{\partial \xi_\beta}\right) \,.
\end{aligned}
\tag{2.23}
$$

By introducing Equation (2.23) into Equation (2.22) and by neglecting the terms multiplied by $\left(\zeta^3\right)^2$, which is a reasonable assumption for thin shells since they are proportional to h_{th}^2, the curvilinear components of the Green-Lagrange strain tensor can be expressed as:

$$
\begin{aligned}
\mathrm{E}_{\alpha\beta} = \frac{1}{2} &\left(\mathbf{g}_\alpha \cdot \mathbf{g}_\beta - \mathbf{G}_\alpha \cdot \mathbf{G}_\beta\right) \\
&+ \zeta^3 \left[\left(\mathbf{g}_\alpha \cdot \frac{\partial \mathbf{g}_3}{\partial \xi_\beta} + \mathbf{g}_\beta \cdot \frac{\partial \mathbf{g}_3}{\partial \xi_\alpha}\right) - \left(\mathbf{G}_\alpha \cdot \frac{\partial \mathbf{G}_3}{\partial \xi_\beta} + \mathbf{G}_\beta \cdot \frac{\partial \mathbf{G}_3}{\partial \xi_\alpha}\right)\right].
\end{aligned}
\tag{2.24}
$$

Because of the orthogonality of in-plane basis $\mathbf{g}_\alpha$ and the shell normal vector $\mathbf{g}_3$, Equation (2.24) can be further simplified. Consider the following equivalent form that express the curvature of the manifold in the current configuration:

$$
\mathbf{g}_\alpha \cdot \frac{\partial \mathbf{g}_3}{\partial \xi_\beta} = \mathbf{g}_\beta \cdot \frac{\partial \mathbf{g}_3}{\partial \xi_\alpha} = -\frac{\partial \mathbf{g}_\alpha}{\partial \xi_\beta} \cdot \mathbf{g}_3. \tag{2.25}
$$

Introducing Equation (2.25) in Equation (2.24) leads to the canonical expression of the Green–Lagrange strain components for this shells:

$$
\mathrm{E}_{\alpha\beta} = \frac{1}{2}\left(\mathbf{g}_\alpha \cdot \mathbf{g}_\beta - \mathbf{G}_\alpha \cdot \mathbf{G}_\beta\right) + \zeta^3 \left(\frac{\partial \mathbf{G}_\alpha}{\partial \xi_\beta} \cdot \mathbf{G}_3 - \frac{\partial \mathbf{g}_\alpha}{\partial \xi_\beta} \cdot \mathbf{g}_3\right) = \varepsilon_{\alpha\beta} + \xi_3 \kappa_{\alpha\beta}\,, \tag{2.26}
$$

where the covariant components $\varepsilon_{\alpha\beta}$ of the *membrane strain* tensor $\boldsymbol{\varepsilon}$ are defined as:

$$
\varepsilon_{\alpha\beta} = \frac{1}{2}\left(\mathbf{g}_\alpha \cdot \mathbf{g}_\beta - \mathbf{G}_\alpha \cdot \mathbf{G}_\beta\right)\,, \tag{2.27}
$$

and the covariant components $\kappa_{\alpha\beta}$ of the *curvature-change* strain tensor $\boldsymbol{\kappa}$ are defined as:

$$
\kappa_{\alpha\beta} = \left(\mathbf{G}_{\alpha,\xi_\beta} \cdot \mathbf{G}_3\right) - \left(\mathbf{g}_{\alpha,\xi_\beta} \cdot \mathbf{g}_3\right)\,. \tag{2.28}
$$

Finally, in order to use an orthotropic contitutive law, it is required to compute the components of the strain tensor associated with an orthogonal basis. This is involves the change of basis from curvilinear (2.13) to local Cartesian (2.15) and (2.16) basis. The Cartesian components of the membrane strain and curvature tensor are computed from their covariant counterparts as:

$$\bar{\varepsilon}_{\alpha\beta} = \varepsilon_{\gamma\delta} \left(\widetilde{\mathbf{G}}^{\gamma} \cdot \bar{\mathbf{e}}_{\alpha} \right) \left(\widetilde{\mathbf{G}}^{\delta} \cdot \bar{\mathbf{e}}_{\beta} \right), \tag{2.29}$$

$$\bar{\kappa}_{\alpha\beta} = \kappa_{\gamma\delta} \left(\widetilde{\mathbf{G}}^{\gamma} \cdot \bar{\mathbf{e}}_{\alpha} \right) \left(\widetilde{\mathbf{G}}^{\delta} \cdot \bar{\mathbf{e}}_{\beta} \right) . \tag{2.30}$$

Details of the transformation from curvilinear to Cartesian components of a second order tensor are reported in Appendix A.1. Following the change of basis, the Cartesian components of the Green–Lagrange strain tensor for the Kirchhoff–Love shell formulation are expressed as:

$$\overline{\mathrm{E}}_{\alpha\beta} = \bar{\varepsilon}_{\alpha\beta} + \xi_3 \bar{\kappa}_{\alpha\beta} . \tag{2.31}$$

2.4 Acknowledgments

Chapter 2 is, in part, an edited reprint of the material as it appears in:

- *"A new multi-layer approach for progressive damage simulation in composite laminates based on isogeometric analysis and Kirchhoff–Love shells. Part I: basic theory and modeling of delamination and transverse shear"*, published on-line in *"Computational Mechanics"* on November 30th, 2017 and co-authored by *Marco S. Pigazzini, Yuri Bazilevs, Andrew C. Ellison, and Hyonny Kim*. This article is currently in press. The author of this dissertation *(Marco S. Pigazzini)* is one of the primary investigators and authors of this paper.
- *"A new multi-layer approach for progressive damage simulation in composite laminates based on isogeometric analysis and Kirchhoff–Love shells. Part II: impact modeling"*, published on-line in *"Computational Mechanics"* on November 24th, 2017 and co-authored by *Marco S. Pigazzini, Yuri Bazilevs, Andrew C. Ellison, and Hyonny Kim*. This article is currently in press. The author of this dissertation *(Marco S. Pigazzini)* is the primary investigator and author of this paper.

This work was supported by NASA Advanced Composites Project No. 15-ACP1-0021. The co-authors of the articles [14, 84] and I thank F. Leone, C, Rose, and C. Davila from NASA Langley Research Center for their valuable comments and suggestions.

3 Isogeometric multi-layer modeling approach for composite laminates

This chapter outlines the key aspects of the IGA-based multi-layer analysis framework that were developed for progressive damage analysis of composite laminates. The multi-layer model developed by the authors is based on the hypothesis that each ply can be represented, individually, by an independent NURBS (or other spline-based) surface. This allows the modeling of interlaminar damage and explicit ply separation (i.e., delamination). In addition, intralaminar damage, which includes fiber breaking, kinking, matrix cracking and fiber debonding, is modeled at the individual lamina level.

One of the key modeling assumptions is that individual plies of a composite laminate are represented by the Kirchhoff–Love shell model, which was developed in order to model thin shells. As discussed in Chapter 2, the kinematics of the Kirchhoff–Love shell element is described purely as function of the midsfurface displacements. The kinematic model underlying the thin-shell formulation is based on the Kirchhoff assumption, which posits that the shell director remains normal to the shell midsurface during the deformation. This hypothesis implies that, at the level of each individual ply, transverse shear is neglected. However, the shear deformability of the whole laminate is recovered due to the presence of compliant cohesive interfaces, which allow for relative in-plane displacement between the connected plies. In particular, we showed [14] that it is possible to compute a specific value of cohesive stiffness, which depends on the material shear modulus and ply thickness, such that the multi-layer model mimics correctly the transverse shear behavior predicted by the First-order Shear Deformable Theory (FSDT).

In the proposed multi-layer model, the plies are connected through zero-thickness cohesive interface whose stiffness is progressively reduced to account for the evolution of interlaminar damage, commonly referred as delamination, which involves local separation of individual plies, or groups of plies, from the original laminate. In the framework of the multi-layer modeling approach we represent the laminate ply-by-ply and we use zero-thickness cohesive interfaces to connect adjacent plies. A cohesive interface is defined between distinct NURBS surfaces, thereby introducing a surface traction term proportional to the relative displacement. A cohesive damage law enables the detection of the onset of permanent interlaminar damage and progression of the delamination front.

The equivalent effects of intralaminar damage are modeled at the lamina level. Intralaminar damage include failures of the matrix phase, such as matrix cracking, of the reinforcement phase, such as fiber breaking and fiber kinking, and of the fiber-matrix interface, such as fiber debonding. While these failures occur at the microscale level, their effects at the meso- and macro-scale levels are often described using a residual stiffness approach in the framework of Continuum Damage Mechanics (CDM) [75]. While the theoretical assumptions lead to a simplified representation of the actual damage state of the material, this model is often preferred for meso- and macro-scale simulations because, while being relatively simple from computational standpoint, it is still able to accurately predict damage growth in composite laminates (see, e.g., results for impact damage on composite laminates [101, 41]).

The modeling framework presented in this dissertation uses a phenomenological Residual Stiffness Approach (RSA) [75] in order to model the intralaminar damage at the level of each individual ply. The RSA implementation is developed in the framework of the CDM and it is based on progressive degradation of the pristine-material elastic properties as a function of local damage variables. For this purpose, a strain-softening damage model [36] is used to degrade material stiffness tensor as a function of local damage variables. The use of local damage theories in combination with strain-softening degradation models may lead to strain localization resulting in high mesh sensitivity of the solution (see, e.g., the work of Lapczyk and Hurtado [72]). However, the introduction of a length scale in the damage model, as proposed by Bažant and Oh [10], allows one to alleviate the global effects of damage localization.

3.1 Equations of structural dynamics

The equations of dynamic equilibrium for structural dynamics are obtained from the principle of virtual work. This leads to the variational form of the linear momentum equation, which is stated as follow: Given the trial-function set S_{x} and the test-function set S_{w}, find the configuration $\mathbf{x} \in S_{\mathrm{x}}$ such that $\forall\ \mathbf{w} \in S_{\mathrm{w}}$,

$$\int_{\Omega_0} \mathbf{w} \cdot \tilde{\rho}_0 \left(\frac{d^2\mathbf{x}}{dt^2} - \mathbf{f} \right) \mathrm{d}\Omega + \int_{\Omega_0} \delta\overline{\mathbf{E}} : \overline{\mathbf{S}}\, \mathrm{d}\Omega - \int_{(\Gamma_t)_h} \mathbf{w} \cdot \mathbf{h}\, \mathrm{d}\Gamma = 0\,, \tag{3.1}$$

where $\tilde{\rho}_0$ is the density per unit volume in the reference configuration, $\mathbf{f}$ are the body forces acting on the domain Ω_0 and $\mathbf{h}$ are the surface traction acting on sub–region of the boundary $(\Gamma_t)_h$.

Following the discussion presented in Chapter 2, the linear momentum equation can be simplified for thin continuum solids modeled as shells and represented by their reference midsurface. By introducing the kinematic Equation 2.12 in the variational form (3.1), it is possible to separate the volume integrals in Equation (3.1) into in-plane and through-the-thickness integrals. Furthermore, for thin structures plan stress state is typically assumed and the Green–Lagrange strain tensor in Equation (3.1) may be conveniently expressed in Voigt notation as:

$$\overline{\mathbf{E}} = \begin{bmatrix} \overline{\mathrm{E}}_{11} \\ \overline{\mathrm{E}}_{22} \\ \overline{\mathrm{E}}_{12} \end{bmatrix} = \begin{bmatrix} \overline{\varepsilon}_{11} \\ \overline{\varepsilon}_{22} \\ \overline{\varepsilon}_{12} \end{bmatrix} + \xi_3 \begin{bmatrix} \overline{\kappa}_{11} \\ \overline{\kappa}_{22} \\ \overline{\kappa}_{12} \end{bmatrix} . \tag{3.2}$$

The St. Venant–Kirchhoff material law is then introduced to relate the second Piola–Kirchhoff stresses to the Green–Lagrange strain as:

$$\begin{bmatrix} \overline{\mathrm{S}}_{11} \\ \overline{\mathrm{S}}_{22} \\ \overline{\mathrm{S}}_{12} \end{bmatrix} = \overline{\mathbf{C}} \begin{bmatrix} \overline{\mathrm{E}}_{11} \\ \overline{\mathrm{E}}_{22} \\ \overline{\mathrm{E}}_{12} \end{bmatrix} , \tag{3.3}$$

where $\overline{\mathbf{C}}$ is the plane stress constitutive material stiffness matrix expressed in the local coordinate system. It follows that the internal work of Equation (3.1) can be conveniently expressed as:

$$\begin{aligned} &\int_{\Omega_0} \delta\overline{\mathbf{E}} : \overline{\mathbf{S}} \, \mathrm{d}\Omega = \\ &\int_{\Gamma_0^s} \delta\overline{\boldsymbol{\varepsilon}} \cdot \left[\left(\int_{h_{th}} \overline{\mathbf{C}} \, \mathrm{d}\xi_3 \right) \overline{\boldsymbol{\varepsilon}} + \left(\int_{h_{th}} \xi_3 \overline{\mathbf{C}} \, \mathrm{d}\xi_3 \right) \overline{\boldsymbol{\kappa}} \right] \mathrm{d}\Gamma \\ + &\int_{\Gamma_0^s} \delta\overline{\boldsymbol{\kappa}} \cdot \left[\left(\int_{h_{th}} \xi_3 \overline{\mathbf{C}} \, \mathrm{d}\xi_3 \right) \overline{\boldsymbol{\varepsilon}} + \left(\int_{h_{th}} \xi_3^2 \overline{\mathbf{C}} \, \mathrm{d}\xi_3 \right) \overline{\boldsymbol{\kappa}} \right] \mathrm{d}\Gamma . \end{aligned} \tag{3.4}$$

3.1.1 Basic semi-discrete variational formulation of the Kirchhoff–Love shell

The Isogeometric discretization then is introduced in the variational Equation (3.1), in which the position vector of a material point on the shell midsurface is approximated using a set of NURBS shape functions as:

$$\mathbf{x}_0^h(\xi_1, \xi_2) = \sum_{A=1}^{N_{\mathrm{shl}}} \mathrm{N}_A(\xi_1, \xi_2) \, \mathbf{d}_A , \tag{3.5}$$

where the positions of the NURBS control points $\mathbf{d}_A$ are the new generalized DOFs of the discrete formulation.

Remark With a slight abuse of notation, in the following sections and in Chapter 4, the approximate position vector of a material point on the shell midsurface is simply denoted as $\mathbf{x}^h$ instead of $\mathbf{x}_0^h$.

The basic semi-discrete variational form of the Kirchhoff–Love shell governing equations may be stated as follows: Given the trial-function set S_{x}^h and the test-function set S_{w}^h, here assumed to be comprised of NURBS basis functions, find the configuration $\mathbf{x}^h \in S_{\mathrm{x}}^h$ of the shell midsurface such that $\forall\ \mathbf{w}^h \in S_{\mathrm{w}}^h$,

$$\begin{aligned} &\int_{\Gamma_0^s} \mathbf{w}^h \cdot \rho_0 h_{th} \left(\frac{d^2 \mathbf{x}^h}{dt^2} - \mathbf{f}^h \right) \mathrm{d}\Gamma \\ +&\int_{\Gamma_0^s} \delta \overline{\boldsymbol{\varepsilon}}^h \cdot \left(\mathbf{K}^{\mathrm{exte}} \overline{\boldsymbol{\varepsilon}}^h + \mathbf{K}^{\mathrm{coup}} \overline{\boldsymbol{\kappa}}^h \right) \mathrm{d}\Gamma \\ +&\int_{\Gamma_0^s} \delta \overline{\boldsymbol{\kappa}}^h \cdot \left(\mathbf{K}^{\mathrm{coup}} \overline{\boldsymbol{\varepsilon}}^h + \mathbf{K}^{\mathrm{bend}} \overline{\boldsymbol{\kappa}}^h \right) \mathrm{d}\Gamma \\ -&\int_{(\Gamma_t^s)_h} \mathbf{w}^h \cdot \mathbf{h}^h \, \mathrm{d}\Gamma = 0 \,, \end{aligned} \tag{3.6}$$

where the Γ_0^s and Γ_t^s represent the shell midsurface in the reference and current configuration, respectively, ρ_0 is the through-thickness averaged density, $\mathbf{f}^h$ is the vector of the body forces per unit mass, $\overline{\boldsymbol{\varepsilon}}^h$ and $\overline{\boldsymbol{\kappa}}^h$ are membrane-strain and curvature-change vectors, $\delta\overline{\boldsymbol{\varepsilon}}^h$ and $\delta\overline{\boldsymbol{\kappa}}^h$ are their respective variations, and $(\Gamma_t^s)_h$ represents the shell midsurface where traction forces $\mathbf{h}^h$ are applied. In addition, the matrices $\mathbf{K}^{\mathrm{exte}}$, $\mathbf{K}^{\mathrm{coup}}$ and $\mathbf{K}^{\mathrm{bend}}$ represent, respectively, the extensional, coupling, and bending stiffness, which result from the through-thickness integration of the stress terms. The integration is simplified according to the Classical Laminated Plate Theory (CLPT) [90], whereby the integrals are reduced to discrete summations over the laminate plies:

$$\begin{aligned} \mathbf{K}^{\mathrm{exte}} &= \int_{h_{th}} \overline{\mathbf{C}} \, \mathrm{d}\xi_3 = \sum_{k=1}^{n_{\mathrm{ply}}} \overline{\mathbf{C}}_k h_{th_k} \,, \\ \mathbf{K}^{\mathrm{coup}} &= \int_{h_{th}} \xi_3 \overline{\mathbf{C}} \, \mathrm{d}\xi_3 = \sum_{k=1}^{n_{\mathrm{ply}}} \overline{\mathbf{C}}_k h_{th_k} z_k \,, \\ \mathbf{K}^{\mathrm{bend}} &= \int_{h_{th}} \xi_3^2 \overline{\mathbf{C}} \, \mathrm{d}\xi_3 = \sum_{k=1}^{n_{\mathrm{ply}}} \overline{\mathbf{C}}_k \left(h_{th_k} z_k^2 + \frac{h_{th_k}^3}{12} \right) \,. \end{aligned} \tag{3.7}$$

In Equation (3.7) , h_{th_k} is the thickness of the k^{th} ply, while z_k is the distance of the ply midsurface from the laminate midsurface. For each ply k, the matrix $\overline{\mathbf{C}}_k$ is obtained through a transformation of the constitutive matrix $\widetilde{\mathbf{C}}_k$, which, for composite materials, is typically expressed in terms of the material axes oriented in the longitudinal (or fiber) and transverse (or matrix) directions. This transformation is defined as:

$$\overline{\mathbf{C}}_k = \mathbf{T}^T \left(\phi_k \right) \widetilde{\mathbf{C}}_k \mathbf{T} \left(\phi_k \right) \,, \tag{3.8}$$

where the transformation matrix $\mathbf{T}(\phi_k)$ arises due to a change of basis from the principal material axes to the local lamina coordinate system, and is given by

$$\mathbf{T}(\phi_k) = \begin{bmatrix} \cos^2\phi_k & \sin^2\phi_k & \cos\phi_k\sin\phi_k \\ \sin^2\phi_k & \cos^2\phi_k & -\cos\phi_k\sin\phi_k \\ -2\cos\phi_k\sin\phi_k & 2\cos\phi_k\sin\phi_k & \cos^2\phi_k - \sin^2\phi_k \end{bmatrix}, \tag{3.9}$$

where (ϕ_k) is the angle between the fiber direction in the k^{th} ply and the x_1-axis of the local Cartesian coordinate system.

Remark If the Kirchhoff–Love shell is employed to represent each individual ply in the laminate, which is a key idea of the present modeling approach, then the definitions of $\mathbf{K}^{\mathrm{exte}}$, $\mathbf{K}^{\mathrm{coup}}$, and $\mathbf{K}^{\mathrm{bend}}$ for each ply reduce to the classical expressions:

$$\begin{aligned} \mathbf{K}^{\mathrm{exte}} &= \int_{h_{th_k}} \overline{\mathbf{C}}\,\mathrm{d}\xi_3 = \overline{\mathbf{C}} h_{th_k}\,, \\ \mathbf{K}^{\mathrm{coup}} &= \int_{h_{th_k}} \xi_3\overline{\mathbf{C}}\,\mathrm{d}\xi_3 = 0\,, \\ \mathbf{K}^{\mathrm{bend}} &= \int_{h_{th_k}} \xi_3^2\overline{\mathbf{C}}\,\mathrm{d}\xi_3 = \overline{\mathbf{C}}\frac{h_{th_k}^3}{12}\,. \end{aligned} \tag{3.10}$$

However, it is sometime convenient, and computationally efficient, to use the so-called "ply grouping" approach, where it is implicitly assumed that delamination will not occur within a given group of plies. This is commonly done for groups of plies made of the same material and with the same fiber orientation. In that case, this group of plies, also called a sub-laminate, is approximated as a single Kirchhoff–Love shell with the extensional, coupling, and bending stiffnesses computed according to Equation (3.7).

3.2 Continuum damage modeling for composite shells

Typical intralaminar damage modes include matrix cracking, fiber pullout caused by failure of the fiber-matrix interface, and fiber kinking under compression, which is a form of local instability. While these failures occur at the microscale level, their effects at the macroscopic level are often described using a residual stiffness approach in the framework of CDM. The residual stiffness approach adopted in this work was originally proposed in [75], where the authors developed a relationship between the damage state and effective elastic properties of unidirectional fiber-reinforced composites with brittle matrix behavior. The model in [75] is based on the following assumptions:

- The material is an orthotropic continuum;
- The material is in the state of plane stress;
- The damage process does not affect the orthotropic nature of the material.

In what follows, we summarize the intralaminar damage model as presented in [72], and further developed for Isogeometric Kirchhoff–Love shells in [36]. The model postulates the existence of crack arrays that cause, in the damaged material, the reduction of the area through which the stresses are transmitted. In order to preserve the orthotropic nature of the material, these cracks arrays are assumed to lie on damage planes orthogonal to the fiber and matrix directions. The second Piola–Kirchhoff stress $\overline{\mathbf{S}}$, which is computed from Equation (3.3), is transformed into its effective counterpart $\widehat{\mathbf{S}}$ in order to take into account the reduction of the effective area as:

$$\begin{bmatrix} \widehat{S}_{11} \\ \widehat{S}_{22} \\ \widehat{S}_{12} \end{bmatrix} = \begin{bmatrix} \dfrac{1}{1-d_1} & 0 & 0 \\ 0 & \dfrac{1}{1-d_2} & 0 \\ 0 & 0 & \dfrac{1}{1-d_6} \end{bmatrix} \begin{bmatrix} \overline{S}_{11} \\ \overline{S}_{22} \\ \overline{S}_{12} \end{bmatrix}, \tag{3.11}$$

where d_1,d_2 and d_6 are the fiber, matrix, and shear damage indices that reside in the open interval $[0,1)$. The compliance matrix $\widetilde{\mathbf{H}}$ may be expressed as a function of the damage indices as (see [75]):

$$\widetilde{\mathbf{H}} = \frac{1}{D} \begin{bmatrix} \dfrac{1}{(1-d_1)\,E_1^0} & -\dfrac{\nu_{21}}{E_2^0} & 0 \\ -\dfrac{\nu_{12}}{E_1^0} & \dfrac{1}{(1-d_2)\,E_2^0} & 0 \\ 0 & 0 & \dfrac{1}{(1-d_6)\,G_{12}^0} \end{bmatrix}, \tag{3.12}$$

and its inverse leads to the material stiffness matrix $\widetilde{\mathbf{C}}$ given by:

$$\widetilde{\mathbf{C}} = \frac{1}{D} \begin{bmatrix} E_1^0\,(1-d_1) & E_1^0\nu_{21}\,(1-d_1)\,(1-d_2) & 0 \\ E_2^0\nu_{12}\,(1-d_1)\,(1-d_2) & E_2^0\,(1-d_2) & 0 \\ 0 & 0 & G_{12}^0 D\,(1-d_6) \end{bmatrix}, \tag{3.13}$$

where E_1^0, E_2^0, G_{12}^0 are the elastic moduli of the undamaged material, ν_{21} and ν_{12} are the Poisson's ratios, and $D = 1 - \nu_{21}\nu_{12}\,(1-d_1)\,(1-d_2)$. Prior to damage initiation, $d_1 = d_2 = d_6 = 0$, and $\widetilde{\mathbf{C}}$ coincides with the classical constitutive matrix for an orthotropic material. As damage initiates and evolves, the lamina stiffness is progressively reduced according to Equation (3.13). Damage initiation and evolution is discussed in what follows.

3.2.1 Damage initiation

The Hashin criteria for plane stress [47, 46] are used to indicate the onset of damage in a ply. These criteria, originally formulated for unidirectional composites, have been extensively used for the analysis of laminates, mostly due to the ease of implementation. More sophisticated criteria [89, 33] for the plane-stress state have been recently introduced to predict with better accuracy the failure modes of fiber reinforced composites, particularly under compressive loads. These criteria take into account orientation of the fracture planes, which are assumed to be fixed in the approach adopted here, misalignment of the fibers, and the constraining interactions between the lamina. The latter, commonly referred to as the *in-situ* effect, has been shown in [97] to increase the strength of individual plies when these are located between the lamina with different fiber orientations. We note that the so-called LaRC03 criterion [33] for matrix cracking under compressive loading coincides with the corresponding Hashin criterion whenever the fracture plane is assumed to be oriented at a constant angle of 45°.

Two fiber-dominated and two matrix-dominated, independent intralaminar damage modes are considered in the present work, namely,

- Mode 1_T: fiber breaking under tension;
- Mode 1_C: fiber buckling under compression;
- Mode 2_T: matrix cracking under traverse tension and shear;
- Mode 2_C: matrix cracking under traverse compression and shear.

One failure index is associated with each failure mode. We mark the failure indices with an integer subscripts to indicate fiber (1) or matrix (2) direction, and with a letter subscript to indicate if the failure occurs under tensile (T) or compressive (C) stress conditions. The failure indices F_{1_T}, F_{1_C},

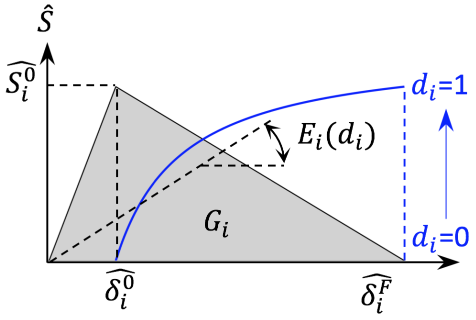

Figure 3.1: Illustration of the bi-linear softening model. In the figure, E_i^0 and E_i are the elastic moduli of the material in an undamaged and damaged state, respectively.

F_{2_T}, and F_{2_C} are computed from the effective stresses as follows:

$$\begin{aligned}
&\text{Mode } 1_T: \quad F_{1_T} = \left(\frac{\widehat{S}_{11}}{X_T}\right)^2 + \alpha\left(\frac{\widehat{S}_{12}}{Z_L}\right)^2 ,\\
&\text{Mode } 1_C: \quad F_{1_C} = \left(\frac{\widehat{S}_{11}}{X_C}\right)^2 ,\\
&\text{Mode } 2_T: \quad F_{2_T} = \left(\frac{\widehat{S}_{22}}{Y_T}\right)^2 + \left(\frac{\widehat{S}_{12}}{Z_L}\right)^2 ,\\
&\text{Mode } 2_C: \quad F_{2_C} = \left(\frac{\widehat{S}_{22}}{Y_C}\right)^2 + \left(\frac{\widehat{S}_{12}}{Z_L}\right)^2 ,
\end{aligned} \tag{3.14}$$

where X_T and X_C are the fiber strengths under tensile and compressive conditions, Y_T and Y_C are the matrix strengths under tensile and compressive conditions, while Z_L is the shear strength. The Hashin equation for the Mode 2_C criterion includes also the effect of transverse shear, which was neglected in Equation (3.14) since it is identically zero under the hypothesis of Kirchhoff–Love shell theory. If the parameter α is chosen to be equal to zero, according to the original Hashin criterion [47], the effect of in-plane shear stress is neglected for the tensile fiber failure. However, in the updated version of the criterion [46], the coefficient α was set to 1.

3.2.2 Damage evolution

Once damage initiation occurs, we use a bi-linear softening model, as shown in Figure 3.1, in order to compute the damage indices. Each damage mode is associated to a bi-linear curve, which allows us to compute the corresponding damage variables d_{1_T}, d_{1_C}, d_{2_T} and d_{2_C} as:

$$d_i = \frac{\hat{\delta}_i^F\left(\hat{\delta}_i - \hat{\delta}_i^0\right)}{\hat{\delta}_i\left(\hat{\delta}_i^F - \hat{\delta}_i^0\right)} , \tag{3.15}$$

where $\hat{\delta}_i$ represents the equivalent displacement for the i^{th} damage mode. The displacements $\hat{\delta}_i$ are computed from the strains as:

$$\begin{aligned}
\hat{\delta}_{1_T} &= L_c \langle \overline{\mathrm{E}}_{11} \rangle \, , \\
\hat{\delta}_{1_C} &= L_c \langle -\overline{\mathrm{E}}_{11} \rangle \, , \\
\hat{\delta}_{2_T} &= L_c \sqrt{\langle \overline{\mathrm{E}}_{22} \rangle^2 + \overline{\mathrm{E}}_{12}^2} \, , \\
\hat{\delta}_{2_C} &= L_c \sqrt{\langle -\overline{\mathrm{E}}_{22} \rangle^2 + \overline{\mathrm{E}}_{12}^2} \, ,
\end{aligned} \tag{3.16}$$

and the corresponding stresses are:

$$\begin{aligned}
\hat{S}_{1_T} &= \langle \hat{S}_{11} \rangle \, , \\
\hat{S}_{1_C} &= \langle -\hat{S}_{11} \rangle \, , \\
\hat{S}_{2_T} &= \frac{L_c \left(\langle \hat{S}_{22} \rangle \langle \overline{\mathrm{E}}_{22} \rangle + \langle \hat{S}_{12} \rangle \overline{\mathrm{E}}_{12} \right)}{\hat{\delta}_{2_T}} \, , \\
\hat{S}_{2_C} &= \frac{L_c \left(\langle -\hat{S}_{22} \rangle \langle -\overline{\mathrm{E}}_{22} \rangle + \langle \hat{S}_{12} \rangle \overline{\mathrm{E}}_{12} \right)}{\hat{\delta}_{2_C}} \, ,
\end{aligned} \tag{3.17}$$

where the symbol $\langle \cdot \rangle$ represents the Macaulay bracket. The characteristic length L_c is introduced to mitigate the dependency of the dissipated strain energy on the element size as proposed by Bažant [10]. We take $L_c = 2\sqrt{J}$, where $J = \|\mathbf{G}_1 \times \mathbf{G}_2\|$ is the surface Jacobian determinant of the transformation between the element parent and physical domains.

The displacement $\hat{\delta}_i^0$ and stress $\hat{S}_i^0$ corresponding to the onset of permanent damage are computed as:

$$\begin{aligned}
\hat{\delta}_i^0 &= \frac{\hat{\delta}_i}{\sqrt{F_i}} \, , \\
\hat{S}_i^0 &= \frac{\hat{S}_i}{\sqrt{F_i}} \, .
\end{aligned} \tag{3.18}$$

The equivalent displacement at failure $\hat{\delta}_i^F$ is computed by assuming that the strain energy required in order for the material to fail is equal to the fracture energy G_i of the i^{th} damage mode, namely,

$$\hat{\delta}_i^F = \frac{2\mathrm{G}_i}{\hat{S}_i^0} \, . \tag{3.19}$$

The equivalent displacements $\hat{\delta}_i^0$ and $\hat{\delta}_i^F$ are both computed only when the failure index reaches unity for the first time. Their values are then kept constant for the rest of the simulation, which also improves nonlinear convergence.

In order to enforce irreversibility of damage growth, the damage variables d_i's are forced to grow monotonically. At the k^{th} increment, the damage variable is computed as:

$$d_i^k = \max\left(d_i^{k-1}, \frac{\hat{\delta}_i^F\left(\hat{\delta}_i^k - \hat{\delta}_i^0\right)}{\hat{\delta}_i^k\left(\hat{\delta}_i^F - \hat{\delta}_i^0\right)}\right) . \tag{3.20}$$

In the above Equations (3.15), (3.18), (3.19), and (3.20), the index i takes on the values 1_T, 1_C, 2_T and 2_C. Finally, the damage indices d_1,d_2 and d_6 are computed from the damage variables d_{1_T}, d_{1_C}, d_{2_T} and d_{2_C} as:

$$\begin{aligned} d_1 &= \begin{cases} d_{1_T} & \text{if } \hat{S}_{11} \geq 0 \ , \\ d_{1_C} & \text{if } \hat{S}_{11} < 0 \ , \end{cases} \\ d_2 &= \begin{cases} d_{2_T} & \text{if } \hat{S}_{22} \geq 0 \ , \\ d_{2_C} & \text{if } \hat{S}_{22} < 0 \ , \end{cases} \\ d_6 &= 1 - \left(1 - d_{1_T}\right)\left(1 - d_{1_C}\right)\left(1 - d_{2_T}\right)\left(1 - d_{2_C}\right) \ . \end{aligned} \tag{3.21}$$

In the following chapters the membrane, coupling and stiffness matrices (i.e., $\mathbf{K}^{\text{exte}}$, $\mathbf{K}^{\text{coup}}$ and $\mathbf{K}^{\text{bend}}$) are explicitly expressed as functions of the damage variables $\boldsymbol{d}_{\text{var}} = [d_1, d_2, d_6]$ to specify that the modified constitutive stiffness matrix (3.13) is used in Equations (3.7) and (3.10).

3.2.3 Viscous regularization of the damage variables

The bi-linear softening law introduced for the degradation of the elastic properties exhibits a sharp transition from the linear-elastic regime to the damaged state. A viscous regularization scheme [72] is introduced in order to mitigate this effect and to also improve nonlinear convergence. The method is a generalization of the well-known Duvaut and Lions [38] regularization procedure. The scheme is defined in terms of the rate of change of the regularized variable, which is inversely proportional to a viscous parameter ρ^{mat}, namely,

$$\frac{d}{dt}\left(d_i^{\text{reg}}\right) = \frac{1}{\rho^{\text{mat}}}\left(d_i - d_i^{\text{reg}}\right) . \tag{3.22}$$

The regularization scheme is then implemented by using the backward Euler method for the time integration of Equation (3.22). Therefore, the regularized damage variables are given by

$$d_i^{\text{reg}}\left(t + \Delta t\right) = \frac{\Delta t}{\rho^{\text{mat}} + \Delta t} d_i\left(t + \Delta t\right) + \frac{\rho^{\text{mat}}}{\rho^{\text{mat}} + \Delta t} d_i^{\text{reg}}\left(t\right) \ , \tag{3.23}$$

where the index i, as before, take on the values 1_T, 1_C, 2_T, and 2_C. When the viscous parameter ρ^{mat} is negligible compared to the problem time scale, the regularized damage variable essentially coincides with the non-regularized one computed according to the procedure described in Section 3.2.2.

When the parameter ρ^{mat} grows, a *delay* is introduced in the growth of the damage variables. In the limit of $\rho^{\text{mat}} \to \infty$, the regularized damage variable essentially remains equal to its value defined at the initial time.

3.3 Cohesive interface model for Kirchhoff–Love shells

We introduce a zero-thickness cohesive interface model in the framework of Kirchhoff–Love shells in order to simulate the nucleation and progressive growth of the delamination front between adjacent plies. The proposed cohesive interface model, which defines an appropriate relationship between the ply-interface traction and separation, may be thought of as a penalty contact formulation (see e.g., [107]) enriched with an asymmetric multi-mode stiffness degradation law based on the cohesive properties of the laminate. The cohesive interface is introduced in the variational formulation given by Equation (3.6) by adding a ply interface traction proportional to the relative displacement jump between the initially connected lamina. The displacement jump term is integrated over the true ply interface and is defined consistently with the kinematics of the Kirchhoff–Love shell. The stiffness degradation law, which is based on the Mixed-Mode Cohesive Model (MMCM) presented in [103, 104], is then introduced to determine the elastic and failure limits of the interface. The MMCM was shown in [103, 104] to give accurate prediction of delamination for a combination of in-plane (Mode II) and out-of-plane (Mode I) opening modes. The *asymmetric* stiffness degradation law allows for a different treatment of the interface in case the plies move away from or toward each other, and prevents the ply interpenetration.

We note that while transverse shear is neglected at the level of individual plies, the introduction of a cohesive interface model permits laminate-level transverse shear compliance. The cohesive interface formulation that is consistent with the kinematics of the Kirchhoff–Love shell and the resulting laminate-level transverse shear compliance present the main novelty of the proposed multi-layer modeling approach.

3.3.1 Cohesive interface term in the weak form

The variational formulation of the multi-layer Kirchhoff–Love shell that includes a cohesive interface model may be obtained by adding the following terms to the interface between the plies:

$$+ \int_{\Gamma_t^{\text{coh}}} \delta\boldsymbol{\delta}_n \cdot (1 - d_{\text{coh}})\, \mathrm{K}_n^{\text{coh}} \boldsymbol{\delta}_n \, \mathrm{d}\Gamma + \int_{\Gamma_t^{\text{coh}}} \delta\boldsymbol{\delta}_\tau \cdot (1 - d_{\text{coh}})\, \mathrm{K}_\tau^{\text{coh}} \boldsymbol{\delta}_\tau \, \mathrm{d}\Gamma \,, \tag{3.24}$$

where Γ_t^{coh} is the cohesive interface in the current configuration, $\boldsymbol{\delta}_n$ and $\boldsymbol{\delta}_\tau$ are the normal and tangential components of the displacement jump $\boldsymbol{\delta}$, and $\delta\boldsymbol{\delta}_n$ and $\delta\boldsymbol{\delta}_\tau$ are their variations. The

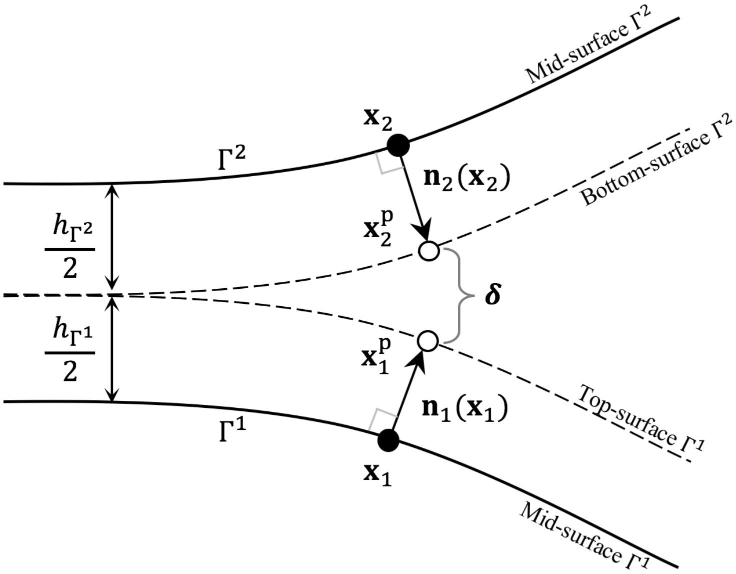

Figure 3.2: Schematic representation of two plies connected with a cohesive interface.

displacement jump is separated into the normal and tangential components to allow for a different treatment of the the normal and tangential opening modes. Also in Equation (3.24) $\mathrm{K}_n^{\mathrm{coh}}$ and $\mathrm{K}_\tau^{\mathrm{coh}}$ are the nominal stiffnesses in the normal and tangential directions, and d_{coh} is the damage variable.

The normal displacement jump δ_n is obtained by projecting δ in the direction orthogonal to the cohesive interface. We use the following definition for the effective interface normal vector $\tilde{\mathbf{n}}$,

$$\tilde{\mathbf{n}} = \frac{\mathbf{n}_1(\mathbf{x}_1) - \mathbf{n}_2(\mathbf{x}_2)}{||\mathbf{n}_1(\mathbf{x}_1) - \mathbf{n}_2(\mathbf{x}_2)||} , \tag{3.25}$$

where $\mathbf{n}_i(\mathbf{x}_i) \equiv \pm \bar{\mathbf{e}}_3^{\mathrm{cur}}(\mathbf{x}_i)$ is the unit vector pointing in the direction of the cohesive interface and orthogonal to the surface Γ^i, as illustrated in Figure 3.2. The normal and in-plane displacement jumps are therefore explicitly computed as:

$$\begin{aligned} \delta_{\mathrm{n}} &= (\tilde{\mathbf{n}} \otimes \tilde{\mathbf{n}})\, \delta \,, \\ \delta_\tau &= (\mathbf{I} - \tilde{\mathbf{n}} \otimes \tilde{\mathbf{n}})\, \delta \,. \end{aligned} \tag{3.26}$$

As explained in detail in Appendix A.2, the orthogonality of displacement jumps allows us to re-write the cohesive interface terms given by Equation (3.24) as a function of δ as:

$$\int_{\Gamma_t^{\mathrm{coh}}} \delta\delta \cdot (1 - d_{\mathrm{coh}}) \left[\mathrm{K}_n^{\mathrm{coh}} (\tilde{\mathbf{n}} \otimes \tilde{\mathbf{n}}) + \mathrm{K}_\tau^{\mathrm{coh}} (\mathbf{I} - \tilde{\mathbf{n}} \otimes \tilde{\mathbf{n}})\right] \delta \, \mathrm{d}\Gamma \,, \tag{3.27}$$

which, in turn, gives an implicit definition of the cohesive traction vector expressed in the global coordinate system,

$$\mathbf{t}^{\mathrm{coh}} = (1 - d_{\mathrm{coh}}) \left[\mathrm{K}_n^{\mathrm{coh}} \left(\tilde{\mathbf{n}} \otimes \tilde{\mathbf{n}} \right) + \mathrm{K}_\tau^{\mathrm{coh}} \left(\mathbf{I} - \tilde{\mathbf{n}} \otimes \tilde{\mathbf{n}} \right) \right] \delta \, . \tag{3.28}$$

The displacement jump is computed by using directly the kinematics of the Kirchhoff–Love shell. Employing the nomenclature of Figure 3.2, which shows two plies (labeled 1 and 2) connected with a cohesive interface, the spatial location $\mathbf{x}_1^{\mathrm{P}}$ of a point on the surface of ply 1 is computed as:

$$\mathbf{x}_1^{\mathrm{P}} = \mathbf{x}_1 + \frac{h_{\Gamma^1}}{2} \mathbf{n}_1 \left(\mathbf{x}_1 \right) \, , \tag{3.29}$$

where $\mathbf{x}_1$ is the spatial coordinate of the ply midsurface, h_{Γ^1} is the local thickness, and $\mathbf{n}_1$ is the normal vector. The spatial location $\mathbf{x}_2^{\mathrm{P}}$ of a point on the surface of ply 2 is computed analogously. The displacement jump on the cohesive interface is then naturally defined as:

$$\delta = \mathbf{x}_1^{\mathrm{P}} - \mathbf{x}_2^{\mathrm{P}} = \left[\left(\mathbf{x}_1 + \frac{h_{\Gamma^1}}{2} \mathbf{n}_1 \left(\mathbf{x}_1 \right) \right) - \left(\mathbf{x}_2 + \frac{h_{\Gamma^2}}{2} \mathbf{n}_2 \left(\mathbf{x}_2 \right) \right) \right] \, . \tag{3.30}$$

The above displacement jump is expressed in terms of the midsurface coordinates, local thicknesses, and normals of the adjacent plies. The variation of the displacement jump $\delta\delta$ may be computed as:

$$\delta\delta = \left[\left(\delta\mathbf{x}_1 + \frac{h_{\Gamma^1}}{2} \delta\mathbf{n}_1 \right) - \left(\delta\mathbf{x}_2 + \frac{h_{\Gamma^2}}{2} \delta\mathbf{n}_2 \right) \right] \, , \tag{3.31}$$

where, in the notation of Equation (3.6),

$$\delta\mathbf{x} = \mathbf{w} \, , \tag{3.32}$$

and

$$\delta\mathbf{n} = \frac{1}{\| \mathbf{x}_{,\xi_1} \times \mathbf{x}_{,\xi_2} \|} \left(\mathbf{I} - \mathbf{n} \otimes \mathbf{n} \right) \left[\left(\mathbf{w}_{,\xi_1} \times \mathbf{x}_{,\xi_2} \right) + \left(\mathbf{x}_{,\xi_1} \times \mathbf{w}_{,\xi_2} \right) \right] \, . \tag{3.33}$$

(See Appendix A.3 for the derivation of the above expression.) The final form of the cohesive interface terms is obtained by introducing Equations (3.30) and (3.31) into Equation (3.27), and using the expressions given by Equations (3.32) and (3.33).

Remark The cohesive interface formulation requires that the integration in Equation (3.27) is carried out over the surface Γ_t^{coh}. In practice, we do not define a cohesive interface surface explicitly. Instead, we carry out the integration of the terms involving $\delta\mathbf{x}_1$ and $\delta\mathbf{x}_2$ over the respective shell middle surfaces Γ^1 and Γ^2. As shown in Appendix A.4, this simplification introduces an error of $\mathcal{O}(h^2)$ in the evaluation of the surface Jacobian determinant. This is quite acceptable given that in the derivation of the Kirchhoff–Love shell theory itself the terms of $\mathcal{O}(h^2)$ are typically neglected.

3.3.2 Enforcement of the ply non-interpenetration condition

The structure of the cohesive interface formulation given by Equation (3.27) is that of a penalty method. Although the relative displacement of the plies is penalized, the penalty factor, which is proportional to $(1 - d_{\text{coh}})$, goes to zero when the cohesive interface fails. As a result, in that limit, the cohesive interface formulation is not able to prevent the non-physical interpenetration of the plies. In order to overcome this limitation, one can either develop an additional contact formulation, or introduce a modification to the cohesive interface stiffness degradation law, which is asymmetric with respect to the direction of the normal displacement jump.

In order to accomplish this, we first define the gap function $\bar{\delta}$ as:

$$\bar{\delta} = \left[\left(\mathbf{x}_1^{\mathrm{P}} - \mathbf{X}_1^{\mathrm{P}} \right) - \left(\mathbf{x}_2^{\mathrm{P}} - \mathbf{X}_2^{\mathrm{P}} \right) \right] \cdot \tilde{\mathbf{n}} \left(\mathbf{x}_1, \mathbf{x}_2 \right) \ . \tag{3.34}$$

The positive value of $\bar{\delta}$ indicates that the interface is closing. In this case, a repulsive force between the plies needs to be applied in the direction normal to the cohesive interface. In addition, because this force is due to contact only, its magnitude needs to be independent of the value of the cohesive-damage variable d_{coh}. To reflect this design, we replace the symmetric cohesive interface formulation given by Equation (3.27) by its asymmetric counterpart as:

$$\int_{\Gamma_t^{\text{coh}}} \delta\boldsymbol{\delta} \cdot \mathbf{t}^{\text{coh}} \, \mathrm{d}\Gamma = \begin{cases} \displaystyle\int_{\Gamma_t^{\text{coh}}} \delta\boldsymbol{\delta} \cdot (1 - d_{\text{coh}}) \left[\mathrm{K}_n^{\text{coh}} \left(\tilde{\mathbf{n}} \otimes \tilde{\mathbf{n}} \right) + \mathrm{K}_\tau^{\text{coh}} \left(\mathbf{I} - \tilde{\mathbf{n}} \otimes \tilde{\mathbf{n}} \right) \right] \boldsymbol{\delta} \, \mathrm{d}\Gamma & \text{if } \bar{\delta} \leq 0 \quad , \\ \displaystyle\int_{\Gamma_t^{\text{coh}}} \delta\boldsymbol{\delta} \cdot \left[\mathrm{K}_n^{\text{coh}} \left(\tilde{\mathbf{n}} \otimes \tilde{\mathbf{n}} \right) + (1 - d_{\text{coh}}) \mathrm{K}_\tau^{\text{coh}} \left(\mathbf{I} - \tilde{\mathbf{n}} \otimes \tilde{\mathbf{n}} \right) \right] \boldsymbol{\delta} \, \mathrm{d}\Gamma & \text{if } \bar{\delta} > 0 \quad . \end{cases} \tag{3.35}$$

3.3.3 Mixed-mode cohesive model

We describe a mixed-mode cohesive model employed in this work. MMCM gives an evolution law for a single damage variable d_{coh}, and assumes that the damage growth is related to a suitable combination of all the interface-traction components. We begin with a definition of the mixed-mode displacement jump δ_m,

$$\delta_m = \begin{cases} \sqrt{\delta_{\mathrm{n}}^2 + \delta_\tau^2} & \text{if } \bar{\delta} \leq 0, \\ |\delta_\tau| & \text{if } \bar{\delta} > 0 \quad , \end{cases} \tag{3.36}$$

where δ_{n} and δ_τ are the magnitudes of the displacement jumps defined in Equation (3.26). The definition of δ_m depends on the sign of the gap function. In the case of interface closing, only the tangential component contributes to the total displacement jump.

Turon et al. [103] proposed damage initiation criteria in the framework of the MMCM which ensures, for any generic mixed-mode opening condition, a smooth transition from the initiation to propagation of damage. The initiation of delamination is defined in terms of the equivalent displacement jump δ_m^0 given by

$$\delta_m^0 = \sqrt{(\delta_\mathrm{n}^0)^2 + \left((\delta_\tau^0)^2 - (\delta_\mathrm{n}^0)^2\right)\left(\frac{\beta^2}{1+2\beta^2-2\beta}\right)^\eta}\,, \tag{3.37}$$

which corresponds to the onset of permanent cohesive interface damage. Here,

$$\begin{aligned} \delta_\mathrm{n}^0 &= \frac{\mathrm{t}_\mathrm{n}^0}{\mathrm{K}_n^\mathrm{coh}}\,, \\ \delta_\tau^0 &= \frac{\mathrm{t}_\tau^0}{\mathrm{K}_\tau^\mathrm{coh}}\,, \end{aligned} \tag{3.38}$$

are the displacement-jump values where the delamination is initiated under pure normal and tangential opening modes, respectively, with t_n^0 and t_τ^0 denoting the corresponding cohesive strengths. Also in Equation (3.37) the semi-empirical, material-specific parameter η is employed to fit the experimental data obtained under mixed-mode opening conditions, while the mixed-mode ratio β is a relative weight for the resultant opening mode defined as a function of the normal and tangential displacement jumps as:

$$\beta = \begin{cases} \dfrac{\delta_\tau}{\delta_\tau + \delta_\mathrm{n}} & \text{if } \bar{\delta} \le 0 \quad , \\ 1, & \text{if } \bar{\delta} > 0 \quad . \end{cases} \tag{3.39}$$

Failure of the cohesive interface occurs according to the Benzeggagh and Kenane [18] damage evolution criterion, which states that the interface fails when the current energy release rate reaches the value of the critical energy release rate, namely,

$$\sum_{i=1}^{3} \mathrm{G}_i \ge \mathrm{G}_{\mathrm{c_n}} + (\mathrm{G}_{\mathrm{c}_\tau} - \mathrm{G}_{\mathrm{c_n}})\left(\frac{\beta^2}{1+2\beta^2-2\beta}\right)^\eta\,, \tag{3.40}$$

where G_i's are the critical energy release rates under pure i^{th}-mode opening. The equivalent displacement jump δ_m^F, corresponding to failure of the cohesive interface, is then obtained for a generic mixed-mode ratio [103] as:

$$\delta_m^F = \frac{\delta_\mathrm{n}^0\delta_\mathrm{n}^F + \left(\delta_\tau^0\delta_\tau^F - \delta_\mathrm{n}^0\delta_\mathrm{n}^F\right)\left(\dfrac{\beta^2}{1+2\beta^2-2\beta}\right)^\eta}{\delta_m^0}\,, \tag{3.41}$$

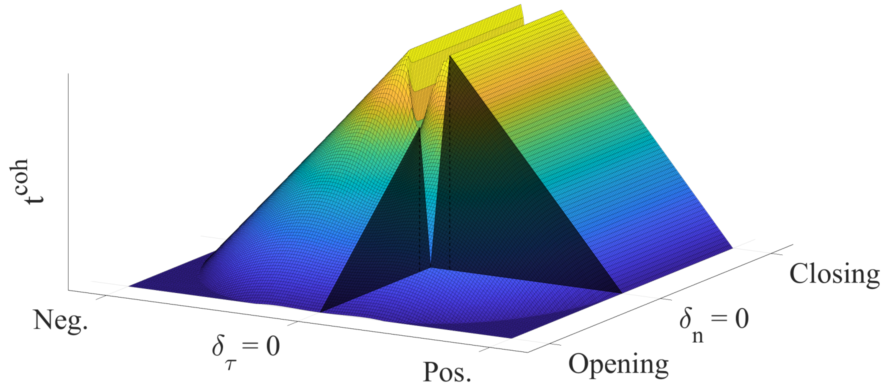

Figure 3.3: Graphical depiction of the MMCM.

where

$$\begin{aligned} \delta_{\mathrm{n}}^F &= \frac{2\mathrm{G}_{\mathrm{n}}}{\mathrm{t}_{\mathrm{n}}^0}, \\ \delta_\tau^F &= \frac{2\mathrm{G}_\tau}{\mathrm{t}_\tau^0}, \end{aligned} \tag{3.42}$$

are the displacement jumps corresponding to a complete failure of the interface under pure normal and tangential opening mode, respectively, with G_{n} and G_τ denoting the respective fracture toughness values. The pure opening Mode I (normal) and Mode II (tangential) are therefore included in the MMCM when $\beta = 0$ and $\beta = 1$, respectively. (See Equations (3.37) and (3.41), where it is clear that for $\beta = 0$, $\delta_m^0 = \delta_{\mathrm{n}}^0$ and $\delta_m^F = \delta_{\mathrm{n}}^F$, while for $\beta = 1$, $\delta_m^0 = \delta_\tau^0$ and $\delta_m^F = \delta_\tau^F$.)

Graphical depiction of the MMCM is shown in Figure 3.3, where the traction is computed as a function of the normal and tangential displacement jumps. The shaded triangles represent bilinear degradation law for pure Mode I and Mode II openings. It is clear from the figure that, if the interface is closing, the degradation of the cohesive interface is only a function of the tangential displacement jump.

From Equations (3.37) and (3.41) one infers that, under mixed-mode opening, both the initial and failure displacement jumps are not constant, but are functions of the current mixed-mode ratio. Nevertheless, one must ensure that the damage growth is irreversible in order to prevent non-physical recovery of the cohesive interface elastic properties. This condition is satisfied by choosing appropriate values for the normal and tangential interface strengths. Turon et al. [104] showed that, for a cohesive interface with mode-independent stiffness, irreversibility of damage is guaranteed by choosing the tangential strength as:

$$\mathrm{t}_\tau^0 = \mathrm{t}_{\mathrm{n}}^0 \sqrt{\frac{G_{c_\tau}}{G_{c_{\mathrm{n}}}}}\,. \tag{3.43}$$

In the present work, the normal and tangential stiffnesses are assumed to be equal, and we set $\mathrm{K}_n^{\mathrm{coh}} = \mathrm{K}_\tau^{\mathrm{coh}} = \mathrm{K}^{\mathrm{coh}}$. The discussion of how $\mathrm{K}^{\mathrm{coh}}$ is selected is provided later in the chapter. Finally, in order to numerically enforce the irreversible damage growth condition, the mixed-mode damage variable at the k^{th} analysis step is computed as:

$$d_{\mathrm{coh}}^{k} = \max\left(d_{\mathrm{coh}}^{k-1}, \frac{\delta_m^{F^k}\left(\delta_m^k - \delta_m^{0^k}\right)}{\delta_m^k\left(\delta_m^{F^k} - \delta_m^{0^k}\right)} \right) . \tag{3.44}$$

Analogously to intralaminar damage, viscous regularization of the cohesive damage variable is also introduced in order to mitigate the effects of rapid changes in the cohesive stiffness induced by the softening law. The regularized cohesive damage variable is assumed to satisfy the differential equation

$$\frac{d}{dt}\left(d_{\mathrm{coh}}^{\mathrm{reg}}\right) = \frac{1}{\rho^{\mathrm{coh}}}\left(d_{\mathrm{coh}} - d_{\mathrm{coh}}^{\mathrm{reg}}\right) , \tag{3.45}$$

which is, in turn, integrated using the Backward Euler method. (See Section 3.2.3 for details.)

3.4 Discrete formulation and numerical aspects

For a laminated composite structure comprised of Np plies (or sublaminates in the case of ply grouping) and Nc cohesive interfaces, the semi-discrete variational formulation may be stated as follows: Find the configuration $\mathbf{x}^h \in S_{\mathrm{x}}^h$, such that, $\forall \mathbf{w}^h \in S_{\mathrm{w}}^h$,

$$\begin{aligned}
\sum_{ip=1}^{Np} \quad & \left\{ \int_{\left(\Gamma_0^S\right)_{ip}} \mathbf{w}^h \cdot \rho_{0_{ip}} h_{th_{ip}} \left(\frac{d^2\mathbf{x}^h}{dt^2} - \mathbf{f}^h \right) \mathrm{d}\Gamma \right. \\
& + \int_{\left(\Gamma_0^S\right)_{ip}} \delta\overline{\boldsymbol{\varepsilon}}^h \cdot \left(\mathbf{K}_{ip}^{\mathrm{exte}}\left(\boldsymbol{d}_{\mathrm{var}_{ip}}\right)\overline{\boldsymbol{\varepsilon}}^h + \mathbf{K}_{ip}^{\mathrm{coup}}\left(\boldsymbol{d}_{\mathrm{var}_{ip}}\right)\overline{\boldsymbol{\kappa}}^h \right) \mathrm{d}\Gamma \\
& + \int_{\left(\Gamma_0^S\right)_{ip}} \delta\overline{\boldsymbol{\kappa}}^h \cdot \left(\mathbf{K}_{ip}^{\mathrm{coup}}\left(\boldsymbol{d}_{\mathrm{var}_{ip}}\right)\overline{\boldsymbol{\varepsilon}}^h + \mathbf{K}_{ip}^{\mathrm{bend}}\left(\boldsymbol{d}_{\mathrm{var}_{ip}}\right)\overline{\boldsymbol{\kappa}}^h \right) \mathrm{d}\Gamma \\
& \left. - \int_{\left(\Gamma_t^S\right)_h} \mathbf{w}^h \cdot \mathbf{h}^h \, \mathrm{d}\Gamma \right\} \\
+ \sum_{ic=1}^{Nc} \quad & \left\{ \int_{\left(\Gamma_t^{\mathrm{coh}}\right)_{ic}} \left[\left(\mathbf{w}_{1_{ic}}^h + \frac{h_{\Gamma^{1_{ic}}}}{2}\delta\mathbf{n}_{1_{ic}}^h \right) - \left(\mathbf{w}_{2_{ic}}^h + \frac{h_{\Gamma^{2_{ic}}}}{2}\delta\mathbf{n}_{2_{ic}}^h \right) \right] \cdot \mathbf{t}^{\mathrm{coh}} \, \mathrm{d}\Gamma \right\} = 0 \, .
\end{aligned} \tag{3.46}$$

In the above formulation the trial and test function sets are, as before, comprised of NURBS basis functions, however, *the sets are defined on each ply, and are discontinuous from ply to ply*. In the cohesive interface terms of the of the above formulation the subscripts 1_{ic} and 2_{ic} are consistent with the notation introduced in Section 3.3.1. The intralaminar CDM presented in Section 3.2 is implicitly embedded in the definition of the extensional, coupling, and bending stiffness matrices of each ply, and automatically accounts for their current damage state.

The Generalized-α method [31], which is an enhancement of the HHT-α method [49, 57] that enables control over high-frequency dissipation, is used for the time integration of the semi-discrete formulation given by Equation (3.46). We adopt a predictor-multicorrector algorithm [32, 15], which, at every time-step, solves the following system of nonlinear equations:

$$\mathbf{R}(\ddot{\mathbf{d}}_{n+\alpha_m}, \dot{\mathbf{d}}_{n+\alpha_f}, \mathbf{d}_{n+\alpha_f}) = \mathbf{0} \, . \tag{3.47}$$

Here, $\mathbf{R}$ is the discrete control-point residual, $\mathbf{d}$ is the vector of control-point position unknowns, $\dot{\mathbf{d}}$ and $\ddot{\mathbf{d}}$ are its first and second time derivatives, respectively. Equation 3.47 can be written explicitly as:

$$\mathbf{F}^{\text{mass}}\left(\ddot{\mathbf{d}}_{n+\alpha_m}\right) + \mathbf{F}^{\text{damp}}\left(\dot{\mathbf{d}}_{n+\alpha_f}\right) + \mathbf{F}^{\text{int}}\left(\mathbf{d}_{n+\alpha_f}\right) - \mathbf{F}^{\text{ext}}\left(\mathbf{d}_{n+\alpha_f}\right) = \mathbf{0} \, , \tag{3.48}$$

where $\mathbf{F}^{\text{mass}}$ is the vector of inertial forces coming from the discretization of the acceleration terms, $\mathbf{F}^{\text{int}}$ are the internal forces obtained from the discretization of the internal stress and cohesive interface terms, $\mathbf{F}^{\text{ext}}$ is the vector of external forces obtained from the discretization of body-force and surface-traction terms. In addition, although this term is not explicitly part of Equation (3.46), $\mathbf{F}^{\text{damp}}$ represents the vector of forces due to damping, which may be included in the formulation. Equation (3.47) states that the discrete residual is collocated using acceleration evaluated at the intermediate time level $n + \alpha_m$ and velocity and position evaluated at the intermediate time level $n + \alpha_f$, where the α levels are chosen to ensure second-order accuracy and unconditional stability of the algorithm (see [31] for more details.)

The nonlinear-equation system is solved using the Newton–Raphson method, which involves, at every nonlinear iteration, solution of a linear-equation system given by

$$\frac{d\mathbf{R}^i}{d\ddot{\mathbf{d}}_{n+1}} \Delta\ddot{\mathbf{d}}_{n+1} = -\mathbf{R}^i_{n+1} \, , \tag{3.49}$$

where i is the nonlinear-iteration index and $\Delta\ddot{\mathbf{d}}_{n+1}$ is the acceleration increment. In Equation (3.49), $\frac{d\mathbf{R}^i}{d\ddot{\mathbf{d}}_{n+1}}$ is the tangent matrix, which may be expressed as:

$$\begin{aligned} \frac{d\mathbf{R}^i}{d\ddot{\mathbf{d}}_{n+1}} &= \frac{\partial\mathbf{R}^i}{\partial\ddot{\mathbf{d}}_{n+\alpha_m}} \frac{\partial\ddot{\mathbf{d}}_{n+\alpha_m}}{\partial\ddot{\mathbf{d}}_{n+1}} + \frac{\partial\mathbf{R}^i}{\partial\dot{\mathbf{d}}_{n+\alpha_f}} \frac{\partial\dot{\mathbf{d}}_{n+\alpha_f}}{\partial\dot{\mathbf{d}}_{n+1}} \frac{\partial\dot{\mathbf{d}}_{n+1}}{\partial\ddot{\mathbf{d}}_{n+1}} + \frac{\partial\mathbf{R}^i}{\partial\mathbf{d}_{n+\alpha_f}} \frac{\partial\mathbf{d}_{n+\alpha_f}}{\partial\mathbf{d}_{n+1}} \frac{\partial\mathbf{d}_{n+1}}{\partial\ddot{\mathbf{d}}_{n+1}} \\ &= \frac{\partial\mathbf{R}^i}{\partial\ddot{\mathbf{d}}_{n+\alpha_m}} \alpha_m + \frac{\partial\mathbf{R}^i}{\partial\dot{\mathbf{d}}_{n+\alpha_f}} \alpha_f \gamma \Delta t + \frac{\partial\mathbf{R}^i}{\partial\mathbf{d}_{n+\alpha_f}} \alpha_f \beta \Delta t^2 \\ &= \mathbf{M}\alpha_m + \mathbf{C}\alpha_f\gamma\Delta t + \mathbf{K}\alpha_f\beta\Delta t^2 \, , \end{aligned} \tag{3.50}$$

where γ and β are the additional parameters of the Generalized-α scheme arising in the well-known Newmark formulae, and $\mathbf{M}$, $\mathbf{C}$, and $\mathbf{K}$ are the mass, damping, and tangent stiffness matrices.

Remark Particular attention is required for the evaluation of the tangent stiffness matrix coming from the cohesive interface terms because they give rise to the coupling of the degrees of freedom coming from the adjacent plies. If a sparse-matrix data structure is employed, it needs to be able to accommodate these *cross-stiffness* terms.

3.5 Numerical examples

In this section the proposed multi-layer shell formulation is tested on a set of benchmark examples. The first two numerical examples simulate the Double Cantilever Beam (DCB) and End Notched Flexure (ENF) tests. DCB and ENF tests are standard experimental procedures to measure the interlaminar fracture toughness for pure Mode I and Mode II opening, respectively, and are widely employed to validate cohesive models in their ability to predict delamination under simple loading conditions. Numerical results are compared with analytical models developed in the framework of Linear Elastic Fracture Mechanics (LEFM). The LEFM close-form solutions for the DCB and ENF tests are derived by Mi et al. [77]. Because the LEFM solutions model each of the DCB and ENF legs as beams, in order to obtain numerical results consistent with the theoretical predictions, we model the legs as isotropic IGA shells with zero Poisson ratio and using a single element in the lateral direction. The inertial effects are also disregarded since the tests are performed under quasi-static loading conditions.

The third numerical example involves a thick composite laminated plate subjected to a point load applied at its center. Following the approach proposed in the dissertation, the laminate is modeled ply by ply, and the lamina are connected through cohesive interfaces. The purpose of this example is to examine the ability of the multi-layer model, developed in the framework of Kirchhoff–Love shell theory at the ply-level, to effectively represent transverse-shear behavior at the overall laminate level. Here the comparisons are made with the solution generated in the framework of First-Order Shear Deformation Theory (FSDT), commonly referred as the Reissner–Mindlin shell theory.

For all the simulations presented in this section we use C^1-continuous quadratic NURBS. In addition, in the computations presented, we do not account for intralaminar damage. The latter is tested in the context of impact simulations presented in Chapter 4 of this dissertation.

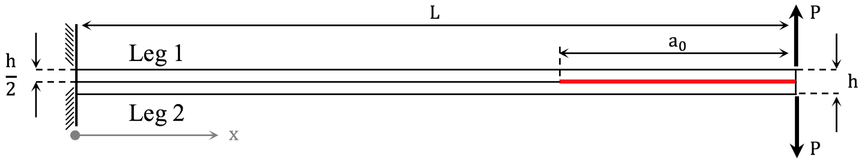

Figure 3.4: Schematic representation of the DCB test with two legs. The initially delaminated region of size a_0 is marked in red.

3.5.1 Validation of the cohesive model: DCB test

The DCB test is used to validate the cohesive model under pure Mode I opening, where the delamination propagates due to opening of the plies in the direction orthogonal to their interface. The configuration of the DCB test [104] is schematically represented in Figure 3.4. The overall specimen length is $L = 150$ mm, the lateral dimension is $b = 20$ mm, and the thickness of each leg is $h/2 = 1.55$ mm. The length of the initially delaminated region is $a_0 = 35$ mm.

Table 3.1: Specimen material properties for the DCB test.

E[GPa]	ν	$\mathrm{K}^{\mathrm{coh}}$ [N/mm^3]	$\mathrm{t}_{\mathrm{n}}^{0}$ [N/mm^2]	$G_{\mathrm{C_n}}$ [N/mm]	G_{C_τ} [N/mm]
120.0	0.0	5×10^6	30.0 - 120.0	0.26	1.002

The elastic and cohesive interface material properties for the DCB test chosen for a typical carbon/epoxy composite, and are summarized in Table 3.1. Mode I critical strain energy release rate, being a well-documented, measured property, is kept constant for all the DCB test simulations. The cohesive penalty stiffness $\mathrm{K}^{\mathrm{coh}}$ is chosen large enough to not introduce any significant compliance in the model. Several simulations have been performed by increasing the value of $\mathrm{K}^{\mathrm{coh}}$ until the force-displacement curve no longer exhibits significant variations. The value chosen for the DCB test is $\mathrm{K}^{\mathrm{coh}} = 5 \times 10^6$ N/mm^3. A range of values for the normal cohesive strength $\mathrm{t}_{\mathrm{n}}^{0}$ are tested in order to assess the sensitivity of the solution with respect to the maximum allowable traction at the interface. The tangential strength t_{τ}^{0} is computed according to Equation (3.43). The coefficient η in Equations 3.37 and 3.41 is set equal to 1. Viscous regularization of the cohesive damage variable is not used in the simulations of the DCB test.

We use a non-uniform mesh in the longitudinal direction for the discretization of the specimen due to high gradients near the crack front. It was shown in [105] that, in the case of linear FEM, three to ten elements are required in the direction of delamination propagation in order to accurately reproduce the interface behavior in the area from the crack tip to the point of maximum traction (1 mm length scale), where the stress gradient is large compared to the rest of the specimen. The extension of the this critical transition area is commonly referred to as *cohesive length*, and it

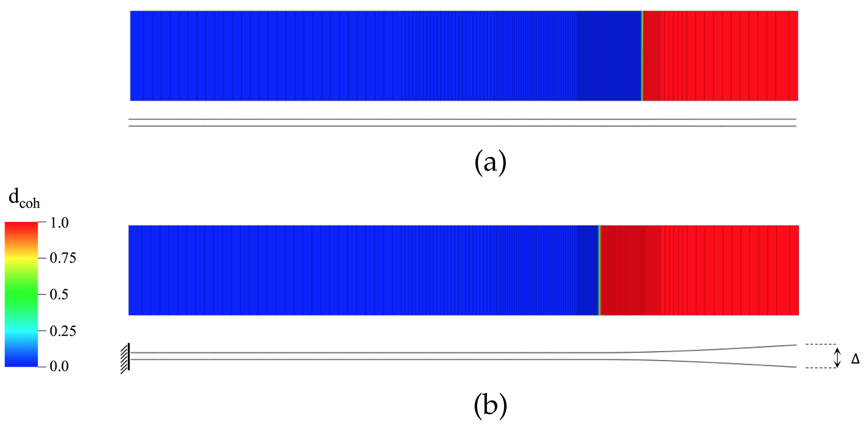

Figure 3.5: DCB test simulation. Top and side views of the specimen. (a) Initial configuration; (b) Configuration at relative displacement $\Delta = 3.5$ mm. Top view shows contours of the cohesive damage variable.

may be estimated a priori as [42]:

$$l^{\mathrm{coh}} = \frac{9}{32}\pi E \frac{G_{C_n}}{\left(t_n^0\right)^2} \,. \tag{3.51}$$

Given the parameters reported in Table 3.1, cohesive length corresponding to cohesive strength of $t_n^0 = 120\ \mathrm{N/mm^2}$ is $l^{\mathrm{coh}} = 1.91$ mm. Therefore, the mesh is designed such that the element size is 0.2 mm ($\approx 10\%$ of l^{coh}) inside the delamination propagation region and 2 mm outside away from this region.

We followed the same semi-heuristic criteria formulated in the framework of linear FEM for the estimation of the critical element size. However, the higher-order accuracy and continuity of the field variables introduced by the NURBS discretization admits a possibility of using coarser discretizations without sacrificing the accuracy and stability of the analysis. Impact simulations presented in Chapter 4 of this dissertation partially support this claim. However, the use of higher-order and higher-continuity discretizations in the context of cohesive-zone modeling is not at all common, and requires a separate investigation.

In our simulations, cohesive interface extends along the entire length of the specimen. In the beginning of the simulation, the damage variable d_{coh} is set to unity inside the initially delaminated area and zero elsewhere, as shown in Figure 3.5(a). In order to achieve a stable propagation of the delamination front [2], the simulations are performed under displacement-controlled conditions by imposing the displacement of the control points on the right edge of the specimen. The coupon is constrained by imposing a zero displacement boundary condition on the first two rows of control points at the left edge of the specimen, as shown in Figure 3.4. The configuration at relative prescribed displacement $\Delta = 3.5$ mm is shown in Figure 3.5(b).

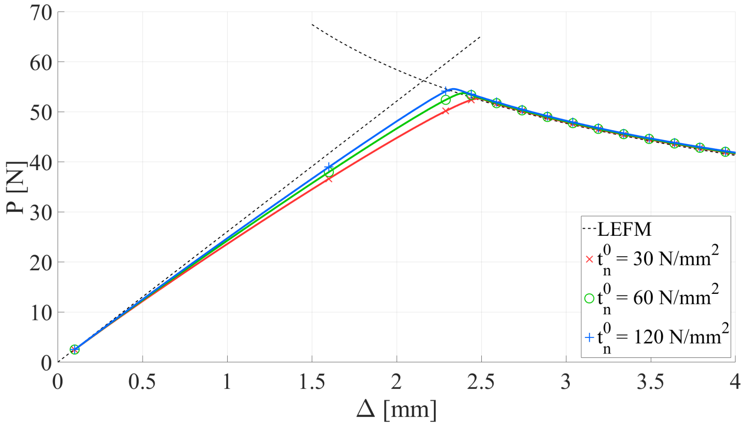

Figure 3.6: DCB test simulation. Load-displacement curves obtained for different interface strengths.

The force-displacement diagrams obtained from the simulations are compared with the LEFM solution and shown in Figure 3.6. The results are in close agreement with the beam theory based on the LEFM solution. As expected, a larger value of the interface strength results in a larger peak force at the initiation of delamination. However, no noticeable differences in the response are found during the delamination propagation stage.

Propagation of the delamination front is shown in Figure 3.7 for different levels of cohesive strength, where the cohesive traction (top panels) and damage variable (bottom panels) are plotted as a function of the longitudinal coordinate x (horizontal axis) and imposed displacement Δ (left axis). The contour plots show the distribution of $\mathrm{t}^{\mathrm{coh}}$ and of d_{coh} over a portion of the specimen, characterized by a longitudinal coordinate $x \in [100, 116]$ mm, where the delamination front propagates. A vertical read on the plot gives the evolution of $\mathrm{t}^{\mathrm{coh}}$ and d_{coh} as a function of the applied Δ for a material point of the specimen located at the coordinate x. Conversely, an horizontal read gives the distribution of $\mathrm{t}^{\mathrm{coh}}$ and d_{coh} along the specimen for a given applied displacement.

The delamination process starts when the energy release rate reaches the value corresponding to the toughness of the interface. The partially delaminated region, where $d_{\mathrm{coh}} \in \,]0, 1[$, is contained between the white and black dashed lines. The area to the right of the black dashed line corresponds to complete delamination. The delamination point is clearly denoted by a sharp change in the slope of the black dashed line at applied displacement nearing 2.5 mm.

Figure 3.7 shows that the size of partially delaminated region grows monotonically with the applied displacement until the start of the delamination process, then it remains constant. Note that lower values of the cohesive strength increase the size of the partially delaminated region. This effect can be more clearly observed in Figure 3.8 where the cohesive traction and damage variable are plotted as a function of the longitudinal coordinate for two applied displacement levels.

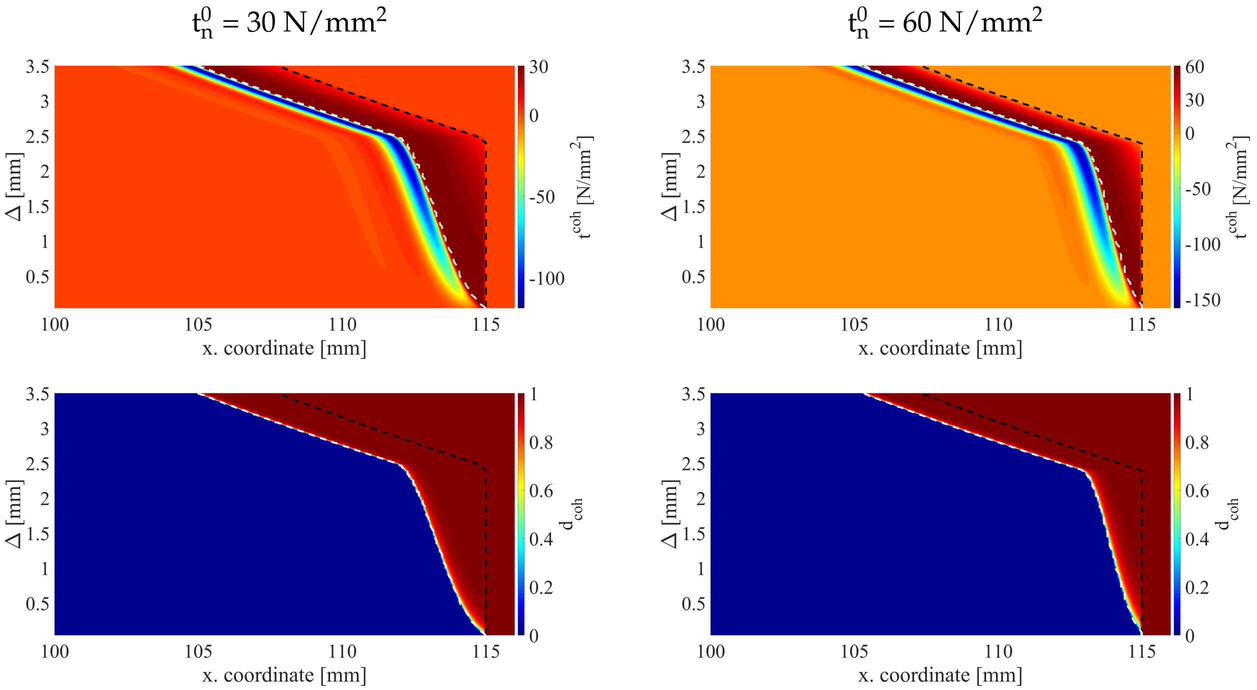

Figure 3.7: DCB test simulation. Cohesive traction (top) and damage variable d_{coh} (bottom) as a function of the displacement Δ and of the longitudinal coordinate. The region to the left of the white dashed line is characterized by d_{coh}=0, the region to the right of the black dashed line is characterized by d_{coh}=1. For the orientation of the longitudinal axis see Figure 3.4.

The figures show that the maximum cohesive traction does not exceed the value of the interface's strength, while the non-interpenetration traction are not bounded. It can also be inferred from the figure that the damage variable exhibits a sharp initial transition in the direction from the crack tip to the delaminated region, where it tends to slowly reach the asymptotic value of 1.

3.5.2 Validation of the cohesive model: ENF test

Simulation of the ENF test [77] is more challenging than the DCB test because the specimen exhibits a snapback instability (i.e., a positive slope of the load-deflection softening branch [25]) when the delamination begins to propagate. Furthermore, the computational model must be able to effectively handle the interaction between the legs in the fully delaminated region to prevent their interpenetration. The ENF-test configuration is shown in Figure 3.9. The length of the specimen is $L = 100$ mm, the width is $b = 1$ mm, and the thickness of each leg is $h/2 = 1.5$ mm. The length of the initially delaminated region is $a_0 = 30$ mm.

Material properties used in the ENF test are summarized in Table 3.2 for a typical carbon/epoxy composite. The Mode II fracture toughness a well-known value and thus is kept constant in the simulations. The specimen is discretized using a uniform mesh with element size

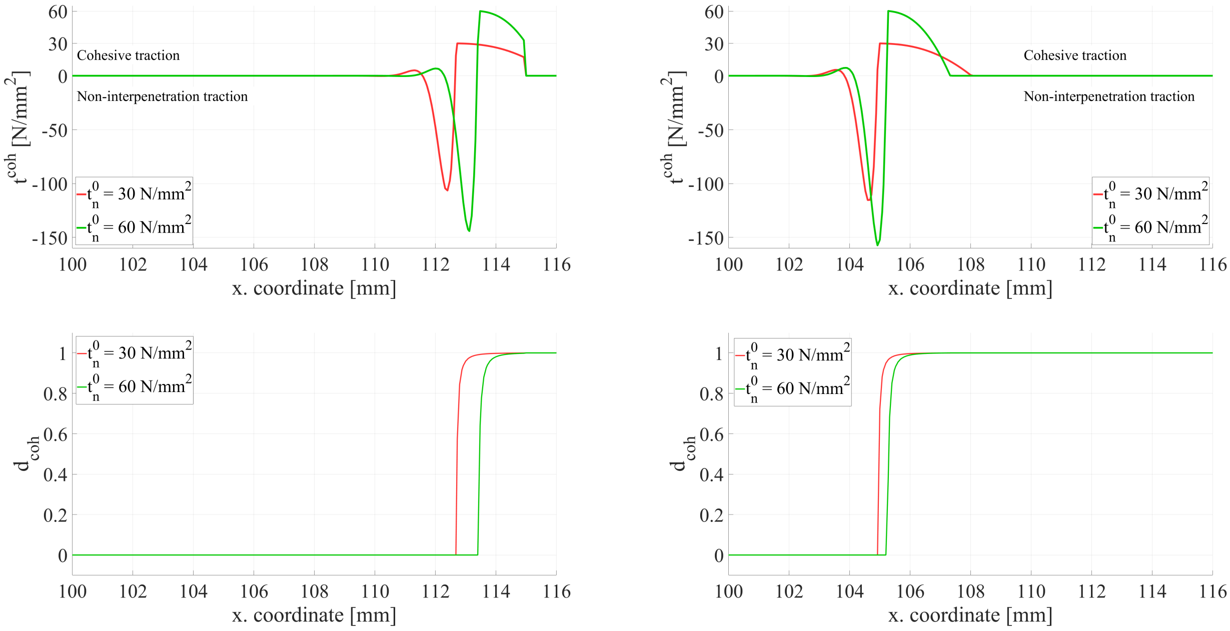

(a)

(b)

Figure 3.8: DCB test simulation. Cohesive traction (top) and damage variable d_{coh} (bottom) as a function of longitudinal coordinate at (a) Δ=2.0 mm and (b) Δ=3.5 mm.

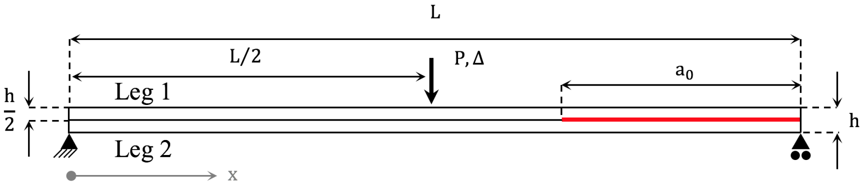

Figure 3.9: Schematic representation of the ENF test with two legs. The initially delaminated region is marked in red.

Table 3.2: Specimen material properties for the ENF test simulation.

E[GPa]	ν	K^{coh} [N/mm^3]	t_τ^0 [N/mm^2]	G_{C_n} [N/mm]	G_{C_τ} [N/mm]
135.3	0.0	1×10^4	80.0 - 160.0	0.268	4.0

of 0.8 mm. According to Equation (3.51), and with the assumption that the cohesive length is discretized using 10 elements, the adopted mesh is suitable for ENF analyses with a cohesive strength of $t_\tau^0 \leq 245$ N/mm^2. This mesh allows to satisfy the semi-heuristic criteria, which is formulated in the framework of linear FEM, with a manageable number of degrees of freedom. Therefore, no local mesh refinement is required.

The value chosen for the ENF test is $K^{coh} = 1 \times 10^4$ N/mm^3. The choice of the cohesive

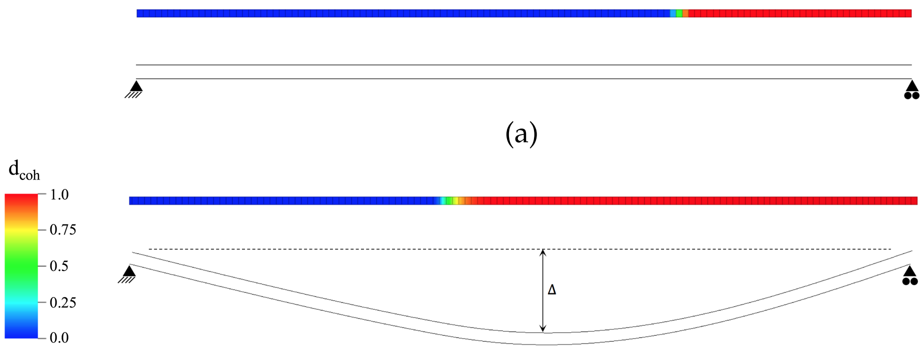

(a)

(b)

Figure 3.10: ENF test simulation. Top and side views of the specimen. (a) Initial configuration; (b) Configuration at relative displacement $\Delta = 10$ mm. Top view shows contours of the cohesive damage variable.

stiffness is discussed later in this chapter. Different values of the in-plane cohesive strength t_τ^0 are tested in order to assess the sensitivity of the solution with respect to maximum allowable traction at the interface. The normal strength t_n^0 is computed according to Equation (3.43). The coefficient η in Equation 3.37 is set equal to 1. For the simulations reported in this section, the regularization coefficient ρ_{coh} is set to 0. The effect of the viscous regularization of the cohesive damage variable is discussed later in the chapter.

The ENF test is simulated by imposing displacement of the control points at the centerline of the upper lamina. The right- and left-side boundary conditions constraining the specimen motion are imposed on the lower lamina, as shown in Figure 3.9. The deformed configuration at the end of the simulation is shown in Figure 3.10(b). Note that the cohesive interface correctly enforces the Kirchhoff condition on the left side of the specimen where the interface is undamaged. On the right side of the specimen, where the two beams are completely delaminated, the cohesive interface formulation allows relative sliding while preventing interpenetration.

Simulation results are compared with the LEFM solution in Figure 3.11. The theoretical load-displacement curve is comprised of three parts identified with (a) the initial linear-elastic response where the delamination does not propagate; (b) the unloading curve valid for crack length $a < L/2$; (c) the propagation curve valid for $a \geq L/2$. Because simulations in the present work are performed by imposing a monotonically increasing vertical displacement, the unloading part of the curve is not captured. One can do so by adopting an arc-length-type method [48, 77], where the load and displacement increments are computed as part of the numerical solution. We find that lower values of the cohesive strength result in a smoother transition from the elastic regime to the propagation of the delamination front, while the response predicted with larger values of the cohesive strength is closer to the analytical solution. Note that the response in the delamination

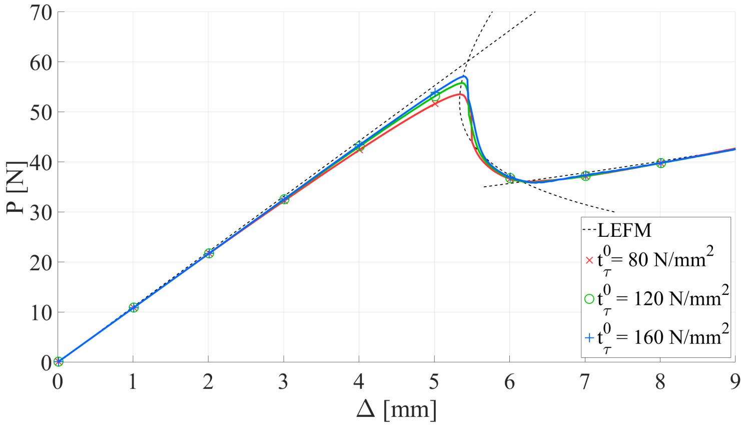

Figure 3.11: ENF test simulation. Load-displacement curves obtained for different interface strengths.

propagation region is independent of the choice of the cohesive strength.

3.5.3 Comparison with Reissner–Mindlin shear-deformable theory

In the proposed multi-layer approach, the model of individual plies is based on the Kirchhoff–Love thin shell theory, which individually do not account for transverse shear deformation. Despite the many numerical advantages of this approach, one may argue that the ability of the model to represent all the key deformation modes is reduced with the increasing shell thickness. In the proposed framework, the displacement jump between the plies is penalized, and $(1 - d_{\mathrm{coh}})\mathrm{K}^{\mathrm{coh}}$ acts as the penalty parameter. In the case the interface is undamaged and $\mathrm{K}^{\mathrm{coh}} \to \infty$, the Kirchhoff condition is enforced across the whole laminate and transverse shear deformations of the laminate are precluded. In practice, however, $\mathrm{K}^{\mathrm{coh}}$ is never infinite. Its values may be obtained from experiments, and also have upper bounds coming from numerical considerations of accuracy, stability, and conditioning of the resulting equation systems. As a result, for finite values of $\mathrm{K}^{\mathrm{coh}}$, a multi-layer Kirchhoff–Love shell may effectively represent transverse shearing deformations of the overall laminate, which we demonstrate in the following numerical example.

Table 3.3: Simply supported laminated plate. Ply-level material properties.

E_1[GPa]	E_2[GPa]	G_{12}, G_{13}[GPa]	G_{23}[GPa]	ν_{12}
137.9	10.0	6.89	3.72	0.3

We simulate the static response of a laminated plate under a concentrated transverse load, and compare the results of the present multi-layer formulation with the analytical solution derived in the framework of shear-deformable Reissner–Mindlin shell theory. The plate is square with edge

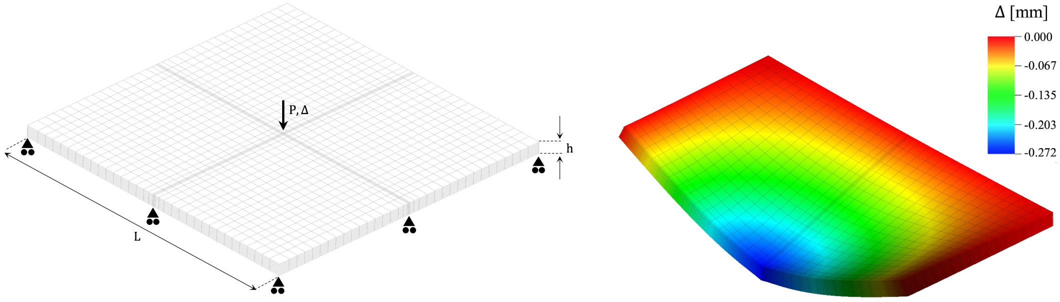

(a) (b)

Figure 3.12: Simply supported laminated plate. (a) Problem setup and mesh; (b) Contours of vertical displacement on the deformed configuration. The displacement is scaled by a factor of 20 and only half of the plate is displayed.

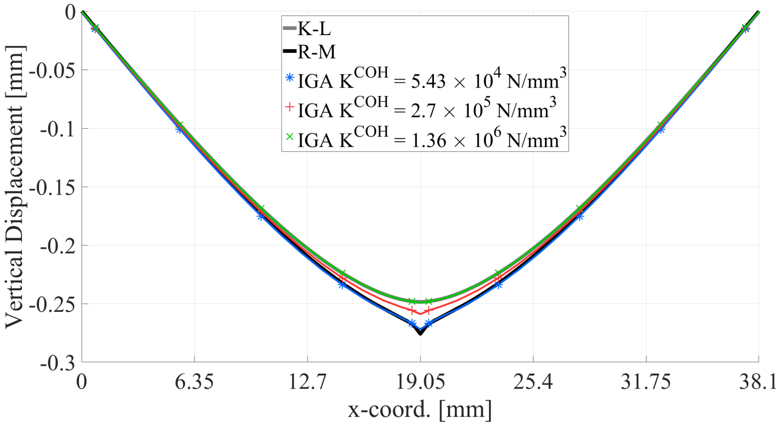

Figure 3.13: Simply supported laminated plate. Midsurface vertical displacement on a line oriented in the direction of the y-axis passing through the plate center. Comparison of the multi-layer formulation with the Kirchhoff–Love (K–L) and with the Reissner–Mindlin (R–M) shear deformable theory solutions.

length of $L = 38.1$ mm and total thickness of $h = 1.524$ mm. The laminate is composed of 12 plies with a symmetric lamination sequence $[0_4/90_2]_s$. Material properties of the individual plies are summarized in Table 3.3.

Problem setup is shown in Figure 3.12(a). Simply supported boundary conditions are enforced on all edges of the bottom ply, and the simulation is carried out by imposing a point force $P = 187.69$ N at the center of the laminate. Since the aim is to assess the ability of the multi-layer construction to represent transverse shear deformation, cohesive interfaces with finite stiffness are defined, but the cohesive interface damage model is not invoked, and the cohesive damage variable d_{coh} is set to zero everywhere during the simulation. The deformed configuration for a 12 layer model is shown in Figure 3.12(b) where the displacements are magnified for illustration purposes.

The analyses are performed by selecting values for the cohesive stiffness in the range

$K^{coh} = 5.43 \times 10^4 - 1.36 \times 10^6$ N/mm^3. We measure the vertical displacement Δ of the plate midsurface on a line oriented in the direction of the y-axis passing through the plate center. Analytical solutions for the Kirchhoff–Love and for the Reissner–Mindlin shell are obtained using the Fourier series approach [90], where the global trigonometric basis functions satisfy the simply-supported boundary conditions on all the plate edges.

Comparisons of the multi-layer, thin-shell, and shear-deformable theory results are shown in Figure 3.13. Larger values of the cohesive stiffness lead to solutions that better satisfy the Kirchhoff constraint, and are closer to the thin-shell theory result. Lowering the cohesive interface stiffness leads to solutions that more and more closely approximate the shear-deformable theory employing shear correction factor of 5/6. In addition, the multi-layer model is also able to capture the highly localized deformation near the applied point load.

3.5.4 Discussion of numerical results

Results of the DCB and ENF tests show excellent correlation with the analytical solutions, derived in the framework of the LEFM, in terms of: (a) The initial elastic response; (b) Initiation of cohesive interface damage; and (c) Propagation of the delamination front. The ability to predict the initial elastic response is particularly relevant for the ENF test because it demonstrates that the bending stiffness of the laminate is recovered by connecting the plies through cohesive interfaces. Additional discussion of the cohesive interface formulation is provided in what follows.

Cohesive interface strength

From the simulation of the DCB and ENF tests it can be inferred that the numerical solutions are affected by the choice of interface strength. On the other hand, the LEFM analytical model [1, 77] is based on the energy released during propagation of delamination, and does not take into account the interface strength. In the numerical simulations, larger values of t_n^0 and of t_τ^0 result in higher peak loads at the delamination point and result in a better match with the theoretical prediction. However, the use of larger interface-strength values translates to a smaller cohesive length (see Equation (3.51)), and thus requires a finer mesh to correctly capture the sharp solution gradients near the delamination front. Turon et al. [104] showed that energy dissipated during delamination under pure Mode I or Mode II opening is independent of the cohesive interface strength. Therefore, in the absence of experimental data, one may specify a lower cohesive strength that meets the element-size requirements without introducing significant energy-dissipation errors [105].

Cohesive interface stiffness

Another parameter introduced in the formulation is the cohesive interface stiffness. In the absence of experimental data, Turon et al. [105] suggest to set $K^{\text{coh}} = \alpha E_3/(h/2)$, where E_3 is the ply out-of-plane Young's modulus and α is a positive constant $\mathcal{O}(10-100)$. In practice, the upper bound of the cohesive stiffness is limited by numerical considerations such as the overall stability of the formulation, conditioning of the resulting equation systems, and stable time-step size for explicit simulations.

Maximum cohesive stiffness also appears to be dependent on the mode in which the cohesive interface fails. For example, in case of the DCB test, the cohesive stiffness is set equal to $K^{\text{coh}} = 5 \times 10^6$ N/mm^3, and the nonlinear solver converges to the required tolerance within a few iterations, even during the propagation of the delamination front. Conversely, it was found that for the ENF test the maximum cohesive stiffness that allows convergence of the nonlinear solver is two orders of magnitude lower than for the DCB test.

In addition, as discussed in the Section 3.5.3, the cohesive interface stiffness affects the extent to which the multi-layered model is able to mimic the behavior of the Reissner–Mindlin shear-deformable theory.

Choosing the cohesive interface stiffness to mimic simple shear

As discussed in Section 3.5.3, the cohesive interface stiffness affects the extent to which the multi-layered model is able to mimic the behavior of the ReissnerMindlin shear-deformable formulation. As such, the cohesive stiffness of the multi-layer model may actually be selected to match the shear deformation behavior of the corresponding continuum solid. For this, we assume that the solid is in the state of simple shear in the through-thickness direction, as shown in Figure 3.14 a. Assuming isotropic, linear-elastic response, the transverse shear strain is uniform, and is given by:

$$\varepsilon_{xz} = \frac{1}{2}\frac{\Delta}{h}\,, \tag{3.52}$$

and the corresponding transverse shear stress by:

$$\tau_{xz} = 2G\varepsilon_{xz} = G\frac{\Delta}{h}\,, \tag{3.53}$$

where G is the shear modulus and h is the thickness. For the multi-layer model, the applied shear stress, in the absence of bending, results in no deformation within the plies and relative displacement of the plies at the cohesive interfaces. (See Figure 3.14 b for an illustration corresponding to a three-layer case). Simple equilibrium at the ply interface leads to the following relationships:

$$\tau_{xz} = \mathrm{K}^{\mathrm{coh}}_{1-2}\left(\Delta_2 - \Delta_1\right)\ , \tag{3.54}$$

and

$$\tau_{xz} = \mathrm{K}^{\mathrm{coh}}_{2-3}\left(\Delta_3 - \Delta_2\right)\ , \tag{3.55}$$

where $\mathrm{K}^{\mathrm{coh}}_{i-j}$ denotes the tangential stiffness of the cohesive interface between the plies i and j, and Δ_i is the horizontal displacement of the i th ply. To ensure that the laminate global deformation follows the continuous case, we introduce the following kinematic compatibility conditions:

$$2\varepsilon_{xz} = \frac{\Delta_2 - \Delta_1}{\frac{h_1}{2} + \frac{h_2}{2}}\ , \tag{3.56}$$

and

$$2\varepsilon_{xz} = \frac{\Delta_3 - \Delta_2}{\frac{h_2}{2} + \frac{h_3}{2}}\ , \tag{3.57}$$

where h_i is the thickness of the i th ply. Equations (3.56) and (3.57) essentially define the equivalent cohesive interface strain as the relative displacement between the ply midsurfaces divided by the distance between them, and equate this strain to its continuum counterpart. Introducing Equations (3.56) and (3.57) into Equations (3.53), and comparing the results with Equation (3.54) and (3.55), leads the following expressions for the cohesive stiffness:

$$\mathrm{K}^{\mathrm{coh}}_{1-2} = \frac{G}{\frac{h_1}{2} + \frac{h_2}{2}}\ , \tag{3.58}$$

and

$$\mathrm{K}^{\mathrm{coh}}_{2-3} = \frac{G}{\frac{h_2}{2} + \frac{h_3}{2}}\ . \tag{3.59}$$

For an arbitrary number of ply interfaces, the cohesive stiffness formula generalizes to:

$$\mathrm{K}^{\mathrm{coh}}_{i-j} = \frac{G}{\frac{h_i}{2} + \frac{h_j}{2}}\ . \tag{3.60}$$

To test the cohesive stiffness definition given by Equation (3.60), we revisit the example of a plate subjected to a point load shown in Fig. 13. This time we assume the plate is made of isotropic material, and represent it by means of two, six and 12 plies of uniform thickness for the multi-layer model. The Youngs modulus is set to E = 68,950 MPa and Poisson's ratio to ν = 0.35, which gives the shear modulus G = 25,536 MPa. The ply thickness and the corresponding values of the cohesive stiffness, computed according to Equation (3.60), are reported for all cases in Table 3.4.

Table 3.4: Value of the cohesive stiffness for the multi-layer models as a function of the ply thickness.

2 Plies		6 Plies		12 Plies	
h^{th} [mm]	K^{coh} [N/mm^3]	h^{th} [mm]	K^{coh} [N/mm^3]	h^{th} [mm]	K^{coh} [N/mm^3]
0.762	3.3512×10^4	0.254	1.0054×10^5	0.127	2.0107×10^5

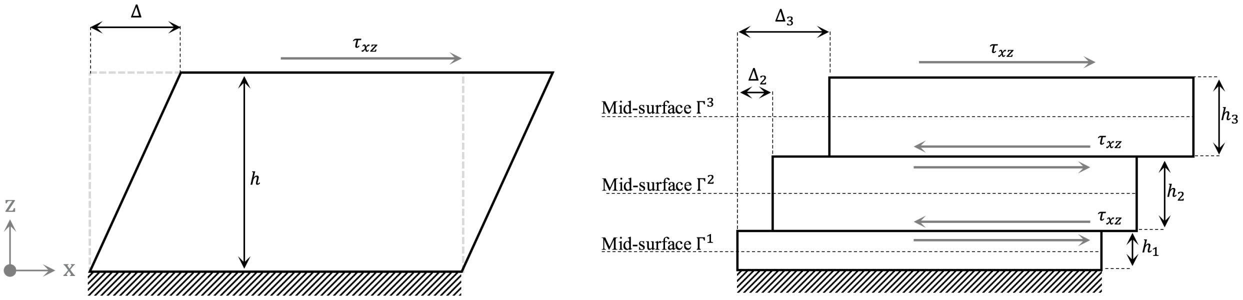

(a) (b)

Figure 3.14: Laminate subjected to a uniform shear stress: (a) continuum solid and (b) multi-layer representation.

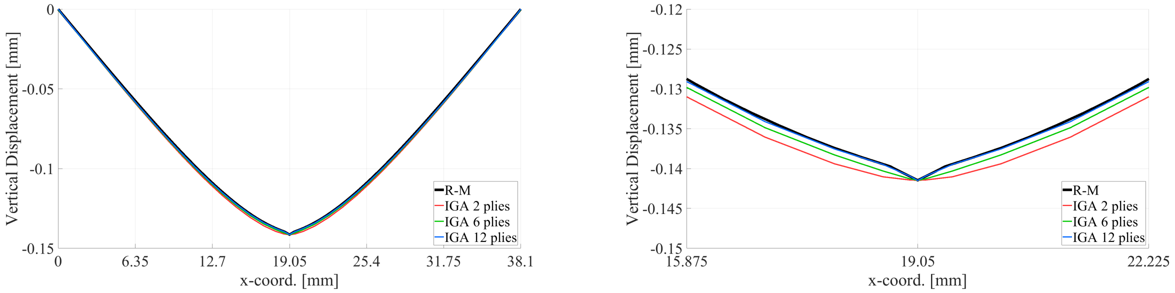

(a) (b)

Figure 3.15: Simply supported laminated plate. Midsurface vertical displacement on a line oriented in the direction of the y-axis passing through the plate center. Comparison of the multi-layer formulation with the Reissner–Mindlin (R–M) shear deformable theory solutions over (a) the entire width of the laminate and (b) in the central section where the load is applied.

The plate mid-surface vertical displacement is shown in Figure 3.15 a, while Figure 3.15 b shows the same results and zooms on the central section where the point load is applied. The plots clearly show that as the number of plies is increased, the solution converges to that predicted by the shear deformable theory.

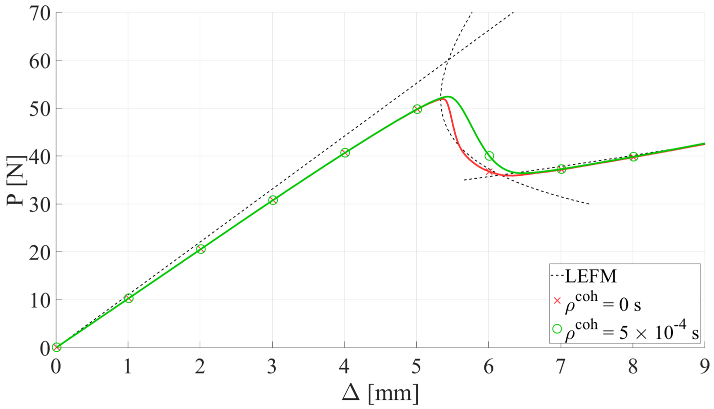

Figure 3.16: ENF test simulation. Load-displacement curves obtained with and without viscous regularization of the damage variable.

Viscous regularization

In this section, the ENF test is used to asses the solution sensitivity to the choice of the cohesive-damage viscous regularization parameter (see Equation (3.45)). We perform a quasi-static simulation of this case with a load step 10^{-3}. We set the viscous regularization parameter to $\rho^{\mathrm{coh}} = 5 \times 10^{-4}$ and compare the results with the non-regularized case. The comparison, reported in Figure 3.16, shows that the peak force obtained with regularization exceeds by 0.9 % the value obtained without regularization. As expected, the initial linear response and stable propagation region are not affected by the regularization. However, regularization delays the initiation of delamination, and gives a smoother transition between the two stable regions in the force-displacement curve. While this smoother transition is favorable from the numerical viewpoint, excessive regularization of the damage variable may lead to underprediction of the extent of delamination during an impact event.

3.6 Acknowledgments

Chapter 3 is, in full, an edited reprint of the material as it appears in:

- *"A new multi-layer approach for progressive damage simulation in composite laminates based on isogeometric analysis and Kirchhoff–Love shells. Part I: basic theory and modeling of delamination and transverse shear"*, published on-line in *"Computational Mechanics"* on November 30th 2017 and co-authored by *Marco S. Pigazzini, Yuri Bazilevs, Andrew C. Ellison, and Hyonny Kim*. This article is currently in press. The author of this dissertation *(Marco S. Pigazzini)* is one of the primary investigators and authors of this paper.
- *"A new multi-layer approach for progressive damage simulation in composite laminates based on isogeometric analysis and Kirchhoff–Love shells. Part II: impact modeling"*, published on-line in *"Computational Mechanics"* on November 24th 2017 and co-authored by *Marco S. Pigazzini,*

Yuri Bazilevs, Andrew C. Ellison, and Hyonny Kim. This article is currently in press. The author of this dissertation *(Marco S. Pigazzini)* is the primary investigator and author of this paper.

This work was supported by NASA Advanced Composites Project No. 15-ACP1-0021. The co-authors of the articles [14, 84] and I thank F. Leone, C, Rose, and C. Davila from NASA Langley Research Center for their valuable comments and suggestions.

4 Isogeometric analysis for progressive damage simulation of composite laminates

This chapter focuses on the application of the multi-layer IGA shell formulation for damage-growth simulations of composite laminates. Three numerical simulations of low velocity impact on composite laminates are presented. These examples aim to represent the broad-spectrum applicability of the multi-layer analysis framework introduced in this dissertation.

In order to perform impact simulations, the formulation developed in Chapter 3, and summarized by Equation (3.46), is augmented with a penalty contact model that is presented in Section 4.1. In Section 4.2 the complete discrete formulation is summarized including intralaminar damage, delamination, contact interface and bending strips. Applications of the multi-layer modeling framework for low velocity impact simulations are presented in Section 4.3. Results of numerical impact simulations and comparison with experimental results are presented in Section 4.4.

4.1 Contact algorithm for shells

The ability of the method to handle contacts between the impactor and laminate, as well as between the lamina or sublaminates, is essential for carrying out simulation of impact on laminated composite structures. In what follows, we describe in detail the contact formulation employed in this work and its algorithmic implementation. The formulation is presented in the context of thin isogeometric shells, however, many of its constituents are applicable to a wider class of solid and structural models.

While several numerical techniques have been developed for contact and impact problems (see, e.g., [107] for a comprehensive review), the penalty formulation is the most commonly adopted methodology, especially for large-scale analyses, because, unlike in the case of Lagrange-multiplier or mortar-type methods [102], no additional unknowns are introduced in the formulation.

The penalty method is based on the introduction of a repulsive traction in order to enforce, albeit approximately, the non-interpenetration condition between the disconnected parts. The contact algorithm presented in this dissertation consists of two separate steps:

1. *Search* step, where pairs of candidate contact points are identified.
2. *Penalization* step, where a signed distance function is evaluated in order to verify if the contact criteria are satisfied.

By definition, a pair of candidate contact points are two material points belonging to two separate parts, or objects, that satisfy a user-defined search criterion. The existence of a pair of candidate contact points is only a necessary condition to determine whether the separate parts are in contact. The actual contact occurs only if the distance between the candidate points is smaller than a specified threshold. If both the search and penalization steps are successful, meaning that a pair of candidate contact points exists and the distance between them is small enough to satisfy the contact criterion, then contact traction is introduced in the multilayer-shell variational formulation. In what follows, we outline our methodology to detect interaction between separate parts represented by shell surfaces in 3D. We note that this two-step procedure is efficient because it allows one to perform the search step, which is computationally demanding, in a configuration of choice, such as, for example, the reference configuration at the beginning of the simulation. Conversely, the penalization step is much less expensive as it only requires evaluation of the distance between all the pairs of candidate contact points, and thus may be performed at every time-integration and/or nonlinear-iteration step.

4.1.1 Search step

A contact interface is defined as the intersection of two distinct surfaces, namely Γ^1 and Γ^2, which, in the framework of our modeling approach, correspond to NURBS surfaces representing two separate geometric entities. The purpose of the search step is to identify, for each point $\mathbf{x}_1 \in \Gamma^1$, the corresponding candidate contact point $\mathbf{x}_2 \in \Gamma^2$ defined according to a specific proximity criterion. From a theoretical standpoint, a pair of candidate contact points is defined as a subset of $\Gamma^1 \cap \Gamma^2$. However, this definition is not appropriate in the framework of shell representations of 3D continuum. Indeed, in order to take the shell thickness into account, it is necessary to detect possible contact *before* the intersection of the surfaces occurs. We therefore introduce a search procedure in order to identify all the possible pairs of candidate contact points on all the surfaces where the contact is activated, while detection of the actual contact is deferred to the penalization step.

In our work, we developed a search algorithm based on the technique proposed in [65]. The search problem is formally defined in terms of finding the points $\mathbf{x}_1\left(\boldsymbol{\xi}_{\mathbf{x}_1}\right)$ and $\mathbf{x}_2\left(\boldsymbol{\xi}_{\mathbf{x}_2}\right)$ that satisfy:

$$\begin{cases} \mathrm{f}_1\left(\boldsymbol{\xi}_{\mathbf{x}_2}\right) = \left(\mathbf{x}_1 - \mathbf{x}_2\left(\boldsymbol{\xi}_{\mathbf{x}_2}\right)\right) \cdot \mathbf{x}_2\left(\boldsymbol{\xi}_{\mathbf{x}_2}\right)_{,\xi_1} & = 0 \quad , \\ \mathrm{f}_2\left(\boldsymbol{\xi}_{\mathbf{x}_2}\right) = \left(\mathbf{x}_1 - \mathbf{x}_2\left(\boldsymbol{\xi}_{\mathbf{x}_2}\right)\right) \cdot \mathbf{x}_2\left(\boldsymbol{\xi}_{\mathbf{x}_2}\right)_{,\xi_2} & = 0 \quad . \end{cases} \tag{4.1}$$

The above nonlinear-equation system represents the condition that the distance vector $\mathbf{x}_1 - \mathbf{x}_2\left(\boldsymbol{\xi}_{\mathbf{x}_2}\right)$ is orthogonal to the tangent plane of Γ^2 defined by the tangent vectors $\mathbf{x}_2\left(\boldsymbol{\xi}_{\mathbf{x}_2}\right)_{,\xi_1}$ and $\mathbf{x}_2\left(\boldsymbol{\xi}_{\mathbf{x}_1}\right)_{,\xi_2}$. Note that $\mathbf{x}_1$ is not explicitly written as a function of $\boldsymbol{\xi}_{\mathbf{x}_1}$ because during the search step the point $\mathbf{x}_1$ is assumed fixed and its parametric coordinates constant.

The Newton–Raphson iterative method is used to solve the nonlinear-equation system for the parametric coordinates $\boldsymbol{\xi}_{\mathbf{x}_2}$, where each iteration takes on the form:

$$\boldsymbol{\xi}_{\mathbf{x}_2}^{i+1} = \boldsymbol{\xi}_{\mathbf{x}_2}^{i} - \left[\mathbf{J}\left(\boldsymbol{\xi}_{\mathbf{x}_2}^{i}\right)\right]^{-1} \begin{bmatrix} \mathrm{f}_1\left(\boldsymbol{\xi}_{\mathbf{x}_2}^{i}\right) \\ \mathrm{f}_2\left(\boldsymbol{\xi}_{\mathbf{x}_2}^{i}\right) \end{bmatrix} \quad , \tag{4.2}$$

where i is the iteration index. The exact Jacobian matrix $\mathbf{J}$ of the Newton–Raphson iteration is given by

$$\mathbf{J}\left(\boldsymbol{\xi}_{\mathbf{x}_2}^{i}\right) = \begin{bmatrix} \mathrm{J}_{11}\left(\boldsymbol{\xi}_{\mathbf{x}_2}^{i}\right) & \mathrm{J}_{12}\left(\boldsymbol{\xi}_{\mathbf{x}_2}^{i}\right) \\ \mathrm{J}_{21}\left(\boldsymbol{\xi}_{\mathbf{x}_2}^{i}\right) & \mathrm{J}_{22}\left(\boldsymbol{\xi}_{\mathbf{x}_2}^{i}\right) \end{bmatrix} \quad , \tag{4.3}$$

where

$$\begin{aligned} \mathrm{J}_{11}\left(\boldsymbol{\xi}_{\mathbf{x}_2}^{i}\right) &= \mathbf{x}_1 \cdot \mathbf{x}_{2,\xi_1\xi_1} - \mathbf{x}_{2,\xi_1} \cdot \mathbf{x}_{2,\xi_1} - \mathbf{x}_2 \cdot \mathbf{x}_{2,\xi_1\xi_1} \ , \\ \mathrm{J}_{12}\left(\boldsymbol{\xi}_{\mathbf{x}_2}^{i}\right) &= \mathbf{x}_1 \cdot \mathbf{x}_{2,\xi_1\xi_2} - \mathbf{x}_{2,\xi_2} \cdot \mathbf{x}_{2,\xi_1} - \mathbf{x}_2 \cdot \mathbf{x}_{2,\xi_1\xi_2} \ , \\ \mathrm{J}_{21}\left(\boldsymbol{\xi}_{\mathbf{x}_2}^{i}\right) &= \mathbf{x}_1 \cdot \mathbf{x}_{2,\xi_2\xi_1} - \mathbf{x}_{2,\xi_1} \cdot \mathbf{x}_{2,\xi_2} - \mathbf{x}_2 \cdot \mathbf{x}_{2,\xi_2\xi_1} \ , \\ \mathrm{J}_{22}\left(\boldsymbol{\xi}_{\mathbf{x}_2}^{i}\right) &= \mathbf{x}_1 \cdot \mathbf{x}_{2,\xi_2\xi_2} - \mathbf{x}_{2,\xi_2} \cdot \mathbf{x}_{2,\xi_2} - \mathbf{x}_2 \cdot \mathbf{x}_{2,\xi_2\xi_2} \ . \end{aligned} \tag{4.4}$$

As pointed out in [13], the IGA representation of contacting surfaces is beneficial for the search procedure because the surfaces are naturally parameterized (in our case, using NURBS functions), and the parameterization is smooth almost everywhere allowing for direct evaluation of the position-vector second derivatives. However, in general, the uniqueness of the nonlinear-system solution is not guaranteed, and it is often necessary to introduce additional constraints on the domain of the unknown solution vector $\boldsymbol{\xi}_{\mathbf{x}_2}$. In practice, these constrains are enforced by reducing the search domain from the whole surface Γ^2 to a smaller sub-domain located in the proximity of the point $\mathbf{x}_1$. Implementation details of the search step are discussed in Section 4.1.4.

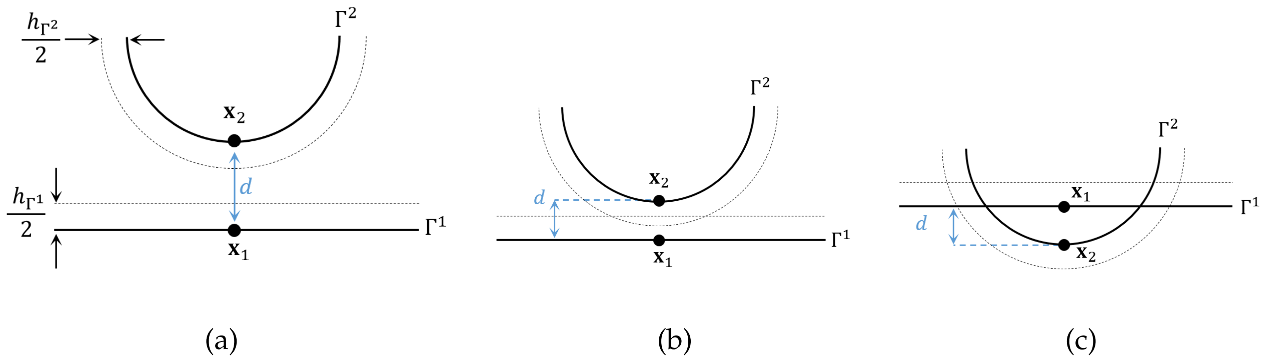

Figure 4.1: Penalty contact formulation: Three stages of the impact. (a) No contact, where $d \leq -h$; (b) Soft contact, where $d \in (-h, 0)$; (c) Hard contact, where $d \geq 0$. Solid black lines represent the shell middle surfaces, while dashed lines represent the actual surface with shell thickness taken into account.

4.1.2 Penalization step

The successful search step finds pairs of points $\mathbf{x}_1$ and $\mathbf{x}_2$ that satisfy the condition given by Equation (4.1). However, these points are not necessarily in contact as they may be too far apart. Contact is thus introduced through a penalization step, where we first introduce the signed distance $d\left(\boldsymbol{\xi}_{\mathbf{x}_1}, \boldsymbol{\xi}_{\mathbf{x}_2}\right)$ defined as:

$$d = \left[\mathbf{x}_2\left(\boldsymbol{\xi}_{\mathbf{x}_2}\right) - \mathbf{x}_1\left(\boldsymbol{\xi}_{\mathbf{x}_1}\right)\right] \cdot \mathbf{n}_2\left(\mathbf{x}_2\left(\boldsymbol{\xi}_{\mathbf{x}_2}\right)\right) \ . \tag{4.5}$$

Since the distance vector $(\mathbf{x}_2 - \mathbf{x}_1)$ is, by definition, parallel to $\mathbf{n}_2$, the value of the distance function is null when the spatial locations $\mathbf{x}_1$ and $\mathbf{x}_2$ coincide in space and the surfaces are in contact at that location. We then define the contact pressure P_k to be a non-linear function of d as:

$$P_k = \begin{cases} 0 & \text{if} \quad d \leq -h \, , \\ \dfrac{k}{2h}\left(d+h\right)^2 & \text{if } d \in (-h, 0) \ , \\ \dfrac{kh}{2} + kd & \text{if } d \geq 0 \, , \end{cases} \tag{4.6}$$

where k is the contact stiffness, while the absolute value of the parameter h determines the distance at which the candidate points are set to be in contact. In our implementation, the parameter h is chosen equal to the sum of the local half-thicknesses of the surfaces Γ^1 and Γ^2 at points $\mathbf{x}_1\left(\boldsymbol{\xi}_{\mathbf{x}_1}\right)$ and $\mathbf{x}_2\left(\boldsymbol{\xi}_{\mathbf{x}_2}\right)$. Note that the contact pressure P_k in Equation (4.6) is designed to be a smooth function of d in order to improve nonlinear convergence.

Using the contact pressure P_k as above, we define the contact traction by multiplying P_k

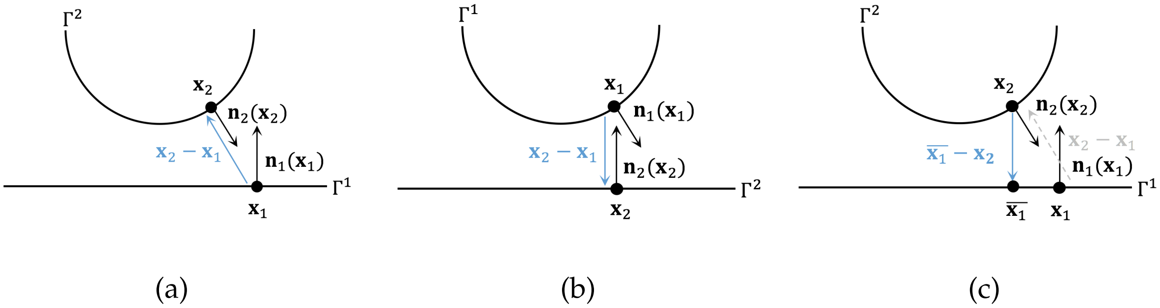

Figure 4.2: Penalty contact formulation: Evaluation of the distance for the penalization step. (a) and (b) Asymmetric definition of the distance vector; (c) Symmetrization procedure.

with the normal vector $\mathbf{n}_2$ as:

$$\mathbf{t}^{\text{con}} = P_k(\mathbf{n}_2)\,\mathbf{n}_2\,, \tag{4.7}$$

and adding the following terms to the variational formulation of the multi-layer shell:

$$+\int_{\Gamma_t^{\text{con}}} (\mathbf{w}_2 - \mathbf{w}_1)\cdot P_k(\mathbf{n}_2)\,\mathbf{n}_2\,\mathrm{d}\Gamma\,. \tag{4.8}$$

Equation (4.8) presents the nonlinear penalty-contact formulation, which weakly enforces the surface non-interpenetration condition. Given the definition of the contact pressure in Equation (4.6), one can identify three stages of impact, namely, no-contact, soft contact, and hard contact. See Figure 4.1 for an illustration and further description.

4.1.3 Symmetrization of the contact formulation

The contact formulation presented in the previous section introduces a dependence of the contact pressure, and, as a result, of the contact traction, on which surface, Γ^1 or Γ^2, is designated as the contact surface. The difference in the contact traction arises from the difference in the orientation of the normal vector on the two contacting surfaces. Consider, for example, the case of a curved and flat surface in contact, as shown in Figures 4.2(a) and 4.2(b). The signed distance function computed with the curved surface designated as Γ^2 is clearly different from that computed by designating the flat surface as Γ^2.

To minimize this dependence, we “symmetrize” the contact formulation by introducing a two-step search procedure illustrated in Figure 4.2(c) and summarized in what follows.

1. Consider point $\mathbf{x}_1$ on Γ^1:
    (a) Do a search step, keeping $\mathbf{x}_1$ fixed, to find $\mathbf{x}_2$ on Γ^2;

   (b) Compute the contact pressure $P_k(\mathbf{n}_2(\mathbf{x}_2))$ based on the distance function $d = (\mathbf{x}_2 - \mathbf{x}_1) \cdot \mathbf{n}_2(\mathbf{x}_2)$.

2. Consider point $\mathbf{x}_2$ on Γ^2 found in Step 1 above.

   (a) Do a search step, keeping $\mathbf{x}_2$ fixed, to find $\bar{\mathbf{x}}_1$ on Γ^1;

   (b) Compute the contact pressure $\bar{P}_k(\mathbf{n}_1(\bar{\mathbf{x}}_1))$ based on the distance $\bar{d} = (\bar{\mathbf{x}}_1 - \mathbf{x}_2) \cdot \mathbf{n}_1(\bar{\mathbf{x}}_1)$.

3. Compute the final contact pressure by averaging P_k and $\bar{P}_k$.

This symmetrization procedure provides significant advantages over the unsymmetrized case if the difference in the orientation of the normal vectors on the contacting surfaces is large.

Remark. In the last step of the symmetrization procedure it is also possible to average the contract traction vector directly. However, this option was not pursued in this work.

4.1.4 Increasing the efficiency of the search step

In order to increase the efficiency of the search step, we devised a two-level reduction of the search domain for a given pair of contact surfaces. The first step involves defining a *search box*: all the elements that are not included in a user-defined box region in 3D space are automatically excluded from the search domain. The second step involves defining a *search list*: for each element included in the search box, we create a list that includes only the elements that are closer to it than a specified threshold. The actual search step, which involves solution of the nonlinear system given by Equation (4.1), is therefore performed only for the elements included in the search list.

A rigorous application of the contact algorithm requires one to perform a full search and penalization at each time step and at every iteration of the nonlinear solver in order to accurately account for the interaction between the contacting surfaces. However, in some situations, this requirement may be relaxed. For example, if the parts in contact are not subjected to large relative displacements during the deformation, search for the candidate contact points can be performed only once in the structure reference configuration. However, even if the search step is performed only once in the reference configuration, the penalization step must be performed continuously during the analysis to allow the surfaces to come in and out of contact as dictated by the governing equations.

4.2 Extended discrete formulation

For the purposes of impact simulation, we consider a laminated composite structure comprised of *Np* plies or sublaminates and *Nc* cohesive interfaces. In addition, we assume the structure also contains *Ncon* contact interfaces and *Nbs* bending strips. The complete semi-discrete variational formulation may be stated as follows: Find the configuration $\mathbf{x}^h \in S_{\mathrm{x}}^h$, such that, $\forall \mathbf{w}^h \in S_{\mathrm{w}}^h$,

$$
\begin{aligned}
\sum_{ip=1}^{N\mathrm{p}} \quad & \Bigg\{ \int_{\left(\Gamma_0^S\right)_{ip}} \mathbf{w}^h \cdot \rho_{0_{ip}} h_{th_{ip}} \left(\frac{d^2 \mathbf{x}^h}{dt^2} - \mathbf{f}^h \right) \mathrm{d}\Gamma \\
& + \int_{\left(\Gamma_0^S\right)_{ip}} \delta \overline{\boldsymbol{\varepsilon}}^h \cdot \left(\mathbf{K}_{ip}^{\mathrm{exte}} \left(\boldsymbol{d}_{\mathrm{var}_{ip}} \right) \overline{\boldsymbol{\varepsilon}}^h + \mathbf{K}_{ip}^{\mathrm{coup}} \left(\boldsymbol{d}_{\mathrm{var}_{ip}} \right) \overline{\boldsymbol{\kappa}}^h \right) \mathrm{d}\Gamma \\
& + \int_{\left(\Gamma_0^S\right)_{ip}} \delta \overline{\boldsymbol{\kappa}}^h \cdot \left(\mathbf{K}_{ip}^{\mathrm{coup}} \left(\boldsymbol{d}_{\mathrm{var}_{ip}} \right) \overline{\boldsymbol{\varepsilon}}^h + \mathbf{K}_{ip}^{\mathrm{bend}} \left(\boldsymbol{d}_{\mathrm{var}_{ip}} \right) \overline{\boldsymbol{\kappa}}^h \right) \mathrm{d}\Gamma \\
& - \int_{\left(\Gamma_t^S\right)_h} \mathbf{w}^h \cdot \mathbf{h}^h \, \mathrm{d}\Gamma \Bigg\} \\
+ \sum_{ic=1}^{Nc} \quad & \Bigg\{ \int_{\left(\Gamma_t^{\mathrm{coh}}\right)_{ic}} \left[\left(\mathbf{w}_{1_{ic}}^h + \frac{h_{\Gamma^{1_{ic}}}}{2} \delta \mathbf{n}_{1_{ic}}^h \right) - \left(\mathbf{w}_{2_{ic}}^h + \frac{h_{\Gamma^{2_{ic}}}}{2} \delta \mathbf{n}_{2_{ic}}^h \right) \right] \cdot \mathbf{t}^{\mathrm{coh}} \, \mathrm{d}\Gamma \Bigg\} \\
+ \sum_{ic=1}^{Ncon} \quad & \Bigg\{ \int_{\left(\Gamma_t^{\mathrm{cont}}\right)_{ic}} \left(\mathbf{w}_{2_{ic}}^h - \mathbf{w}_{1_{ic}}^h \right) \cdot \mathbf{t}^{\mathrm{con}} \, \mathrm{d}\Gamma \Bigg\} \\
+ \sum_{ibs=1}^{N\mathrm{bs}} \quad & \Bigg\{ \int_{\left(\Gamma_t^{\mathrm{bs}}\right)_{ibs}} \delta \overline{\boldsymbol{\kappa}}^h \cdot \mathbf{K}_{ibs}^{\mathrm{bend}} \overline{\boldsymbol{\kappa}}^h \, \mathrm{d}\Gamma \Bigg\} \\
- \int_{\left(\Gamma_0^S\right)_{es}} & \mathbf{w}^h \cdot \mathbf{K}^{\mathrm{es}} \left(\mathbf{x}^h - \mathbf{X}^h \right) \mathrm{d}\Gamma = 0 \, ,
\end{aligned}
\tag{4.9}
$$

where $\mathbf{K}_{ibs}^{\mathrm{bend}}$ is the stiffness matrix associated with the *ibs-th* bending strip. A detailed description of the bending strip method is reported in the work of Kiendl et al. [67]. As discussed in Chapter 3, the trial and test function sets are comprised of NURBS basis functions that are defined on each ply, and are discontinuous from ply to ply. In the cohesive-interface terms of the above formulation the subscripts 1_{ic} and 2_{ic} are consistent with the notation introduced in Chapter 3 of this dissertation, while the subscripts 1_{ic} and 2_{ic} in the contact terms are consistent with the notation in Section 4.1. Intralaminar damage is implicitly embedded in the definition of the extensional, coupling, and bending stiffness matrices of each ply, and automatically accounts for their current damage state. Both the implicit and explicit versions of the Generalized-α method [31] are employed to integrate the semi-discrete Equations (4.9) in time.

Remark In the above formulation, the last term on the left hand side represents the elastic-support boundary conditions. The boundary conditions are defined on a subregion $\left(\Gamma_0^S\right)_{es}$ in the reference configuration. The matrix $\mathbf{K}^{\mathrm{es}}$ is diagonal and may be expressed as:

$$\mathbf{K}^{\mathrm{es}} = \begin{bmatrix} \mathrm{K}_x^{\mathrm{es}} & 0 & 0 \\ 0 & \mathrm{K}_y^{\mathrm{es}} & 0 \\ 0 & 0 & \mathrm{K}_z^{\mathrm{es}} \end{bmatrix} , \tag{4.10}$$

where $\mathrm{K}_x^{\mathrm{es}}$, $\mathrm{K}_y^{\mathrm{es}}$ and $\mathrm{K}_z^{\mathrm{es}}$ are the directional stiffness coefficients expressed in the global coordinate system. Although the elastic-support boundary conditions are not employed in the computations presented in the next section, they may be quite useful for representing the effect of frame-like supports employed in many impact tests.

4.2.1 Numerical integration of constitutive equations

As discussed in Chapter 3.4, the Generalized–α method is used for the numerical solution of the variational form (4.9). The nonlinear set of equation is solved using the Newton–Raphson method which, for every nonlinear iteration, involves solution of the following system of linear equations:

$$\left(\mathbf{M}\alpha_m + \mathbf{C}\alpha_f\gamma\Delta t + \mathbf{K}\alpha_f\beta\Delta t^2\right)\Delta\ddot{\mathbf{d}}_{n+1} = -\mathbf{R}_{n+1}^i \, . \tag{4.11}$$

Impact simulations presented in this Chapter, however, often require small time steps to accurately capture the underlying fast dynamics. For this reason, an explicit version of the Generalized-α scheme may be introduced where the tangent matrix given by Equation (3.50) is simplified to only contain the mass terms, without changing the rest of the Generalized-α algorithm. In this case, the nonlinear iteration is reduced to

$$\alpha_m\mathbf{M}\Delta\ddot{\mathbf{d}}_{n+1} = -\mathbf{R}_{n+1}^i \, . \tag{4.12}$$

In addition, the consistent mass matrix $\mathbf{M}$ may be replaced with its "lumped" counterpart using the row-sum technique [57]. Unlike in the case of Lagrange polynomials, because the NURBS basis functions are pointwise non-negative, the row-sum procedure results in a lumped mass matrix with all positive entries for NURBS of any order. For recent advances in explicit time integration using IGA see [6].

4.3 Impact simulations

In this section, impact test on composite laminates are simulated in order to validate the modeling procedures through comparison with experimental data and simulations of this test reported in the literature.

The first set of numerical examples involves low-velocity impact on flat composite plates. In the first example, labeled *Model 1*, a 16-plies composite flat laminate is modeled ply-by-ply and ply grouping is employed to increase the computational efficiency. For this test, in-house FE-based Abaqus/Explicit [59] simulations using 3D linear solid elements are also carried out for comparison. Results of IGA and in-house FE model are compared with results reported in the literature. In the second example, labeled *Model 2*, a 24-plies composite flat laminate is modeled ply-by-ply. In order to obtain a high-fidelity representation of the damage state at the lamina level, no ply grouping is employed. Numerical results are validated through a comparison with experimental data.

A third numerical example, labeled *Model 3*, aims to predict damage growth in a stringer-stiffened composite panel subjected to an accidental impact. Isogeometric analysis is beneficial for the representation of curved geometries, such as the composite stringer considered in this example. By providing an exact representation of all conics, the IGA approach allows for more accurate modeling of curved boundaries using coarser discretizations than more traditional low-order FEM approximations.

All the IGA-based computations are carried out using an in-house research software that implements all the methods presented in this dissertation. C^1-continuous quadratic NURBS are employed for all the IGA-based simulations presented in this section.

4.3.1 Experimental setup

Model 1: 16-plies flat laminate

Experimental setup of the impact test is shown in Figure 4.3(a). The coupon measures 150 mm × 100 mm and is supported by a rigid frame with a rectangular open window at its center. The size of the unsupported test region is 125 mm × 75 mm. The plate is 4.16 mm thick and is composed of 16 unidirectional carbon/epoxy plies stacked using a symmetric lamination sequence $[0_2, 45_2, 90_2, -45_2]_s$. The impactor head is stiff and spherical, with a diameter of 16 mm and total mass of 2 kg.

Two cases with different impact-energy levels are considered, 6.5 J and 25 J, with experimental investigations reported in [93] and [50], respectively. The experimental results in these references are commonly used for the purposes of model validation (see, e.g., [101]). For the lower energy case, the composite plate is made of T700/M21 material, while for the higher energy case the material employed is T700GC/M21. The lamina material properties employed in the simulations are summarized in Table 4.1.

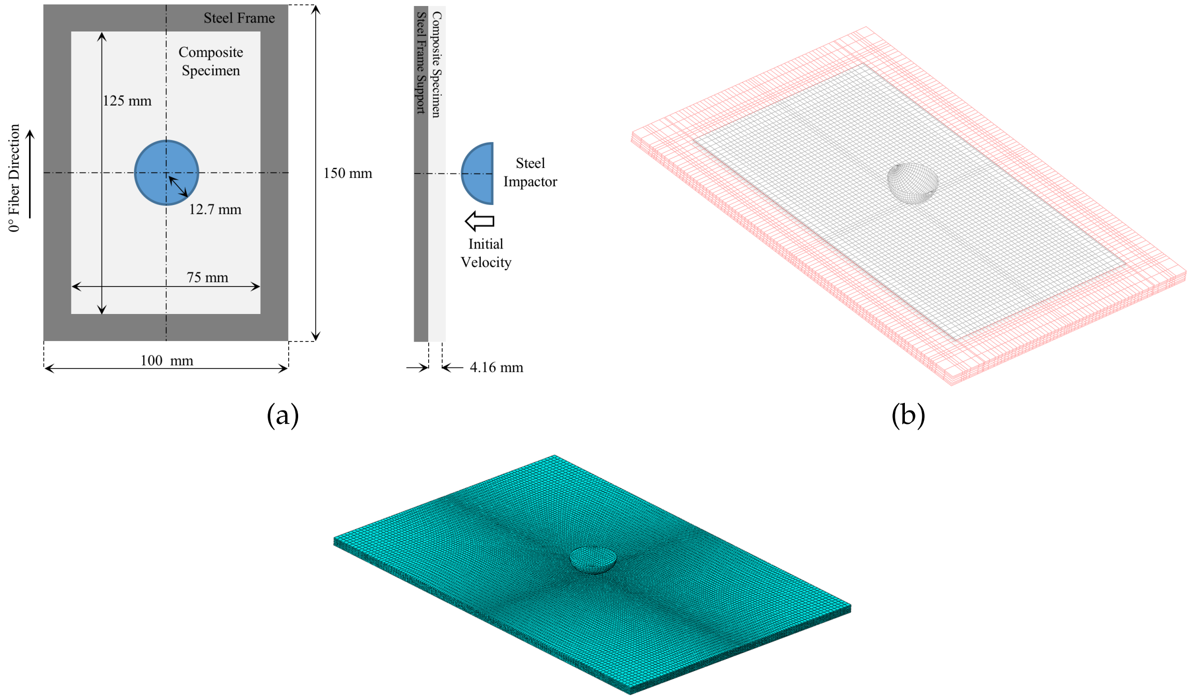

(a) (b)

(c)

Figure 4.3: Impact on a 16-plies flat panel. (a) Experimental setup, (b) IGA model and mesh and (c) In-house FE model. Clamped boundary conditions are imposed on the elements highlighted in red in (b).

Model 2: 24-plies flat laminate

The experimental setup for low-velocity vertical impact on a flat panel is shown in Figure 4.4(a). The composite laminate, which measures 152.4 mm × 101.6 mm, is clamped by steel plates on all the edges. The constraining frame has a rectangular open window at its center that measures 127 mm × 76.2 mm. The plate is 4.809 mm thick and it is made of 24 unidirectional T800/3900-2 carbon/epoxy plies. Material properties used for the analysis are summarized in Table 4.1. The lamination sequence is $[0/45/90/-45]_{3s}$. The impactor has a hemispherical head with a radius of 25.4 mm. The total impacting mass is 5.605 kg, and the initial kinetic energy is 25.1 J.

Model 3: Stiffened panel

The third example involves the simulation of a low-velocity impact on a reinforced aerospace panel. The simulation considers a scenario of an accidental impact that occurs at the center of a stringer flange on the external side of the structure.

The panel, shown in Figure 4.5, measures 990.6 mm in the longitudinal direction of the stringers and 1308.1 mm in the lateral direction. The stringer cross-section is shown in Figure 4.6,

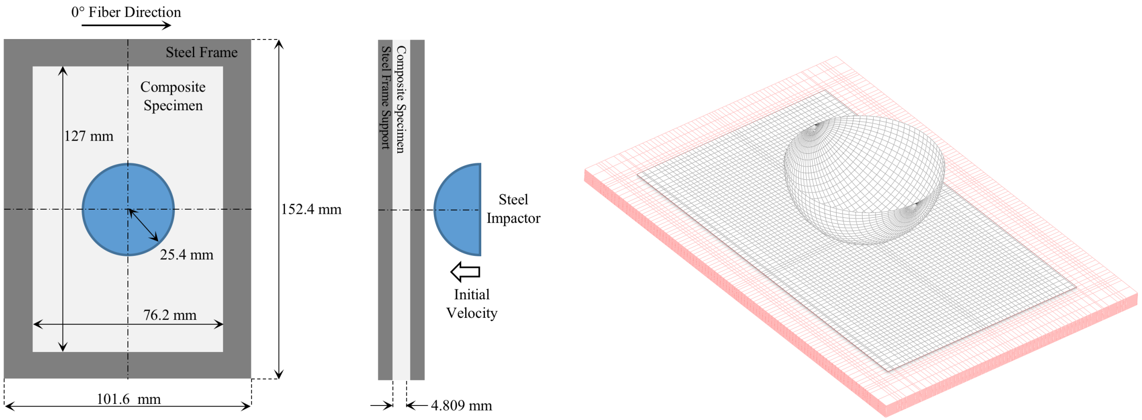

(a) (b)

Figure 4.4: Impact on a 24-plies flat panel. (a) Experimental setup and (b) IGA model and mesh. Clamped boundary conditions are imposed on the elements highlighted in red.

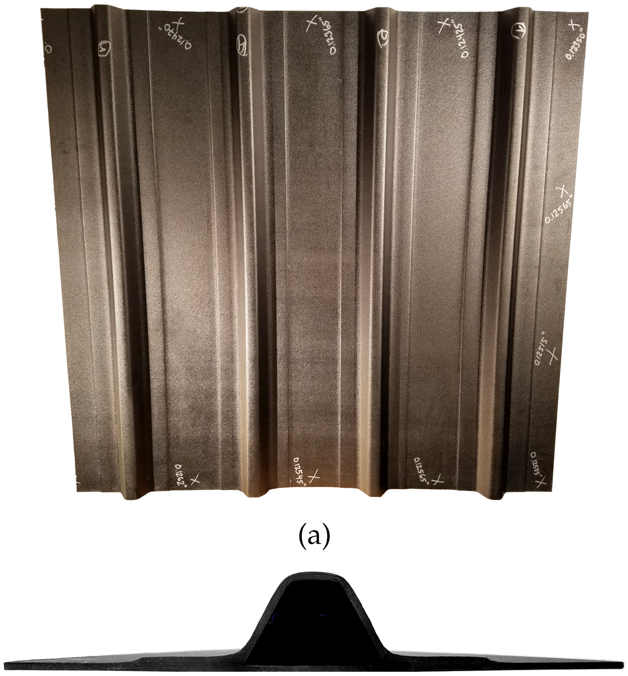

(a)

(b)

Figure 4.5: Stiffened composite panel: (a) Top view of the manufactured five-stringers panel and (b) Detailed cross-section view of a single stiffener.

while the distance between the stringer centerlines is 260.35 mm. The impactor has a hemispherical head with a radius of 12.7 mm. The total impacting mass is 2 kg and the initial kinetic energy is 16 J.

The skin and stringers have an average thickness of 3.2 mm, and are made of 16 unidirec-

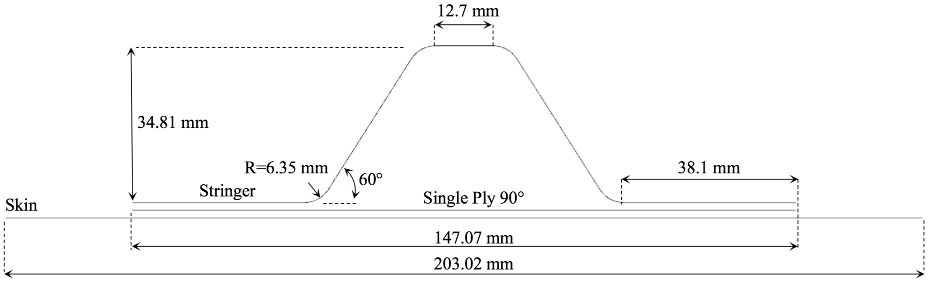

Figure 4.6: Schematic cross-section view of the hat-shaped stringer with dimensions.

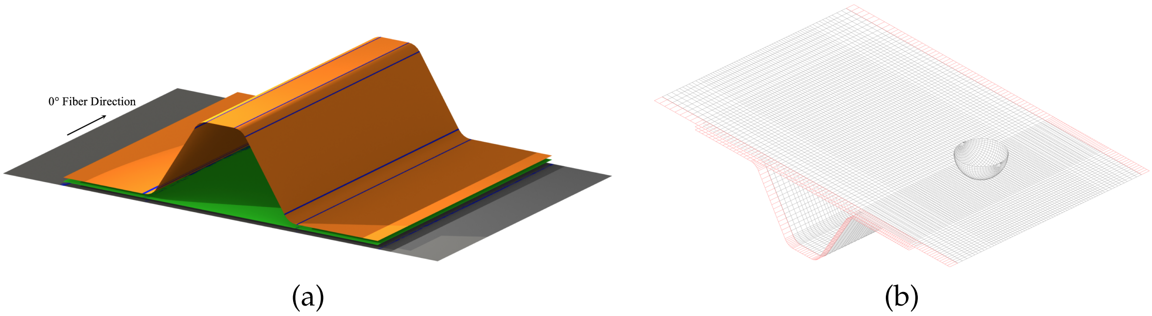

(a) (b)

Figure 4.7: Stiffened composite panel: (a) CAD model and (b) IGA model and mesh. Blue thin surfaces in (a) represent bending strips. Clamped boundary conditions are imposed on the elements highlighted in red in (b).

tional T800/3900-2 carbon/epoxy plies. Material properties used for the analysis are summarized in Table 4.1. The lamination sequence is $[45/\text{-}45/0/45/90/\text{-}45/0/90]_s$. Additional single plies, oriented at 90°, are placed between the skin and each stringer. These extend for the entire length of the panel in the longitudinal direction of the stringers, while in the lateral direction they span the width of the stringer flanges.

4.3.2 Computational setup for IGA-based simulations

Model 1: 16-plies flat laminate

An illustration of the IGA-based multi-layer shell approach for the laminated-plate impact test is shown in Figure 4.8. The lamina material properties employed in the simulations are reported in Table 4.1. The impactor is modeled as a hemispherical shell made from isotropic, stiff material to minimize compliance, with uniform thickness of 1.5 mm and density chosen to match the total mass of the experimental impactor. Zero normal displacement and tangential traction boundary conditions are employed on the plate subdomain supported by the rigid frame.

As proposed in [10], and discussed in Chapter 3 of this dissertation, a characteristic length L_c

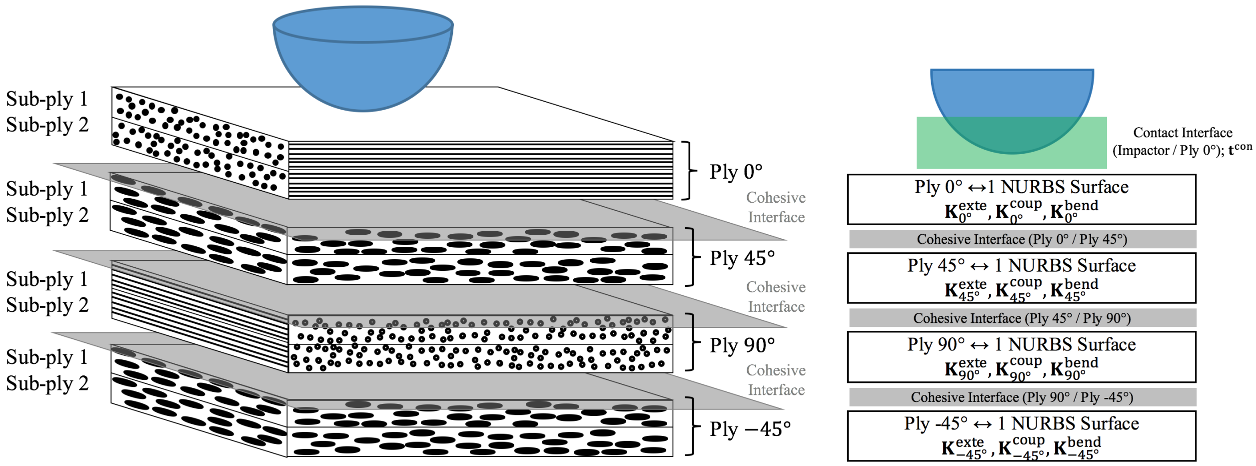

Figure 4.8: Schematic representation of the multi-layer shell model for the impact test. Each ply is represented by a flat surface discretized with C^1-continuous quadratic NURBS. The extensional, coupling and bending stiffnesses depend on the current damage state, and are computed according to the procedures introduced in Chapter 3 of this dissertation. Only half of the laminate is shown for clarity.

Table 4.1: Lamina material properties used in the simulations for the T700/M21 material [93], the T700GC/M21 material [50] and for the T800/3900-2 material.

	Material		
Value	T700/M21	T700GC/M21	T800/3900-2
ρ [kg/m^3]	1,600		1,550
E_1 [GPa]	130		159.9
$E_2 = E_3$ [GPa]	7.7		8.96
$G_{12} = G_{13}$ [GPa]	4.8		6.205
G_{23} [GPa]	3.8		n.a.
$\nu_{12} = \nu_{13}$	0.3	0.33	0.27
ν_{23}	0.35		n.a.
X_T [MPa]	2,080		2,840
X_C [MPa]	1,250		1,551
Y_T [MPa]	60		55.2
Y_C [MPa]	290		165.5
Z_L [MPa]	110		88.2
G_{X_T} [N/mm]	133		179.7
G_{X_C} [N/mm]	10	40	179.7
G_{Y_T} [N/mm]	0.5	0.6	0.419
G_{Y_C} [N/mm]	1.6	2.1	1.187

is introduced in the intralaminar damage model in order to ensure that the strain energy dissipated during the damage process is independent of the discretization adopted for analysis. As before, we define $L_c = \sqrt{A_{\text{ele}}}$, where A_{ele} is the surface area the shell element. The baseline mesh size employed

Table 4.2: Cohesive-interface properties used in the simulations for the (a) T700/M21 material [93] and for the (b) T700GC/M21 and T800/3900-2 materials [50].

$\mathrm{K^{coh}}$ [N/mm^3]	$\mathrm{t_n^0}$ [N/mm^2]	$\mathrm{t_\tau^0}$ [N/mm^2]	$G_{\mathrm{C_n}}$ [N/mm]	$G_{\mathrm{C_\tau}}$ [N/mm]	η
$1 \times 10^{4\ a,b}$	$20.0^{a,b}$	$36.0^{a,b}$	0.5^a,0.6^b	1.6^a,2.1^b	$1.45^{a,b}$

for the IGA-based simulations is 1 mm near the impact location, and gradually increases to 1.5 mm outside the impact zone. The baseline IGA model is shown in Figure 4.3(b). A coarser discretization is also employed for the IGA-based 6.5 J impact-energy simulation in order to investigate the effect of the mesh size. The mesh size of the coarser isogeometric discretization is 1 mm near the impact location and gradually increases to 2.8 mm outside the area where damage is expected to occur. The distribution of L_c in the problem domain is consistent with that of the mesh size.

The cohesive-interface properties employed in the simulations are taken from [101] and reported in Table 4.2. A detailed discussion about the selection of the cohesive-interface stiffness may be found in [105]. As shown in Chapter 3, a more compliant interface gives rise to more pronounced transverse-shear-induced localized deformations, which are inherently neglected in the pure Kirchhoff–Love shell theory. For IGA-based simulations we selected a cohesive-interface stiffness of $\mathrm{K^{coh}} = 10^4$ N/mm^3.

Cohesive-interface formulations, as a rule, require finer mesh resolution in order to correctly describe the delamination-front propagation. According to [105], three-to-ten elements are needed in the cohesive process zone, which is defined as the region between the crack tip and the point where cohesive traction reaches its maximum value. Several models [42, 111, 112, 45, 105, 108] were proposed for the estimation of the process-zone length l^{coh}. Here we make use of the following expressions for the normal and in-plane opening modes:

$$
\begin{aligned}
l_{\mathrm{n}}^{\mathrm{coh}} &= \mathrm{M}E'_{\mathrm{n}}\frac{\mathrm{G_{C_n}}}{\left(\mathrm{t_n^0}\right)^2}\,, \\
l_{\tau}^{\mathrm{coh}} &= \mathrm{M}E'_{\tau}\frac{\mathrm{G_{C_\tau}}}{\left(\mathrm{t_\tau^0}\right)^2}\,,
\end{aligned}
\tag{4.13}
$$

where E' is the equivalent elastic modulus and M is a parameter that depends the model adopted for the cohesive interface. Following [42], we chose $\mathrm{M} = 9\pi/32$ in the simulations.

The equivalent elastic modulus for an orthotropic material E' can conservatively be set equal to the elastic modulus in the transverse direction E_3, as suggested in [105]. Other authors [111, 45] proposed a definition of the the equivalent elastic modulus for an orthotropic material to be a function of the fiber-direction elastic modulus E_1, the transverse modulus E_3, the shear modulus G_{31}, and loading conditions. The equivalent elastic modulus is computed [112] under the hypothesis of the plane-stress state in an unbounded medium. For Mode I opening E'_{n} is computed as:

$$\frac{1}{E'_{\mathrm{n}}} = \sqrt{\frac{1}{2E_1E_2}}\sqrt{\sqrt{\frac{E_1}{E_3}} + \frac{E_1}{2}\left(-\frac{2\nu_{31}}{E_3} + \frac{1}{G_{13}}\right)}\,, \tag{4.14}$$

while for Mode II opening E'_{τ} is computed as:

$$\frac{1}{E'_{\tau}} = \sqrt{\frac{1}{2E_1}}\sqrt{\sqrt{\frac{1}{E_1E_3}} + \left(-\frac{\nu_{31}}{E_3} + \frac{1}{2G_{13}}\right)}\,. \tag{4.15}$$

We note that for isotropic materials the equivalent elastic modulus E' obtained from either expression reduces to the classical elastic modulus E.

Substituting the values of E' given by Equations (4.14) and (4.15) computed for both T700/M21 and T700GC/M21 materials into Equations (4.13), gives $l_{\mathrm{n}}^{\mathrm{coh}} = 11.86$ mm, whereas a more conservative definition from [105] gives $l^{\mathrm{coh}} = 8.4$ mm. As a result, NURBS meshes created for the impact simulations allow at least five (quadratic!) elements to resolve the cohesive process zone.

Ply grouping is adopted for the simulations in order to reduce the computational effort. This simplification is based on the assumption that delamination is triggered mainly due to transverse shear at the interface between the plies with *different* fiber orientations. We note that while delamination between the sub-plies of a single ply group is neglected, the intralaminar damage variables are still evaluated at the level of each ply in the group. This different treatment of interlaminar and intralaminar damage allows us to improve the simulation efficiency without degrading the solution accuracy.

An implicit version of the Generalized-α algorithm is employed with a time step of 2.5 μs (10 μs) for the 25 J (6.5 J) impact case to integrate the governing equations in time. Viscous regularization discussed in Chapter 3 of this dissertation is employed for both intralaminar and interlaminar damage variables. Viscous regularization parameters are set to 10^{-7} s (3×10^{-7} s) for the 25 J (6.5 J) impact case for both intralaminar and interlaminar damage variables.

Model 2: 24-plies flat laminate

For the 24-plies multi-layer model no ply grouping is employed, resulting in a computational model comprised of 24 rectangular NURBS surfaces connected with 23 cohesive interfaces, whose properties are summarized in Table 4.2. The baseline IGA model is shown in Figure 4.4(b). Clamped boundary conditions are only imposed on the top and bottom plies. The impacting device is represented as a hemispherical surface and it is modeled as a stiff isotropic material. A contact interface is defined between the top ply and the impactor.

As discussed in Section 4.3.2, we introduce a reference length in the damage model. The length scale L_c is defined equal to the square root of the element surface area $\sqrt{A_{\text{ele}}}$. The mesh size in the center of the coupon is 1 mm and it gradually increases to 1.5 mm closer to the clamped region. According to Eq. (4.13), the critical cohesive length for the selected material is 17.3 mm. Therefore, the process-zone discretization adopted for IGA guarantees at least ten quadratic elements anywhere in the domain.

Model 3: Stiffened panel

For this example, in order to improve the computational efficiency, we adopt a ply grouping technique. In addition, we perform analysis on a subregion of the entire panel that is 127 mm long, 203.2 mm wide, and includes only one stringer. The model is comprised of 31 NURBS patches that are employed as follows:

- 9 structural patches to represent the stringer;
- 8 bending strips to connect the stringer patches;
- 5 structural patches to represent the skin;
- 4 bending strips to connect the skin patches;
- 3 structural patches to represent the single 90° ply;
- 2 bending strips to connect the patches of the 90° ply.

Clamped boundary conditions are applied on the long edges of the coupon, while the short edges are stress-free. The impacting device is represented as a hemispherical surface and it is modeled as a stiff isotropic material. A contact interface is defined between the skin and the impactor. Five cohesive interfaces, whose properties are summarized in Table 4.2, are employed to connect the skin, the 90° ply and the stringer flanges. Conforming meshes are used for the stringer flange, the 90° ply and the skin. The mesh size L_c is 1.08 mm in the impact region, while it gradually increases toward the clamped edges. The mesh size on the non-impacted flange is 4.18 mm. The discretization satisfies the restrictions imposed by the critical cohesive length computed according to Eq. (4.13).

4.4 Results and discussion of impact simulations

4.4.1 Results and discussion: 16-plies flat laminate

The IGA-based model is validated through the correlation of the impact-force time history with the experimental data available in the literature. In addition, we compare the IGA predictions with the results obtained using an in-house FE model as well as an FE model from [101]. We refer to the latter as the reference FE model.

The in-house FE model, shown in Figure 4.3(c), is an Abaqus/Explicit model comprised of linear brick elements (C3D8R). The in-plane mesh has elements of size 0.5 mm near the impact location, and the element size is gradually increased to 1.5 mm away from the impact zone. Ply grouping is employed with one layer of elements per group. The impactor is modeled as a hemisphere of solid elements with steel elastic properties and mass scaled to 2 kg. Impactor-to-laminate contact is modeled as hard contact with the impactor surface as the master. The NASA CompDam subroutine [95, 63] is employed to model intralaminar damage. Delamination is modeled using the Abaqus built-in cohesive-interface formulation that implements a mixed-mode bilinear softening law. After delamination, ply-to-ply interactions are modeled via contact with friction.

The reference FE model is similar to its in-house counterpart, however, in contrast to the IGA-based and in-house FE models, it also employs a non-symmetric tension-compression material constitutive law and a model for matrix plasticity. (See [101] for details.)

The baseline discretization for the IGA-based simulations has 128,244 DOFs. This number is reduced to only 62,766 DOFs for the coarser IGA-based simulation of the 6.5 J impact case. In contrast, the in-house FE discretization makes use of 772,176 DOFs.

The impact force time histories for the 6.5 J and 25 J impact energy cases are reported in Figures 4.9(a) and 4.9(b), respectively. The results obtained for the 6.5 J impact exhibit a good correlation with the experimental test in terms of the maximum impact force. The IGA and in-house FE models overpredict the peak value by 6% and 9.7%, respectively. In addition, all numerical simulations show an excellent agreement with the experimental data for impact duration. No significant differences are found between the IGA simulation results for two different mesh discretizations (see Figure 4.9(a)), suggesting the baseline IGA mesh is sufficiently fine for the prediction of the impact force.

The numerical results obtained for the 25 J impact case show a little more discrepancy compared to the experimental data and to the reference FE model. The maximum impact force predicted by the IGA-based simulation is 4% larger compared to the in-house FE model, while no significant differences are found in terms of the impact duration. The IGA model overpredicts the

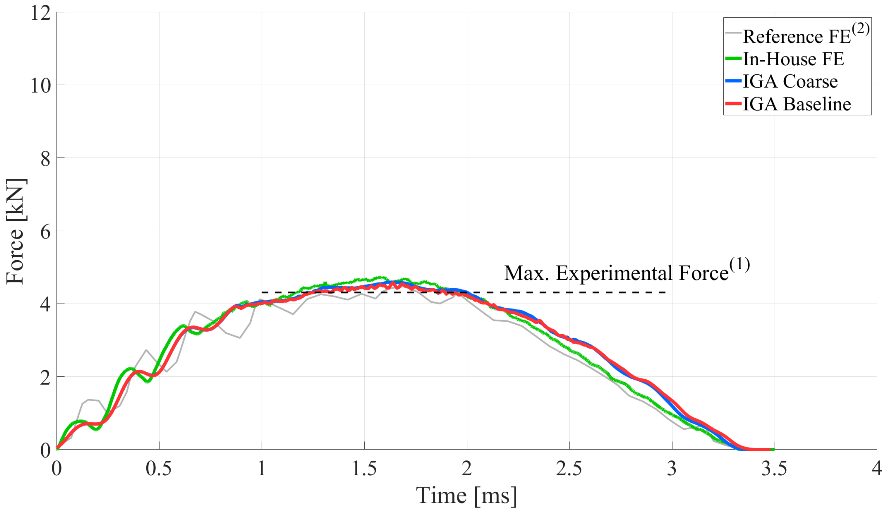

(a)

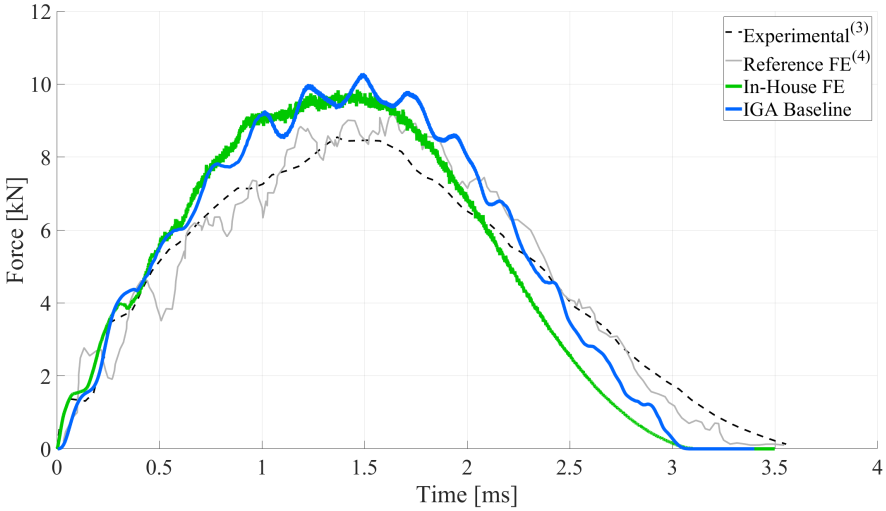

(b)

Figure 4.9: Impact on a 16-plies flat laminate. Impact force time history obtained for the (a) 6.5 J and (b) 25 J impact energy cases. Experimental data labeled (1) and (3) are reported, respectively, in [93] and [50]. Reference numerical results labeled (2) and (4) are reported in [101].

peak force by 11.5% relative to the reference FE model and by 20.1% compared to the experimental data. The predicted duration of the impact event is 0.5 ms shorter compared to the experimental value. However, in the reference FE model, the authors adopted a non-symmetric constitutive law for the unidirectional composite, where the compressive elastic modulus is 23% smaller than the corresponding tensile value of 130 GPa. This can explain a somewhat softer response predicted by the reference FE model.

A ply-by-ply distribution of the intralaminar matrix damage variable is shown in Fig-

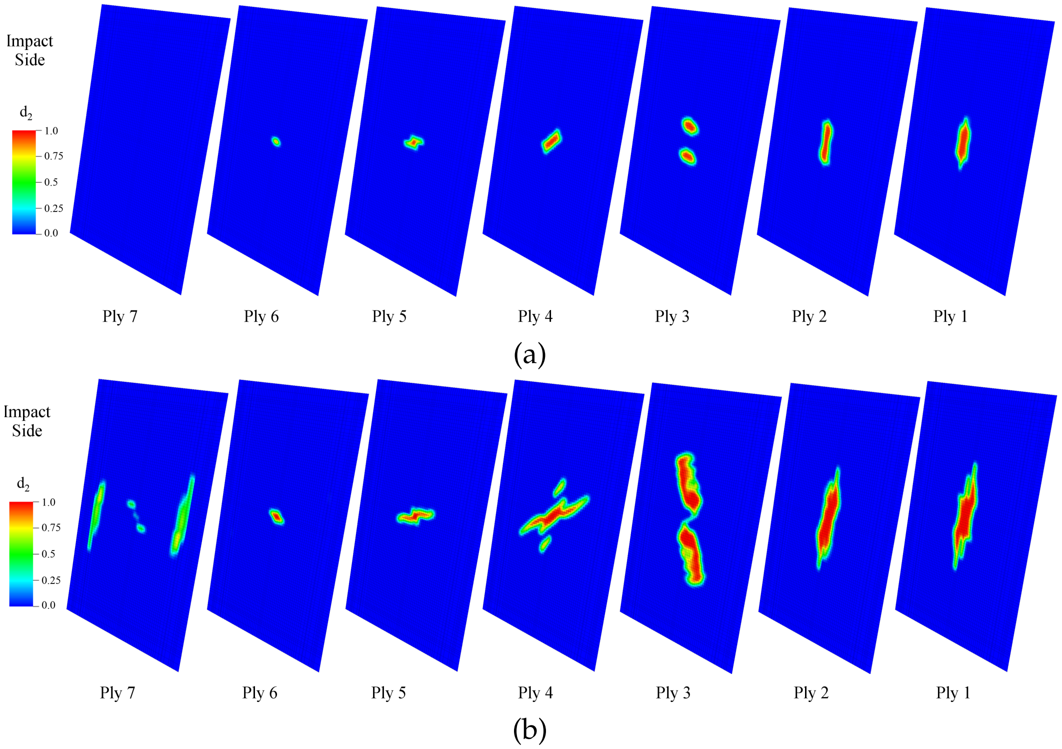

Figure 4.10: Impact on a 16-plies flat laminate. IGA-based simulation results. Intralaminar matrix damage for plies 1 (bottom) to 7 (impact side) for the (a) 6.5 J and (b) 25 J impact energy cases. Contour plots of the matrix damage variable d_2.

ures 4.10(a) and 4.10(b) for the 6.5 J and 25 J impact-energy cases, respectively. The results show a symmetric damage pattern within each ply. The most severe damage is predicted to develop on the back side of the laminate. This is because the matrix tensile stress in the lower lamina causes it to fail earlier compared to the lamina closer to the impacted side, where compressive stresses are dominant.

A interface-by-interface distribution of the interlaminar damage variable is shown in Figures 4.11(a) and 4.11(b) for the 6.5 J and 25 J impact-energy cases, respectively. The most severe delamination occurs in the lower half of the laminate, between the plies oriented at 90 and -45 degrees. We note that localized compressive stress near the impact location prevents the plies to reach complete delamination. In the case of high-energy impact, the presence of the support frame causes the initiation of interlaminar damage at the interface closest to the back of the laminate.

A comparison of matrix damage and delamination between the IGA-based and in-house FE simulations is shown in Figures 4.12 and 4.13, respectively. Discrepancies in the matrix damage are attributable to the difference in the intralaminar damage models adopted in the two simulations, and to the fact the FE simulation is able to represent a full 3D state of stress at the lamina

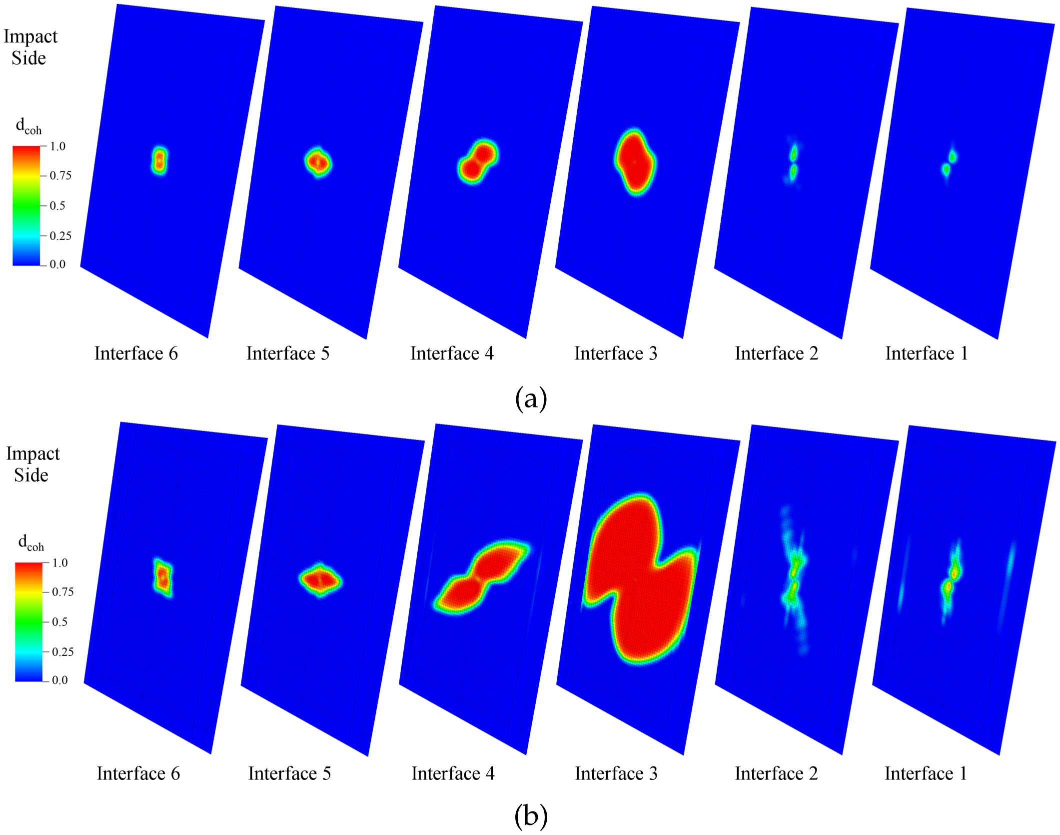

Figure 4.11: Impact on a 16-plies flat laminate. IGA-based simulation results. Interlaminar damage for cohesive interfaces 1 (bottom) to 6 (impact side) for the (a) 6.5 J and (b) 25 J impact energy cases. Contour plots of the cohesive damage variable d_{coh}.

level. Compared to the IGA results, the in-house FE model predicts a more severe and extended delamination on all the ply interfaces, especially for the higher-energy impact case. This, in turn, explains a slightly softer response of the in-house FE model for the prediction of the peak force during impact for this case.

Finally, the distribution of the matrix and of the interlaminar damage predicted by the IGA-based model is compared with the results of the reference FE model for the 6.5 J impact scenario. The comparison is shown in Figure 4.14. The dashed red line in the bottom-right panel defines the contour of the delaminated area obtained from experimental test. The models show good agreement in terms of damage extension and of its distribution on the coupon surface. Discrepancies in the predicted intralaminar damage can be attributed to different damage initiation criteria adopted for the matrix phase, which are based on the description of the state of stress in the IGA-based (plane stress) and in the reference FE (three-dimensional stress) model. The damage distribution in the matrix phase of each ply affects the local compliance of the material and, as a consequence of the displacement-based cohesive interfaces adopted for the analysis, differences in the relative

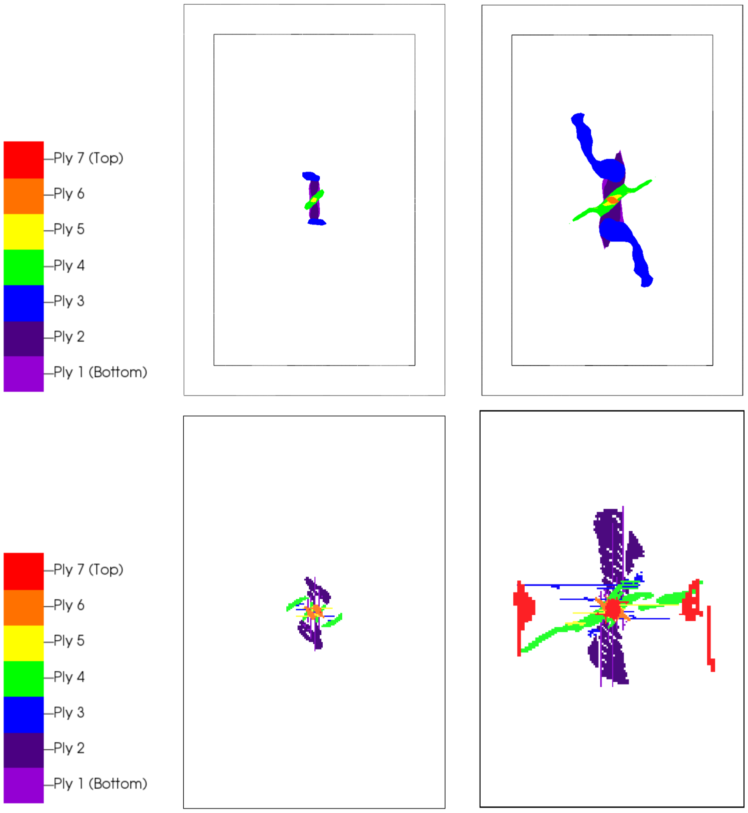

(a) (b)

Figure 4.12: Impact on a 16-plies flat laminate. Matrix failure for the (a) 6.5 J and (b) 25 J impact impact energy cases. Top: IGA-based results. Bottom: in-house FEM-based results. View from the impacted side.

displacements between the plies lead to discrepancies in the predicted interlaminar damage. It is also worth to recall that the displacement jump computed at the interface between the plies is related to the different kinematics assumptions of the thin shell and of the 3D hexahedral elements.

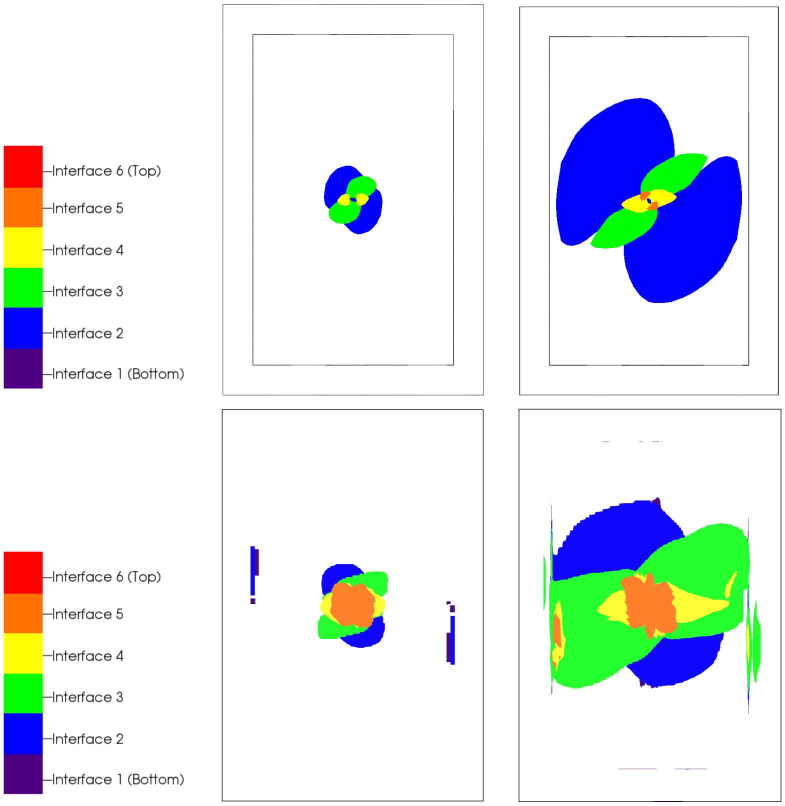

(a) (b)

Figure 4.13: Impact on a 16-plies flat laminate. Delamination for the (a) 6.5 J and (b) 25 J impact impact energy cases. Top: IGA-based results. Bottom: in-house FEM-based results. View from the impacted side.

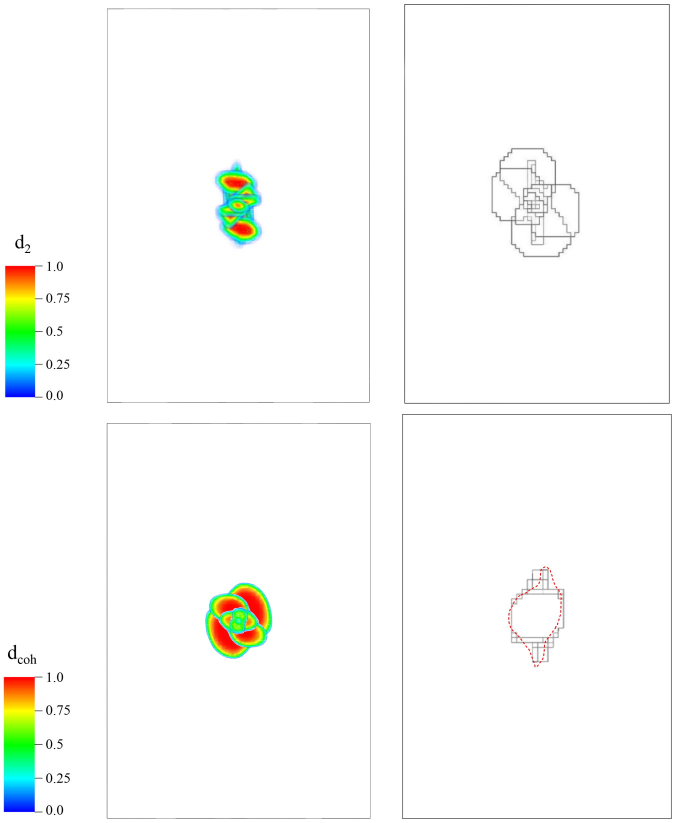

(a) (b)

Figure 4.14: Impact on a 16-plies flat laminate. Comparison of damage predicted by the (a) IGA-based and by the (b) reference FE model for the 6.5 J impact case. Contour plots of the (top) matrix damage variable d_2 and (bottom) of the cohesive damage variable d_{coh}. Source: sub-figures (b) edited from [101].

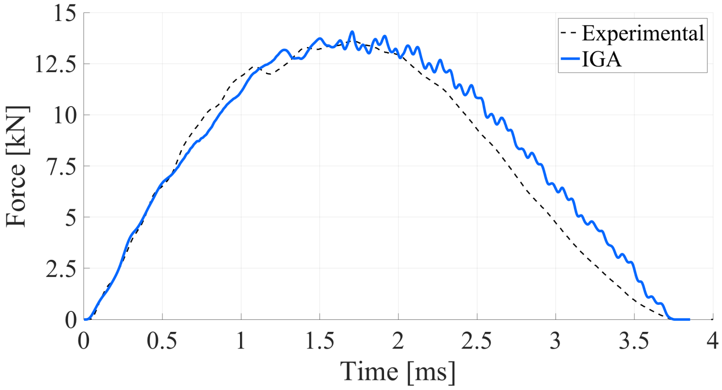

Figure 4.15: Impact on a 24-plies flat laminate. Comparison of impact-force time history.

4.4.2 Results and discussion: 24-plies flat laminate

The experimental data used for validation corresponds to a vertical drop test and post-impact non-destructive investigation of the damaged coupon conducted at the NASA Langley Research Center. Numerical simulation was performed using implicit time integration with a constant time-step of 2.5 μs. The model discretization has 436,215 DOFs. The correlation of the impact force, measured on the impacting device, is shown in Figure 4.15. The results of the IGA multi-layer shell model show excellent agreement with the experimental data. The simulation over-predicts the peak force by 3.44%, while no noticeable differences are found in the case of impact duration. No structural damping was introduced in the analysis; the oscillatory response obtained after the peak load is associated with local vibration of the panel at and near the contact interface.

Numerical results in Figures 4.16 and 4.17 show the extent of delamination front at every interface. Every sub-figure represents an individual cohesive interface. Interface numbering follows top-to-bottom ordering, where interface 23 is closest to the impacted surface. Highlighted areas identify where the cohesive damage variable $d_{\text{coh}} \geq 0.5$. For each cohesive interface, solid black lines represent the boundary of the area where the matrix damage d_2 on the plies located above and below the interface is larger than 0.5. Figures 4.16 and 4.17 demonstrate the ability of the multi-layer IGA shell model to correctly capture coupling mechanisms of matrix cracking and delamination. Although the interaction of these damage modes is not taken explicitly into account, numerical results indicate a clear correlation. In particular, it can be observed that discrepancies in the matrix damage level on two adjacent plies result in a delaminated area with boundaries aligned with those of the matrix-damage zone. This implicit interaction between the damage modes can be explained by considering that matrix damage generates in-plane variations in the compliance.

Interf. 23 (0° / 45°) Interf. 22 (45° / 90°) Interf. 21 (90° / -45°) Interf. 20 (-45° / 0°)

Interf. 19 (0° / 45°) Interf. 18 (45° / 90°) Interf. 17 (90° / -45°) Interf. 16 (-45° / 0°)

Interf. 15 (0° / 45°) Interf. 14 (45° / 90°) Interf. 13 (90° / -45°) Interf. 12 (-45° / -45°)

Figure 4.16: Impact on a 24-plies flat laminate. Correlation between matrix damage and delamination predicted by IGA simulation for cohesive interfaces 12-23. Cohesive interface 23 is at the top of the laminate (impacted side). The black solid line represents isocurves corresponding to d_2=0.5, while the highlighted area represent the sub-domain of cohesive interface where $d_{\text{coh}} \geq 0.5$.

When loads are applied, differences in compliance on two adjacent plies lead to larger displacement jump at the interface. Combined with different orientations of the connected lamina, for large enough loads, this leads to onset of permanent delamination.

In Figures 4.18 and 4.19, we compare, for every interface, the numerical prediction of delamination with experimental data obtained from rasterization of Computed Tomography (CT)

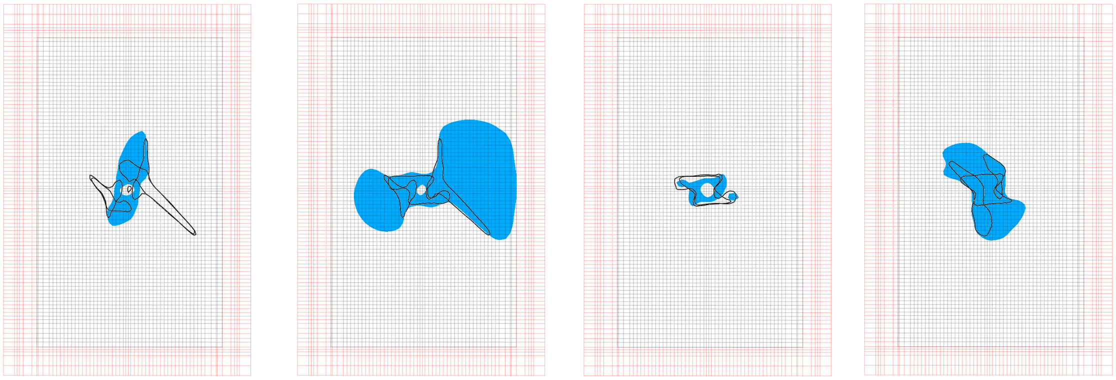

Interf. 11 (-45° / 90°) Interf. 10 (90° / 45°) Interf. 9 (45° / 0°) Interf. 8 (0° / -45°)

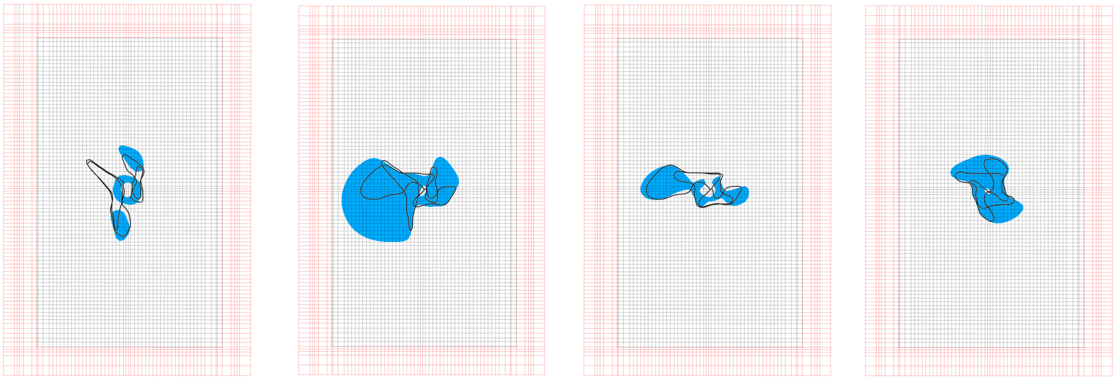

Interf. 7 (-45° / 90°) Interf. 6 (90° / 45°) Interf. 5 (45° / 0°) Interf. 4 (0° / -45°)

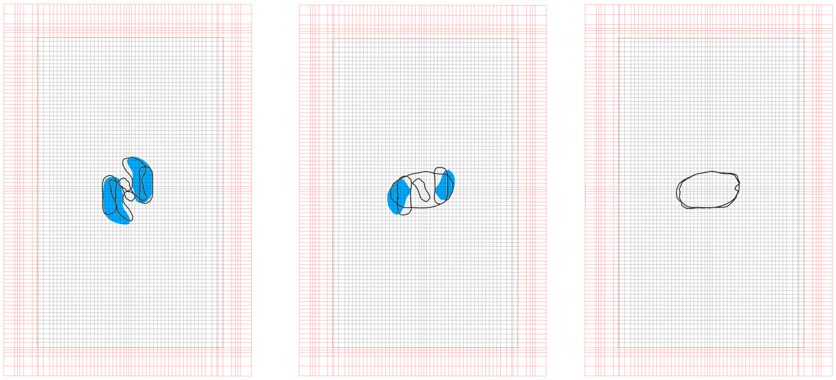

Interf. 3 (-45° / 90°) Interf. 2 (90° / 45°) Interf. 1 (45° / 0°)

Figure 4.17: Impact on a 24-plies flat laminate. Correlation between matrix damage and delamination predicted by IGA simulation for cohesive interfaces 1-11. Cohesive interface 1 is at the bottom of the laminate (non-impacted side). The black solid line represents isocurves corresponding to d_2=0.5, while the highlighted area represent the sub-domain of cohesive interface where $d_{\text{coh}} \geq$ 0.5.

images. Likewise, in Figures 4.20 and 4.21 we compare, for each ply, the matrix damage. Numerical values of cohesive and matrix damage variables are evaluated directly at the mesh quadrature points, where damage is computed, evolved, and stored. CT scans are performed on impacted specimens in order to obtain detailed information about the damage state in individual plies and

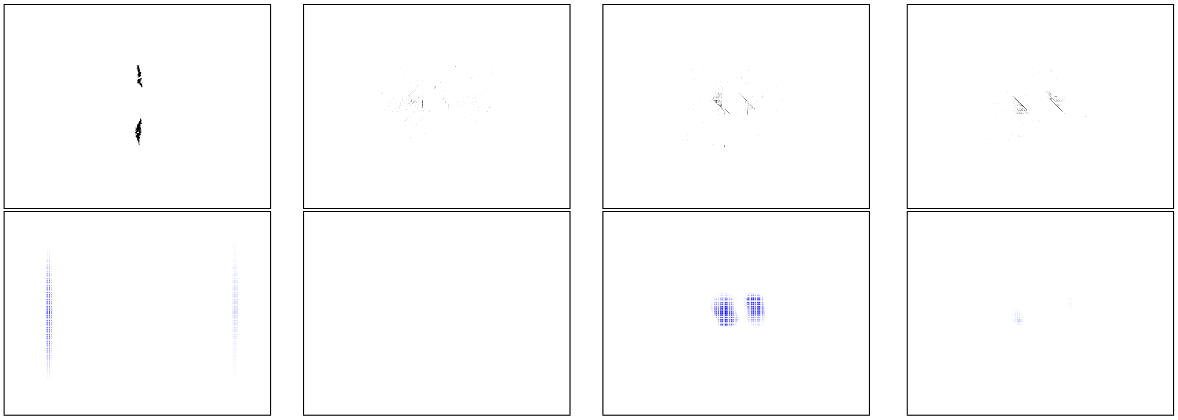

Interf. 23 (0° / 45°)
Interf. 22 (45° / 90°)
Interf. 21 (90° / -45°)
Interf. 20 (-45° / 0°)

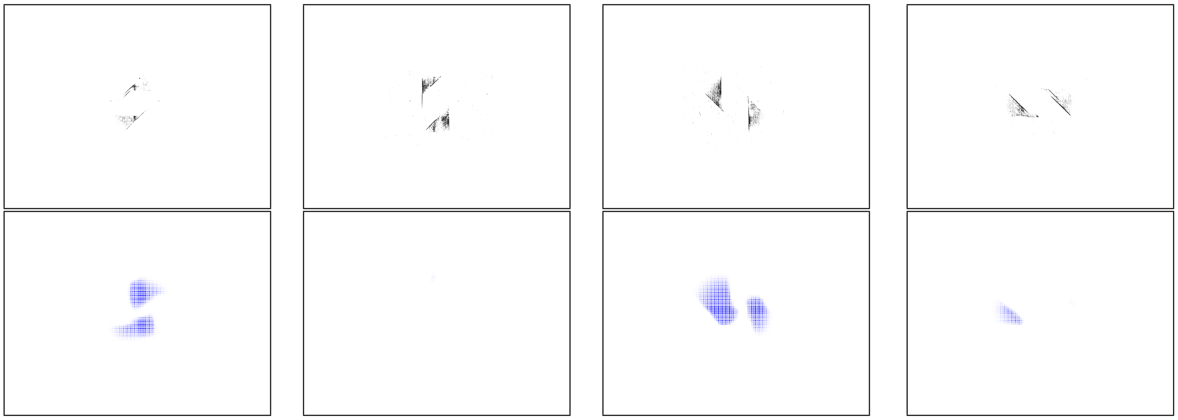

Interf. 19 (0° / 45°)
Interf. 18 (45° / 90°)
Interf. 17 (90° / -45°)
Interf. 16 (-45° / 0°)

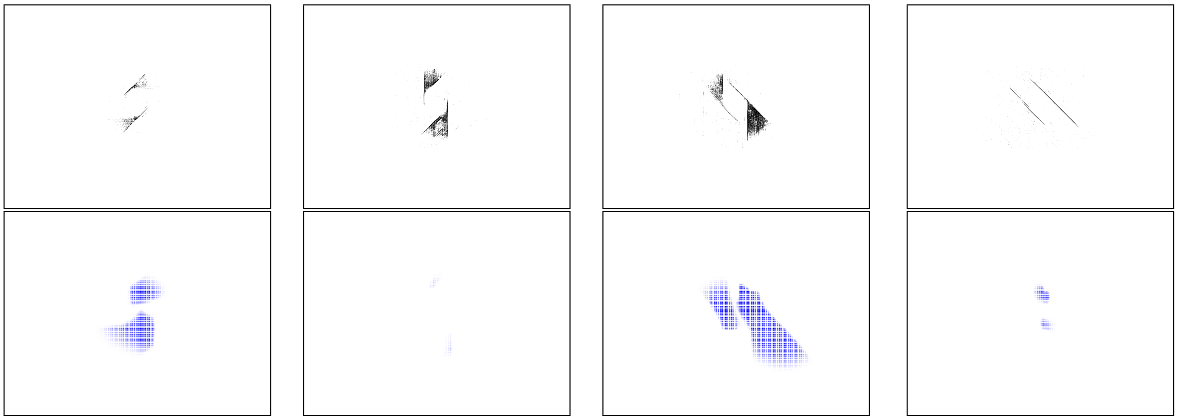

Interf. 15 (0° / 45°)
Interf. 14 (45° / 90°)
Interf. 13 (90° / -45°)
Interf. 12 (-45° / -45°)

Figure 4.18: Impact on a 24-plies flat laminate. Correlation of (top) CT-scan results and (bottom) Delamination predicted by the IGA simulation for cohesive interfaces 12-23. Cohesive interface 23 is at the top of the laminate (impacted side). Each frame represents a 80 mm × 60 mm area in the center of the panel.

at interfaces between the plies. The technique developed to extract interlaminar and intralaminar damage data from CT images is described in the work of Ellison and Kim [39].

Numerical prediction and experimental data show good correlation in terms of the orien-

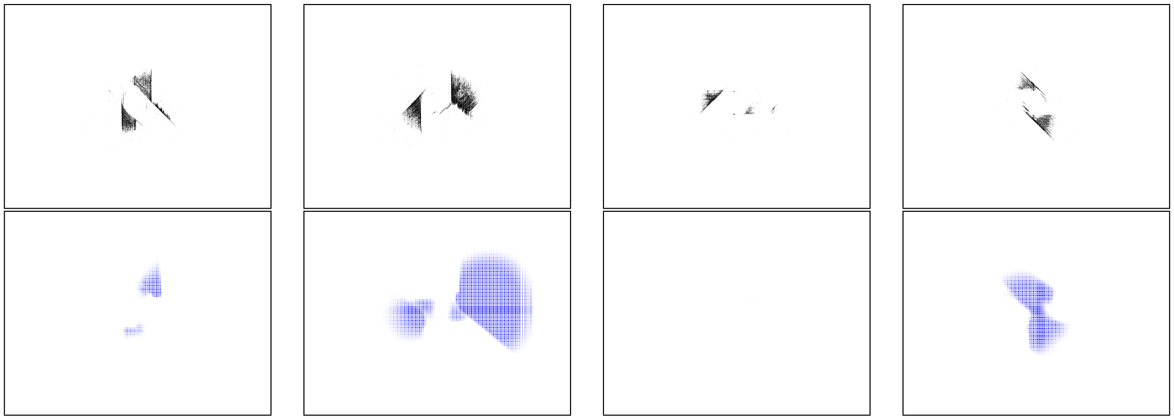

Interf. 11 (-45° / 90°) Interf. 10 (90° / 45°) Interf. 9 (45° / 0°) Interf. 8 (0° / -45°)

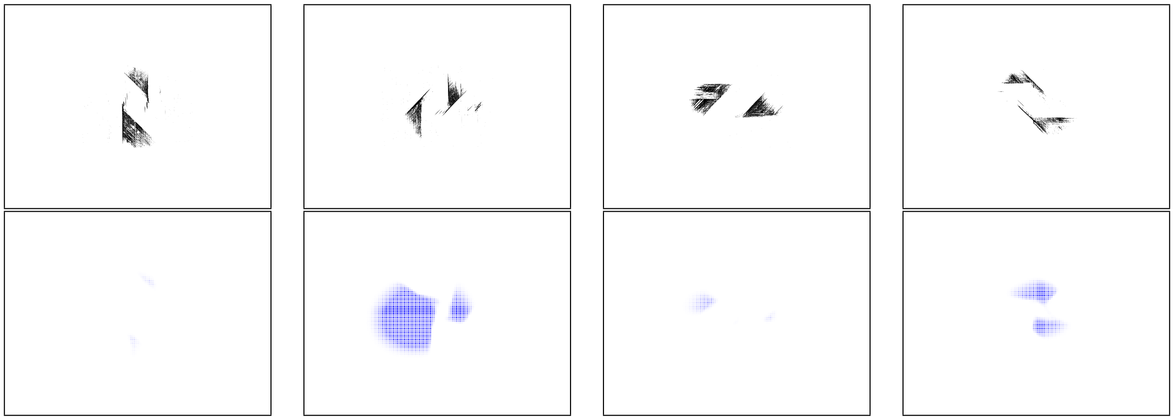

Interf. 7 (-45° / 90°) Interf. 6 (90° / 45°) Interf. 5 (45° / 0°) Interf. 4 (0° / -45°)

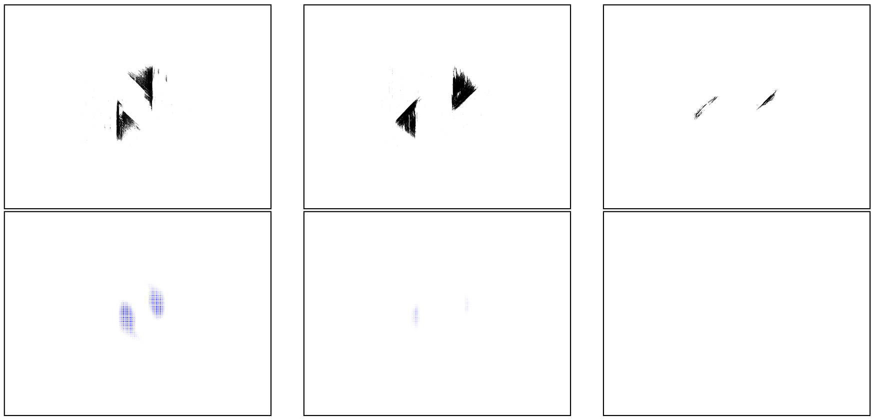

Interf. 3 (-45° / 90°) Interf. 2 (90° / 45°) Interf. 1 (45° / 0°)

Figure 4.19: Impact on a 24-plies flat laminate. Correlation of (top) CT-scan results and (bottom) Delamination predicted by the IGA simulation for cohesive interfaces 1-11. Cohesive interface 1 is at the bottom of the laminate (non-impacted side). Each frame represents a 80 mm × 60 mm area in the center of the panel.

tation of delamination boundaries and the relative extent of delamination zones. The model also accurately predicts the absence of delamination in the impact area on the upper interfaces due to the presence of compressive stress introduced by the impactor. Although the simulation tends to

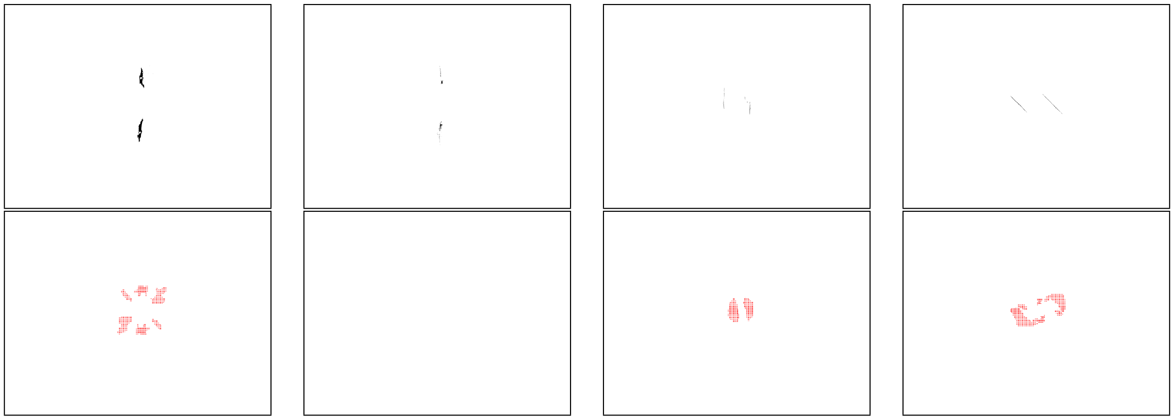
Ply 24 (0°) Ply 23 (45°) Ply 22 (90°) Ply 21 (-45°)

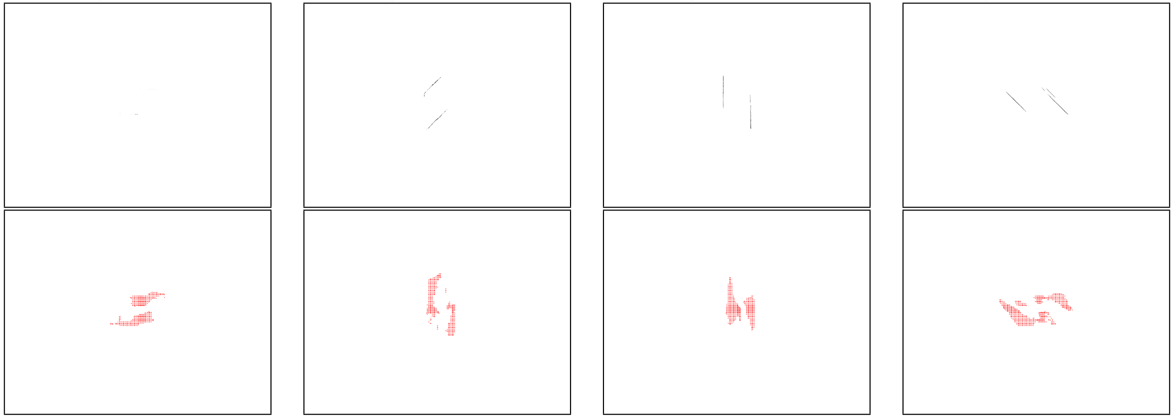
Ply 20 (0°) Ply 19 (45°) Ply 18 (90°) Ply 17 (-45°)

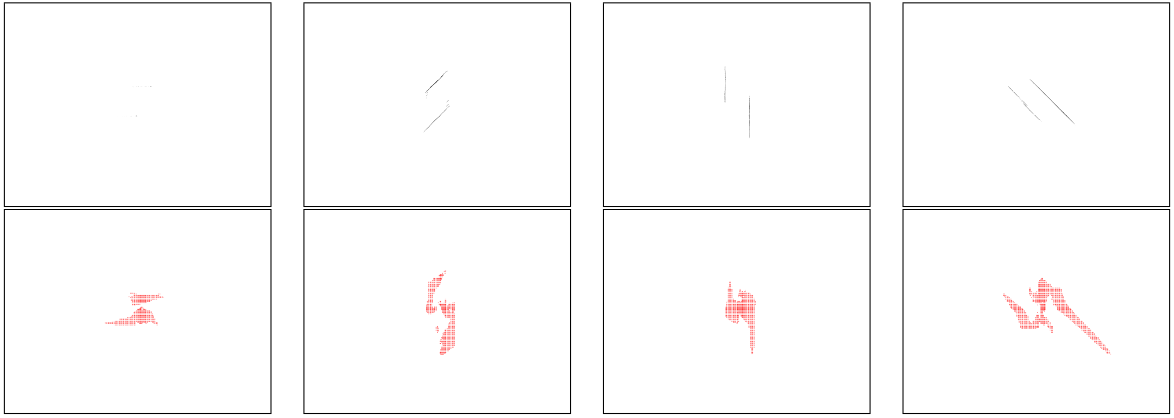
Ply 16 (0°) Ply 15 (45°) Ply 14 (90°) Ply 13 (-45°)

Figure 4.20: Impact on a 24-plies flat laminate. Correlation of (top) CT-scan results and (bottom) Matrix damage predicted by the IGA simulation for plies 13-24. Ply 24 is at the top of the laminate (impacted side). Each frame represents a 80 mm × 60 mm area in the center of the panel.

predict larger interlaminar and intralaminar damage compared to experimental observation, it is worth noting that rasterization of CT images introduces some level of arbitrariness in the definition of the damage extent.


Ply 12 (-45°)
Ply 11 (90°)
Ply 10 (45°)
Ply 9 (0°)
Ply 8 (-45°)
Ply 7 (90°)
Ply 6 (45°)
Ply 5 (0°)
Ply 4 (-45°)
Ply 3 (90°)
Ply 2 (45°)
Ply 1 (0°)

Figure 4.21: Impact on a 24-plies flat laminate. Correlation of (top) CT-scan results and (bottom) Matrix damage predicted by the IGA simulation for plies 1-12. Ply 1 is at the bottom of the laminate (non-impacted side). Each frame represents a 80 mm × 60 mm area in the center of the panel.

The discrete nature of matrix cracking is clearly visible in the processed CT images, where damage appears to be confined along narrow crack-bands oriented parallel to fiber direction. The orientation and length of matrix cracks predicted by the numerical model is in good agreement with the CT results. However, the extent of matrix damage is larger compared to experimental observations. These discrepancies can be attributed to the continuous nature of models based on damage mechanics, where the predicted damage areas represent the effect of coalescence of parallel crack-bands aligned in the fiber direction.

4.4.3 Results and discussion: Stiffened panel

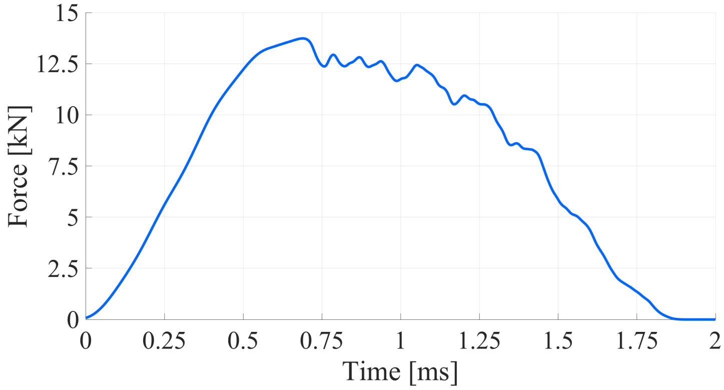

Figure 4.22: Impact simulation on a stringer-stiffened panel. Impact-force time history obtained from the IGA simulation.

The low velocity impact scenario on reinforced composite panel is investigated from a numerical point of view only. Experimental data are not presently available for this case. Numerical simulations are performed using implicit time integration with a constant time step of 2.0 μs. The IGA model uses 75,891 displacement-only DOFs for the discretization of the problem. The impact force time history, shown in Figure 4.22, exhibits a sharp drop related to a sudden propagation of the delamination front at the interface between the skin and 90° ply.

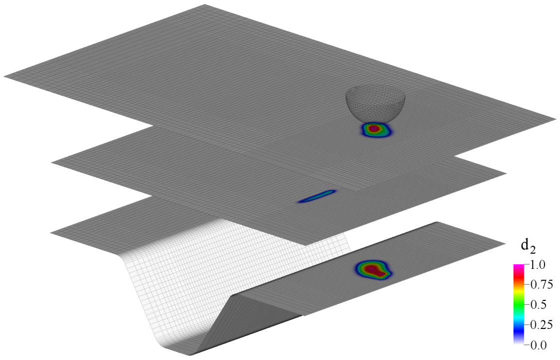

Figure 4.23: Impact on a stiffened panel. Contour plot of the intralaminar matrix damage variable d_2: envelope of maximum damage obtained for each ply of the laminate.

Figures 4.23 and 4.24 show the contour plots of matrix and interlaminar damage, respectively. Since ply grouping technique is enabled, we report the envelope of damage variable d_2 obtained, for each point, by taking its maximum value in the through-thickness direction on all the the plies of the laminate. As expected, matrix damage is confined to the impact area, while the extension of matrix damage is larger on the stringer, where tensile stresses are dominant.

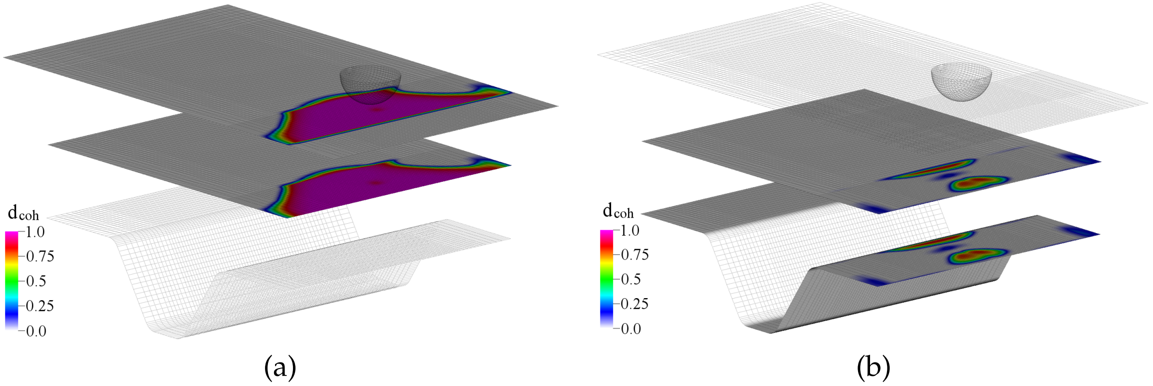

(a) (b)

Figure 4.24: Impact on a stiffened panel. Contour plots of the interlaminar damage variable d_{coh}: interface (a) skin / 90° ply and (b) 90° ply / stringer flange.

Remark Enabling ply grouping allows for significant improvements in computational performance, while still satisfying mesh size requirements for continuum damage and delamination. On the other hand, this approach artificially prevents delamination of plies that belong to the same group. Particular attention to ply grouping choices is therefore required since delamination significantly affects the laminate residual bending stiffness.

4.5 Hard landing simulation of a UAV

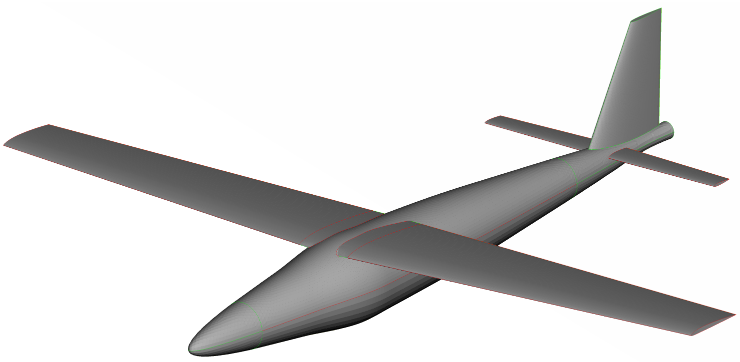

Figure 4.25: Simplified CAD model of the Aurora Flight Sciences LCAAT UAV. *Courtesy of Prof. A. Korobenko, U. Calgary.*

In this section we present an application of the design-to-analysis concept, which is the key idea behind IGA and drives much of the research and development in this area. The IGA multi-layer modeling approach is applied for progressive damage simulation of a full-scale Unmanned Aerial Vehicle (UAV). The UAV is a prototype designed and manufactured by Aurora Flight Sciences with a wingspan of 3.66 m. It belongs to a new class of air vehicles developed within the Low Cost

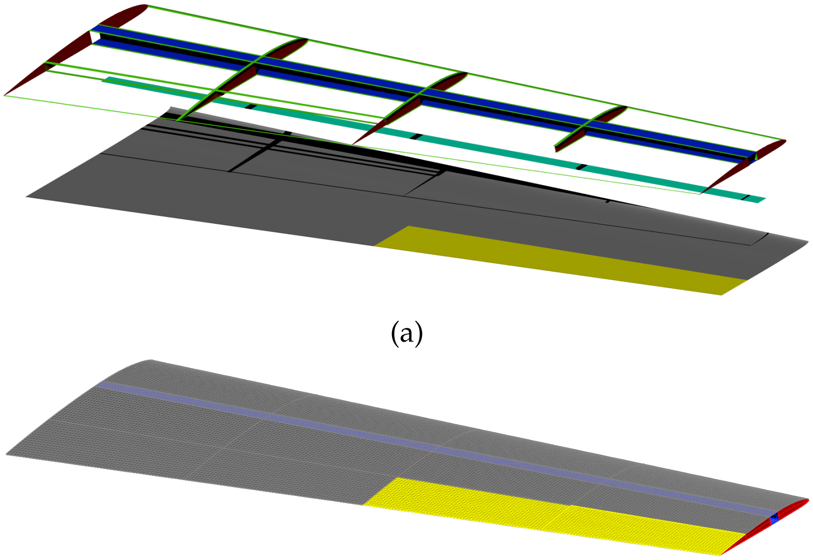

(a)

(b)

Figure 4.26: Detailed NURBS-based CAD model of the LCAAT semi-wing for IGA: (a) View of the internal structural components and (b) Global view of the assembled wing. In (a), the following color code is used to distinguish structural parts: (gray) skin, (blue) spar, (red) ribs, (yellow) ailerons. Non-structural geometries are also represented: (green) bending strips and (blue-green) cohesive interface.

Attritable Aircraft Technology (LCAAT) research program managed by the US Air Force Research Laboratory. A simplified CAD model of the LCAAT UAV is shown in Figure 4.25.

We investigate the structural response of the UAV main wing, focusing on the skin / spar cap debonding that may occur during a hard landing scenario. The fuselage is not modeled and the analysis is performed under the conservative assumption that the impact loads are transferred directly to the wing. The wing presents a traditional single-spar design with four ribs and one reinforced rib at the wing root. The spar runs for the entire length of the wing. The IGA model is comprised of 127 NURBS patches that are used to represent all structural components, such as spar, ribs, and skin, as well as aerodynamic surfaces. The ply grouping technique is adopted for computational efficiency. Cohesive interfaces are used to connect the skin to spar caps. The properties employed in the current analysis are reported in Table 4.2.

We make use of the commercial CAD software Rhinoceros3D [76] for modeling purposes in order to create the basic geometry and carry out mesh refinement required for simulation. It is worth mentioning that NURBS-based CAD software, in general, represent surfaces using the minimum required number of control points such that the geometry is visually accurate. For analysis purposes, however, *h-refinement* (i.e., increasing the number of non-repeated knots in the NURBS parametric space) or *p-refinement* (i.e., increasing the polynomial order of the NURBS

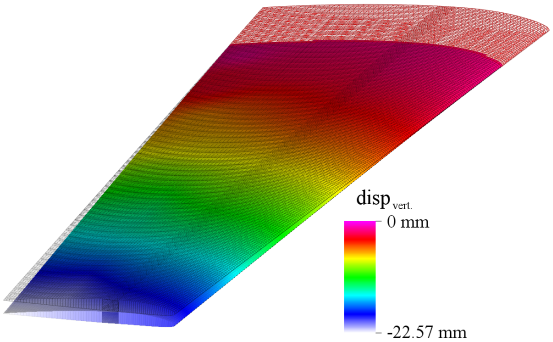

Figure 4.27: Hard landing simulation of LCAAT UAV. Contour plot of the vertical displacement. Mesh in the undeformed configuration is superimposed to visualize wing deformation. Contour color is not reported for those elements at wing's root where acceleration is imposed.

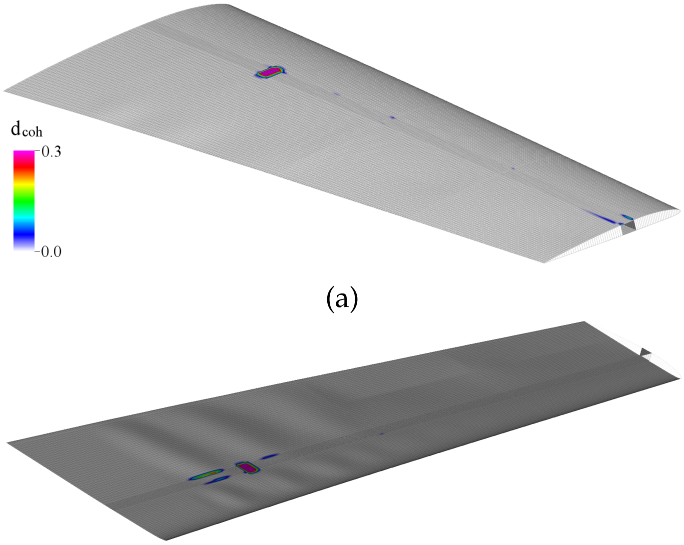

(a)

(b)

Figure 4.28: Hard landing simulation of LCAAT UAV. Contours plots of the cohesive damage variable d_{coh} on (a) Top of the wing and (b) Bottom of the wing.

functions while keeping the number of non-repeated knots constant) are often required to achieve sufficient accuracy. A detailed description of the refinement procedures is reported by Cottrell et al. [32]. These refinement procedures may be *performed directly in the CAD environment*, which is one of the more attractive features of the IGA approach. The final, analysis-ready UAV wing NURBS model and mesh are shown in Figure 4.26.

A hard landing simulation is performed by imposing an initial uniform downward velocity of 3 m/s on the entire semi-wing. An upward acceleration ramp from 0 g to 6 g is imposed in the time frame 0 s to 0.1 s. Boundary conditions are imposed on the portion of the wing that is connected to the fuselage (not modeled). After 0.1 s, the deceleration is kept constant until the constrained control points come to rest. Numerical simulations are performed using implicit time integration with a constant time step of 0.5 ms. The model uses 129,626 DOFs for the discretization of the problem. Simulation results are shown in Figure 4.27, where the deformed configuration is represented at the moment of maximum deflection. Figure 4.28 shows the distribution of the interlaminar damage on the connection between the spar cap and skin. Despite the presence of a delamination trigger, introduced *ad-hoc* on both sides of the wind to facilitate the propagation of the delamination front, the model predicts the onset of interlaminar damage in the area closer to the wing-fuselage connection. In this area, stresses in the spar are high, giving rise to interlaminar shear due to different elastic properties between the spar cap and skin.

4.6 Acknowledgments

Chapter 4 is, in full, an edited reprint of the material as it appears in:

- *"A new multi-layer approach for progressive damage simulation in composite laminates based on isogeometric analysis and Kirchhoff–Love shells. Part I: basic theory and modeling of delamination and transverse shear"*, published on-line in *"Computational Mechanics"* on November 30th 2017 and co-authored by *Marco S. Pigazzini, Yuri Bazilevs, Andrew C. Ellison, and Hyonny Kim*. This article is currently in press. The author of this dissertation *(Marco S. Pigazzini)* is one of the primary investigators and authors of this paper.
- *"A new multi-layer approach for progressive damage simulation in composite laminates based on isogeometric analysis and Kirchhoff–Love shells. Part II: impact modeling"*, published on-line in *"Computational Mechanics"* on November 24th 2017 and co-authored by *Marco S. Pigazzini, Yuri Bazilevs, Andrew C. Ellison, and Hyonny Kim*. This article is currently in press. The author of this dissertation *(Marco S. Pigazzini)* is the primary investigator and author of this paper.
- *Isogeometric analysis for simulation of progressive damage in composite laminates*, published on-line on April 22nd 2018 in *Journal of Composite Materials* and co-authored by *Marco S. Pigazzini, Yuri Bazilevs, Andrew C. Ellison, and Hyonny Kim*. This article is currently in press. The author of this dissertation *(Marco S. Pigazzini)* is the primary investigator and author of this paper.

The development of the multi-layer model presented in this work was supported by NASA Advanced Composites Project No. 15-ACP1-0021. The co-authors of the articles [14, 84, 85] and I thank Dr. F. Leone, Dr. C. Rose, and Dr. C. Davila from NASA Langley Research Center for their valuable comments and suggestions. The authors would like to thank Mr. W. Jackson of NASA Langley for providing the CT scan data used in this paper. The research related to the LCAAT UAV prototype was supported by the AFOSR within the Dynamic Data Driven Application System project, Award No. FA9550-16-1-0131. The co-authors of the article [85] and I thank Dr. E. Blasch and Dr. F. Darema for the their support. I want to express out gratitude to C. Kays of Aurora Flight Sciences for providing technical support in the development of the UAV structural model. Finally, I would like to thank Prof. A. Korobenko at the University of Calgary, Canada, for providing the exterior CAD model of the LCAAT UAV prototype.

5 Gradient–enhanced damage modeling in Kirchhoff–Love shells

This chapter aims to address the issue of material instability, which typically affects strain-softening damage models described in the previous chapters. We begin, in Section 5.1, by formulating a strain-smoothing model for the Green–Lagrange strain, for a general 3D continuum. In contrast to much prior work on gradient damage, we smooth the full tensor-valued strain (rather than a scalar effective strain), to account for the anisotropic damage modes of fiber-reinforced composites. Further, we formulate our model using the tensor generalization of the Laplace–Beltrami operator on manifolds and provide formulas for arbitrary coordinate charts, to facilitate the reduction to a shell theory. Section 5.2 specializes this model to the case of a thin shell by introducing kinematic assumptions, and Section 5.3 applies it to laminated composite shells. In Section 5.5, we provide several examples illustrating the validity and general applicability of the new gradient damage model.

5.1 Gradient-Enhanced damage on manifolds

Building on our prior work [36, 14, 84] on continuum damage in composite shell structures, we assume that the damage law is driven by the Green–Lagrange strain, which encapsulates information about the change in length of small line segments embedded in a deforming material. For an un-deformed body modeled by manifold Ω_0, mapped to a deformed body Ω by the motion ϕ, the Green–Lagrange strain $\mathbf{E}$ satisfies:

$$2\mathbf{E}^{\flat} = \phi^{*}(\mathbf{g}) - \mathbf{G}\,, \tag{5.1}$$

where $\mathbf{g}$ is the metric tensor on Ω, $\mathbf{G}$ is the metric tensor on Ω_0, ϕ^{*} is the pull-back by ϕ, and the superscript $\flat$ indicates an associated tensor taking all vector arguments. The $\sharp$ symbol will be used to denote an associated tensor taking all co-vector arguments. For a review of mathematical prerequisites for large-strain elasticity, refer to [74, Chapter 1], whose notational conventions we largely follow. In index notation, the pulled-back metric is given by:

$$(\phi^*(\mathbf{g}))_{AB} = g_{ab} F^a{}_A F^b{}_B \ , \tag{5.2}$$

where $\mathbf{F} = D\phi$ is the deformation gradient, raised indices indicate co-vector arguments, lowered indices indicate vector arguments, and repeated indices denote contraction. We follow the convention that lower-case Roman-letter indices correspond to tensor arguments in (co)tangent spaces of points in Ω, while upper-case Roman-letter indices refer to Ω_0. The formula (5.1) becomes the familiar $\mathbf{F}^T\mathbf{F} - \mathbf{I}$ in Cartesian coordinates, with $g_{ab} = \delta_{ab}$, $G_{AB} = \delta_{AB}$, and $(\cdot)^T$ understood as matrix transposition (vs. [74, Proposition 3.4(ii), Chapter 1]), but we retain the generality of the manifold viewpoint here, to facilitate reduction to a shell theory.

To avoid unstable strain localization, we propose to instead drive damage with a smoothed Green–Lagrange strain. We build on the Gradient-Enhanced damage model of [82], in which a scalar effective strain ε_0 is smoothed to obtain $\widetilde{\varepsilon}_0$ satisfying the PDE:

$$\widetilde{\varepsilon}_0 - c\Delta\widetilde{\varepsilon}_0 = \varepsilon_0 \ , \tag{5.3}$$

where c is a scalar parameter with dimensions of area and Δ is the Laplace operator. By analogy, we consider a smoothed Green–Lagrange strain $\widetilde{\mathbf{E}}$ satisfying the PDE:

$$\widetilde{\mathbf{E}} - \mathrm{DIV}\left(\mathbf{c}\,\mathrm{GRAD}\,\widetilde{\mathbf{E}}\right) = \mathbf{E} \ , \tag{5.4}$$

where DIV and GRAD are the divergence and gradient operators on the reference configuration Ω_0, and the tensor $\mathbf{c}$ permits anisotropy in the strain smoothing. The full tensor-valued strain $\mathbf{E}$ is smoothed because the damage model of [14] requires anisotropic strain information. The smoothed strain $\widetilde{\mathbf{E}}$ will then be used in place of the Green–Lagrange strain to drive damage evolution. Multiplying by a tensor-valued test function $\mathbf{W}$, integrating by parts, and (again following [82] by analogy) assuming natural boundary conditions (i.e., $\left(\mathbf{c}\,\mathrm{GRAD}\,\widetilde{\mathbf{E}}\right) \cdot \mathbf{N} = \mathbf{0}$, where $\mathbf{N}$ is the outward normal to $\partial\Omega_0$), we obtain the weak form: Find $\widetilde{\mathbf{E}}^\flat \in \mathcal{V}_E$ such that for all $\mathbf{W}^\flat \in \mathcal{V}_E$:

$$\int_{\Omega_0} \widetilde{\mathbf{E}}^\flat : \mathbf{W}^\sharp \, d\Omega_0 + \int_{\Omega_0} \left(\mathbf{c}\,\mathrm{GRAD}\,\widetilde{\mathbf{E}}\right)^\flat : (\mathrm{GRAD}\,\mathbf{W})^\sharp \, d\Omega_0 = \int_{\Omega_0} \mathbf{E}^\flat : \mathbf{W}^\sharp \, d\Omega_0 \ , \tag{5.5}$$

where the tensor contraction operator " : " indicates contraction over all indices of its operands, i.e., (cf. [74, Definition 4.12, Chapter 1]):

$$\mathbf{S}^\flat : \mathbf{T}^\sharp = S_{ABC\ldots} T^{ABC\ldots} \ . \tag{5.6}$$

In index notation, (5.5) may be written unambiguously:

$$\int_{\Omega_0} \widetilde{E}_{AB} W^{AB}\, d\Omega_0 + \int_{\Omega_0} c^F{}_G \widetilde{E}_{AB|C} W_{DE|F} G^{DA} G^{EB} G^{GC}\, d\Omega_0 = \int_{\Omega_0} E_{AB} W^{AB}\, d\Omega_0 \,, \tag{5.7}$$

where the vertical stroke " | " indicates covariant differentiation and G^{AB} are components of $\mathbf{G}^{-1}$. For a tensor $\mathbf{A}$ of type $\binom{0}{2}$, covariant differentiation can be expressed in a coordinate chart $\{\xi^A\}$ as [74, Box 4.1, Chapter 1]:

$$(\nabla \mathbf{A})_{ABC} = A_{AB|C} = A_{AB,C} - A_{DB}\Gamma^D_{AC} - A_{AD}\Gamma^D_{BC} \,, \tag{5.8}$$

where the comma indicates partial differentiation and the Γs are Christoffel symbols, i.e.,

$$\nabla_{\mathbf{G}_A} \mathbf{G}_B = \Gamma^C_{AB} \mathbf{G}_C \,, \tag{5.9}$$

in which $\nabla_{\mathbf{w}}$ denotes covariant differentiation in the direction $\mathbf{w}$ and

$$\mathbf{G}_A = \frac{\partial}{\partial \xi^A} \tag{5.10}$$

are the covariant basis vectors associated with the coordinates.

5.2 Specialization for thin shells

We now choose a particular coordinate chart tailored to the case of a thin shell structure whose thickness, h_{th}, is assumed to be much smaller than the overall size of the structure. Let $\{\xi^\alpha\}_{\alpha=1}^2$ be coordinates of the shell structure's 2D un-deformed midsurface, Γ_0, and let the coordinate $\xi^3 \in [-h_{\text{th}}/2, h_{\text{th}}/2]$ parameterize the through-thickness direction orthogonal to Γ_0. Unless otherwise specified, we follow the notational convention that Greek-letter indices have range 1,2, while Roman-letter indices have range 1,2,3. Assuming standard Kirchhoff–Love kinematics, we consider:

$$E_{\alpha 3} = E_{3\alpha} = E_{33} = 0 \,, \tag{5.11}$$

and likewise for $\widetilde{\mathbf{E}}$ and $\mathbf{W}$. We make the further approximation that $\{\mathbf{G}_\alpha\}$ do not depend on ξ^3. This contradicts (5.10) unless Γ_0 is flat, but it is consistent with the assumptions frequently made to permit analytical through-thickness integration of Kirchhoff–Love shell formulations, as in [68]; see [19, Section 4.4.4] for more detailed justification. With this assumption, $\nabla_{\mathbf{G}_3} \mathbf{G}_\alpha = \mathbf{0}$, or

$$\Gamma^B_{\alpha 3} = \Gamma^B_{3\alpha} = 0 \,. \tag{5.12}$$

Kirchhoff–Love thin shell kinematics allow for a separation of membrane and bending components of the in-plane strain, so that:

$$\mathrm{E}_{\alpha\beta} = \varepsilon_{\alpha\beta} + \xi^3 \kappa_{\alpha\beta} \;, \tag{5.13}$$

$$\widetilde{\mathrm{E}}_{\alpha\beta} = \widetilde{\varepsilon}_{\alpha\beta} + \xi^3 \widetilde{\kappa}_{\alpha\beta} \;, \tag{5.14}$$

$$W_{\alpha\beta} = \delta\varepsilon_{\alpha\beta} + \xi^3 \delta\kappa_{\alpha\beta} \;, \tag{5.15}$$

where $\boldsymbol{\varepsilon}$ and $\boldsymbol{\kappa}$ are membrane and curvature-change strains (defined by [14, Section 2.1]), $\widetilde{\boldsymbol{\varepsilon}}$ and $\widetilde{\boldsymbol{\kappa}}$ are their smoothed counterparts, and $\delta\boldsymbol{\varepsilon}$ and $\delta\boldsymbol{\kappa}$ are the corresponding test functions. Due to our use of midsurface basis vectors $\{\mathbf{G}_\alpha\}$ through the entire thickness, $\mathbf{E}^\flat$ in (5.13) operates on tangent vectors of Γ_0 for all ξ^3. (We acknowledge the slight abuse of notation, in using the same symbol for the 3D continuum strain, operating on tangent vectors of Ω_0.) Given the strain decompositions (5.13)–(5.15), we may split the weak problem (5.5) into two independent problems. First: Find $\widetilde{\boldsymbol{\varepsilon}}$ such that for all $\delta\boldsymbol{\varepsilon}$,

$$h_{\mathrm{th}} \left(\int_{\Gamma_0} \widetilde{\varepsilon}_{\alpha\beta}\, \delta\varepsilon^{\alpha\beta}\, d\Gamma_0 + \int_{\Gamma_0} c^{\zeta}{}_{\nu}\, \widetilde{\varepsilon}_{\alpha\beta|\gamma}\, \delta\varepsilon_{\delta\epsilon|\zeta} G^{\delta\alpha} G^{\epsilon\beta} G^{\gamma\nu}\, d\Gamma_0 \right) = h_{\mathrm{th}} \int_{\Gamma_0} \varepsilon_{\alpha\beta}\, \delta\varepsilon^{\alpha\beta}\, d\Gamma_0 \tag{5.16}$$

and, second: Find $\widetilde{\boldsymbol{\kappa}}$ such that for all $\delta\boldsymbol{\kappa}$,

$$\begin{aligned} &\frac{h_{\mathrm{th}}^3}{12} \left(\int_{\Gamma_0} \widetilde{\kappa}_{\alpha\beta}\, \delta\kappa^{\alpha\beta}\, d\Gamma_0 + \int_{\Gamma_0} c^{\zeta}{}_{\nu}\, \widetilde{\kappa}_{\alpha\beta|\gamma}\, \delta\kappa_{\delta\epsilon|\zeta} G^{\delta\alpha} G^{\epsilon\beta} G^{\gamma\nu}\, d\Gamma_0 \right) \\ &\qquad + h_{\mathrm{th}} \int_{\Gamma_0} c^3{}_3\, \widetilde{\kappa}_{\alpha\beta}\, \delta\kappa^{\alpha\beta}\, d\Gamma_0 = \frac{h_{\mathrm{th}}^3}{12} \int_{\Gamma_0} \kappa_{\alpha\beta}\, \delta\kappa^{\alpha\beta}\, d\Gamma_0 \;. \end{aligned} \tag{5.17}$$

Terms coupling $\widetilde{\boldsymbol{\varepsilon}}$ and $\widetilde{\boldsymbol{\kappa}}$ have canceled, due to integration of odd powers of ξ^3 over the symmetric interval $(-h_{\mathrm{th}}/2, h_{\mathrm{th}}/2)$. The "extra" term proportional to h_{th} in (5.17) comes from smoothing of 3D strain in the ξ^3 direction:

$$\widetilde{\mathrm{E}}_{\alpha\beta|3} = \frac{\partial \left(\widetilde{\varepsilon}_{\alpha\beta} + \xi^3 \widetilde{\kappa}_{\alpha\beta} \right)}{\partial \xi^3} - \widetilde{\mathrm{E}}_{D\beta} \Gamma^D_{\alpha 3} - \widetilde{\mathrm{E}}_{\alpha D} \Gamma^D_{\beta 3} = \widetilde{\kappa}_{\alpha\beta} \tag{5.18}$$

and, likewise,

$$W_{\alpha\beta|3} = \delta\kappa_{\alpha\beta} \;, \tag{5.19}$$

so that:

$$\widetilde{\mathrm{E}}_{\alpha\beta|3} W^{\alpha\beta}{}_{|3} G^{33} = \widetilde{\kappa}_{\alpha\beta}\, \delta\kappa^{\alpha\beta} \;, \tag{5.20}$$

where we use assumptions (5.12) in the second equality of (5.18), and the fact that $G^{33} = 1$ in (5.20). This additional term will dominate the problem for $\widetilde{\boldsymbol{\kappa}}$ in the limit of $h_{\mathrm{th}} \to 0$, driving $\widetilde{\boldsymbol{\kappa}} \to \mathbf{0}$. This is expected when smoothing the odd-in-ξ^3 function $\xi^3\widetilde{\boldsymbol{\kappa}}$ over a small interval about $\xi^3 = 0$.

Remark 1. The use of covariant differentiation in the diffusive terms of (5.16) and (5.17) ensures that damage models relying on the smoothed strain will be independent of the choice of coordinates on Γ_0. Most prior studies on Gradient-Enhanced damage (and related phase field methods) smooth only a scalar-valued field, say, s, in which case $s_{|\alpha} = s_{,\alpha}$. However, this is no longer true for higher-rank fields.

5.3 Application to continuum damage modeling for laminated composite shells

Following our earlier work [14], we model multi-layer laminated composite shell structures as collections of Kirchhoff–Love thin shells coupled through cohesive zones, with one Kirchhoff–Love shell representing each lamina. The problem (5.16) is used to determine the smoothed membrane strain in each of these layers. Based on the assumption that the individual laminae are very thin, we assume that $\widetilde{\boldsymbol{\kappa}} = \mathbf{0}$, as implied by the $h_{\text{th}} \to 0$ limit of (5.17). This *does not* preclude damage due to bending of the full laminated shell; laminae away from the neutral axis will have nonzero membrane strains. For a single ply, then, we have $\widetilde{\mathbf{E}}^\flat = \widetilde{\boldsymbol{\varepsilon}}$ for all $\xi^3 \in [-h_{\text{th}}/2, h_{\text{th}}/2]$ For the ply group construction of [14, Section 2.2], in which a collection of lamina are represented by a single Kirchhoff–Love shell, but may be damaged independently, we modify this to:

$$\widetilde{\mathbf{E}}^\flat_k = \widetilde{\boldsymbol{\varepsilon}} + \xi^3_k \boldsymbol{\kappa} \,, \tag{5.21}$$

where $\widetilde{\mathbf{E}}^\flat_k$ is the smoothed strain within the k^{th} ply, ξ^3_k is the through-thickness coordinate of the midsurface of the k^{th} ply, $\widetilde{\boldsymbol{\varepsilon}}$ is the smoothed membrane strain of the entire group, and $\boldsymbol{\kappa}$ is the *un*smoothed bending strain of the group. This assumes that individual plies are thin enough to consider $\widetilde{\mathbf{E}}$ constant through the thickness of each ply, but still permits damage to be caused by pure bending movements of the ply group. We re-use the damage model detailed in [14, Section 3], but alter the definitions of the "equivalent displacements" that are used to drive the evolution of damage parameters associated with different damage modes. As in [14], we consider each lamina to be composed of an orthotropic material, reinforced by fibers aligned along a single direction. We consider four distinct modes of damage in such materials:

- Mode 1_T: Fiber breaking under tension.
- Mode 1_C: Fiber buckling under compression.
- Mode 2_T: Matrix cracking under transverse tension and shear.

- Mode 2_C: Matrix cracking under transverse compression and shear.

These modes are associated with equivalent displacements $\hat{\delta}_{1_T}$, $\hat{\delta}_{1_C}$, $\hat{\delta}_{2_T}$, and $\hat{\delta}_{2_C}$. Equivalent displacements are computed from dimensionless strains through multiplication by a length scale. In the case of local damage models, this length scale is tied to the choice of discretization, and is chosen to be the smallest distance within which strains can be localized in a discrete displacement field, in an attempt to prevent mesh-dependent energy dissipation. However, the choice of length scale is by heuristic, at best, for problems discretized on general unstructured meshes in multiple space dimensions. In the case of Gradient-Enhanced damage modeling, the localization of strains is controlled by the model parameter c, and we may consider $\sqrt{c}$ to be an appropriate mesh-independent length scale for computing equivalent displacements from smoothed strains.

In particular, we compute the equivalent displacements by:

$$\hat{\delta}_{1_T} = L_1 \left\langle \overline{\widetilde{\mathrm{E}}}_{11} \right\rangle \,, \tag{5.22}$$

$$\hat{\delta}_{1_C} = L_1 \left\langle -\overline{\widetilde{\mathrm{E}}}_{11} \right\rangle \,, \tag{5.23}$$

$$\hat{\delta}_{2_T} = L_2 \sqrt{\left\langle \overline{\widetilde{\mathrm{E}}}_{22} \right\rangle^2 + \left(\overline{\widetilde{\mathrm{E}}}_{12} \right)^2} \,, \tag{5.24}$$

$$\hat{\delta}_{2_C} = L_2 \sqrt{\left\langle -\overline{\widetilde{\mathrm{E}}}_{22} \right\rangle^2 + \left(\overline{\widetilde{\mathrm{E}}}_{12} \right)^2} \,, \tag{5.25}$$

where $\overline{\widetilde{\mathrm{E}}}_{\alpha\beta}$ are dimensionless components of the *smoothed* strain $\widetilde{\mathbf{E}}^\flat$ with respect to an orthonormal basis $\{\overline{\mathbf{e}}^\alpha\}$ for the co-tangent space of the lamina midsurface, in which $\overline{\mathbf{e}}^1$ is parallel to fiber direction in the lamina (cf. [14, Section 2.1]). Angle brackets $\langle \cdot \rangle$ are Macaulay brackets, isolating the non-negative part of their argument. The coefficients $\{L_\alpha\}$ are the length scales used to convert from strains to equivalent displacements; in [14], we assumed $L_1 = L_2$ and computed these length scales from the Jacobian of the mapping from a standard element to physical space, to limit the effects of mesh-dependent damage localization. In the present work, we compute $\{L_\alpha\}$ from $\mathbf{c}$. First, we introduce the assumption that $\mathbf{c}^\flat$ is diagonal in the basis $\{\overline{\mathbf{e}}^\alpha\}$, then set:

$$L_\alpha = \sqrt{\overline{c}_{\underline{\alpha\alpha}}} \,, \tag{5.26}$$

where the bar again indicates that components are in the fiber-aligned orthonormal basis, and the repeated index is underlined to indicate that no summation takes place in this instance. As we do not presently have a method for estimating appropriate anisotropy of $\mathbf{c}$, we assume, for the remainder of this paper, that:

$$c^\alpha{}_\beta = c\delta^\alpha{}_\beta \,, \tag{5.27}$$

where the scalar parameter c has dimensions of area. The remainder of the shell structure mechanics, laminar damage modeling, and interlaminar cohesive coupling from [14] is unchanged, and we refer the reader to the cited reference for additional details.

Remark 2. The introduction of a new model parameter, c, may seem unappealing to practitioners working with local models, who have no established protocol for calibrating a strain-smoothing length scale. However, mesh-dependence of solutions to local models means that the number, positions, and connectivity of nodes in a finite element mesh must all be considered free parameters. This makes calibration with specific geometries difficult, and renders intractable the end goal of predicting damage in new scenarios, for which experimental data is not available.

5.4 Isogeometric discretization of strain smoothing

To apply the smoothed-strain damage model of Sections 5.2–5.3 in computer simulations, the numerical framework of [14] is extended to solve for an approximate solution to (5.16) at each time (or load) step of a simulation. The smoothed strain is nonlinearly coupled to the mechanics and damage evolution of the structure. However, the problem of solving for $\widetilde{\varepsilon}$ given a fixed structural deformation is linear, with only the source term depending on the deformation. The relative straightforwardness of the fixed-displacement strain smoothing problem leads us to adopt a staggered approach to solving the fully-coupled problem, in which we alternate between solving structural mechanics and strain smoothing subproblems, holding the solution to the other fixed in each, until arriving at a fixed point. The precise algorithm for applying this staggered solution procedure in conjunction with the generalized-α time integration used in [14] is essentially identical to that given for phase field fracture analysis in [20, Section 3.3.2], with the strain smoothing subproblem taking the place of the phase field subproblem.

The discretization of the structural mechanics subproblem is as specified in [14] and references therein. We discretize the new strain smoothing subproblem (5.16) using a standard Bubnov–Galerkin approach, i.e., posing (5.16) over a finite-dimensional subspace $\mathcal{V}_E^h$ of $\mathcal{V}_E$. For convenience, each of the three unique components of the symmetric tensor $\widetilde{\varepsilon}$ (as expressed in the *curvilinear* basis $\{\mathbf{G}^\alpha\}$) is considered to be in the same finite-dimensional scalar-valued space as the components of shell structure displacement. Test and trial spaces for the second-order strain smoothing subproblem need only be $H^1(\Gamma_0)$-conforming, but we use C^1 isogeometric spline functions, due to the more stringent constraints on the displacement spaces, from the higher-order bending terms of the Kirchhoff–Love shell formulation. In particular, we use B-spline and NURBS function spaces, and assume that the curvilinear coordinates $\{\xi^\alpha\}$ correspond to the parameter spaces of the spline patches.

Remark 3. The discretization of curvilinear (rather than Cartesian) tensor components is in contrast to some prior finite element discretizations of surface differential operators acting on unknown fields of nonzero rank, e.g., [94, 44, 60]. The approaches of the cited references introduce redundant degrees of freedom by seeking higher-dimensional tensor-valued solutions, and require extra mechanisms to enforce solution tangency, albeit with various advantages discussed in [60]. Our approach in the present work is analogous in some ways to the treatment of isogeometric discrete differential forms in [23, 22], where the coupled unknown scalar fields are associated with parametric rather than spatial directions. In the same way that divergence-conforming B-spline discretizations of incompressible flows fail to satisfy exact global momentum balance [40, Section 9.7], our smoothed strain field may fail certain "patch tests" such as exactly reproducing spatially-uniform strains. However, the error converges under refinement and is likely negligible for approximation spaces sufficient to represent accurate displacement solutions to strain-softening damage models. Further, $\mathbf{E}^h = \mathbf{0}$ still implies $\widetilde{\mathbf{E}}^h = \mathbf{0}$, so rigid-body motions cannot result in spurious damage.

The only terms in the formulation (5.16) that are not readily available within prior frameworks for isogeometric analysis of Kirchhoff–Love shell structures (as detailed in, e.g., [68, 69, 66]) are the Christoffel symbols, $\Gamma^{\alpha}_{\beta\gamma}$. These may be computed from the metric tensor $\mathbf{G}$ using the formula [74, Lemma 3.29, Chapter 1]:

$$\Gamma^{\alpha}_{\delta\gamma} = \frac{1}{2} G^{\alpha\beta} \left(G_{\gamma\beta,\delta} + G_{\delta\beta,\gamma} - G_{\delta\gamma,\beta} \right) \ . \tag{5.28}$$

The necessary partial derivatives of $\mathbf{G}$ can be obtained via:

$$G_{\alpha\beta,\gamma} = \left(\mathbf{X}_{,\alpha} \cdot \mathbf{X}_{,\beta} \right)_{,\gamma} = \left(X^D{}_{,\alpha} \delta_{DE} X^E{}_{,\beta} \right)_{,\gamma} = X^D{}_{,\alpha\gamma} \delta_{DE} X^E{}_{,\beta} + X^D{}_{,\alpha} \delta_{DE} X^E{}_{,\beta\gamma} \ , \tag{5.29}$$

where $\mathbf{X} : \mathbb{R}^2 \to \mathbb{R}^3$ maps from coordinates $\{\xi^\alpha\}$ to embeddings of the corresponding points of Γ_0 into a Cartesian coordinate representation of 3D space. (The Kronecker delta δ_{AB} gives the components of the 3D metric tensor in Cartesian coordinates.) In standard isogeometric discretizations, position components X^A are linear combinations of scalar basis functions defined on the parameter space, and thus the derivatives $X^A{}_{,\alpha}$ and $X^A{}_{,\alpha\beta}$ are straightforwardly constructed as linear combinations of derivatives of shape functions.

5.5 Numerical results

Reinstatement of mesh objectivity is the primary objective of the Gradient-Enhanced method. Results presented in the literature (i.e., see [82, 53, 35]) proved that it is possible to obtain mesh-independent damage predictions by adopting the Gradient-Enhanced strain regularization technique. However, to the authors knowledge, the accuracy of the Gradient-Enhanced method has not been investigated yet for applications on severely distorted meshes.

The formulation presented in Sections 5.2–5.3 is specifically developed for Isogeometric applications, in which mesh regularity is strictly connected to the NURBS representation of geometries. Therefore, in this section, we show applications of the Gradient-Enhanced strain-smoothing method in order to verify the robustness of the proposed formulation in terms of sensitivity with respect to mesh distortion.

First, three benchmark problems are presented in order to assess convergence properties under *h*- and *k* refinements and to verify mesh objectivity with respect to damage prediction. The nonlocal strain regularization is then applied for impact simulations in combination with full multi-layer modeling approach. In the first example, the low velocity impact on a 24-plies flat laminate, presented in Section 4.4.2, is revisited and results obtained from local and nonlocal damage formulations are compared. The last example shows the application of the nonlocal damage theory for a low-velocity impact on a reinforced composite panel.

It is worth to mention that all the graphics results are obtained by projecting the solution, computed at NURBS control points, on a lower order linear polynomial space. This allows us to use traditional visualization tools developed for Finite Element applications.

5.5.1 Convergence of the Gradient-Enhanced method under *h*-refinement

The method of manufactured solution is applied in order to verify the accuracy of the proposed strain-smoothing method (5.5) under mesh *h*-refinement. In particular we employ the formulation (5.16) developed for Kirchhoff–Love shell elements under plane-stress assumption. The manufactured strain field $\widetilde{\mathbf{E}}$ is defined with respect to the global Cartesian basis $\{\bar{\mathbf{e}}_\alpha\}$ on the domain $\Gamma_0 = (-1,1)^2$, and its components are chosen *ad-hoc* such that the flux-free natural boundary condition (see, e.g., [82]) is identically satisfied anywhere on $\partial\Gamma_0$:

$$\widetilde{\mathbf{E}}^\sharp = \tilde{\bar{\varepsilon}}^{\alpha\beta}\, \bar{\mathbf{e}}_\alpha \otimes \bar{\mathbf{e}}_\beta = \cos\left(\pi X^1\right) \overline{m}^{\alpha\beta}\, \bar{\mathbf{e}}_\alpha \otimes \bar{\mathbf{e}}_\beta \,, \tag{5.30}$$

where X^1 is the coordinate associated with the global basis $\bar{\mathbf{e}}_1$, while $\mathbf{m}$ is a constant second order tensor with $\overline{m}^{11} = 1$, $\overline{m}^{22} = 3$ and $\overline{m}^{12} = \overline{m}^{12} = 2$. It is worth noting that, since $\tilde{\bar{\varepsilon}}^{\alpha\beta}$ are defined with respect to a Cartesian basis, their values are unaffected by raising and lowering of indices. The components of the source term $\boldsymbol{\varepsilon}$ in (5.16) are straightforwardly computed in Cartesian coordinates from (5.4) and, thereafter, transformed into covariant component $\varepsilon_{\alpha\beta}$ for consistency with the equation (5.16). The components $c^\alpha{}_\beta$ of the smoothing tensor are set to $\delta^\alpha{}_\beta$.

Convergence test is performed using both regular and skewed discretization. In the first case, local curvilinear basis $\{\mathbf{G}^{\alpha}\}$ are constant and point-wise parallel to the global axes. In case of skewed mesh, the length and the orientation of the basis vary along the curvilinear parametric coordinates $\{\xi^{\alpha}\}$. The purpose of the test is to verify the convergence rate of the numerical solution $\widetilde{\mathbf{E}}^{h}$ as a result of mesh refinement. For the current test, we employ quadratic NURBS shape functions. The L_2 norm of the error $\|\widetilde{\mathbf{E}} - \widetilde{\mathbf{E}}^{h}\|$ is reported in Figure 5.1. It can be observed that the the error converges correctly as a cubic function of the characteristic element size $l_{\text{ele}} = 2\sqrt{\|\mathbf{G}_1 \otimes \mathbf{G}_2\|}$.

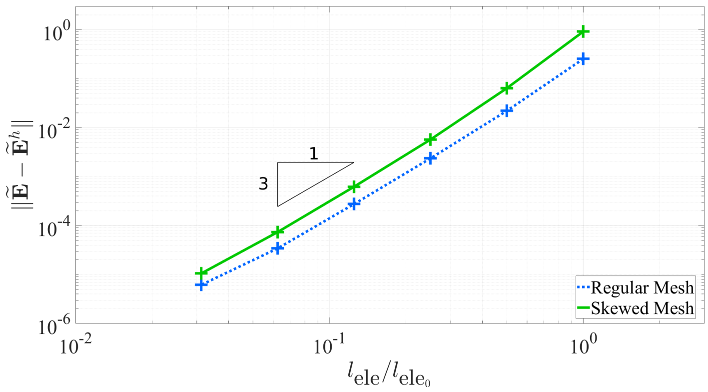

Figure 5.1: Convergence of Gradient-Enhanced method: Convergence rate, as a function of mesh size, for regular and skewed meshes.

A qualitative comparison of the numerical results obtained for different distorted meshes is shown in Figure 5.2. The mesh skew factor is computed for quadrilateral elements as SF = $\max\|\cos\alpha\|$, where α is the angle between the edges at the element center.

5.5.2 Uniaxial tensile test

The second benchmark simulates an uniaxial tensile test on a slender bar [82]. The purposes of this test are:

- To investigate damage localization using NURBS shape function of increasingly higher-order and higher inter-element continuity NURBS shape functions in combination with a local damage model;
- To verify that, if nonlocal regularization is employed, the numerical solution converges under mesh refinement.

The coupon, that is shown in Figure 5.3, measures 100 mm and 10 mm in the longitudinal and in the lateral direction, respectively. The bar has a constant thickness of 1 mm except for a

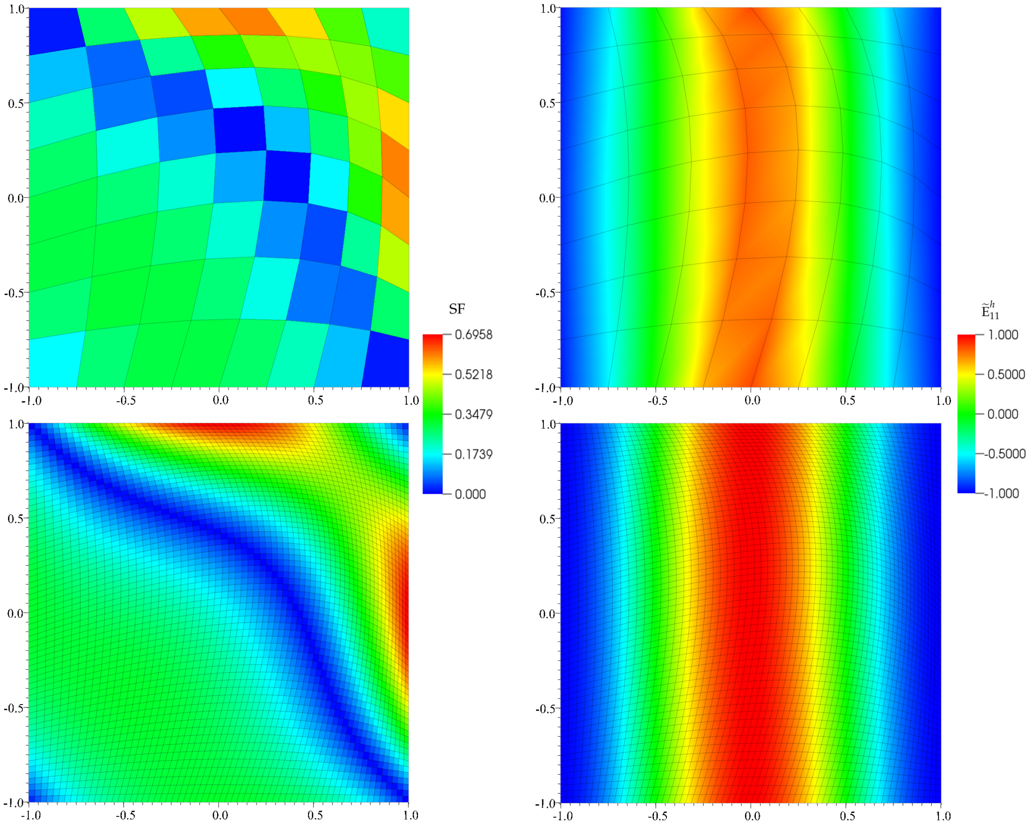

(a) (b)

Figure 5.2: Convergence test performed by using the manufactured solution method. Plot contours represent (a) the distribution of the skew factor of the mesh and (b) the $\widetilde{\mathrm{E}}^h_{11}$ component referred to the global Cartesian basis $\{\bar{\mathbf{e}}_\alpha\}$.

central section, which extends for a length of 10 mm, where the thickness is reduced to 0.9 mm. Clamped boundary condition is imposed on one short side of the bar, while uniform displacement is imposed on the opposite short side. The test is performed under displacement control boundary condition in order to ensure stability of the simulation during the softening damage process. The material is isotropic with a Young's modulus is E=20 GPa. Poisson's ratio is set to ν=0 in to simulate a true uniaxial stress along the bar.

The isotropic damage model is based on a residual-stiffness constitutive law:

$$\mathbf{S} = (1 - d_{\text{iso}})\,\mathbf{C} : \mathbf{E}\,, \tag{5.31}$$

where $\mathbf{S}$ denotes the second Piola–Kirchhoff stress tensor, d_{iso} a scalar isotropic damage variable and $\mathbf{C}$ the fourth-order tensor of elastic moduli. A bilinear damage law is introduced in order to

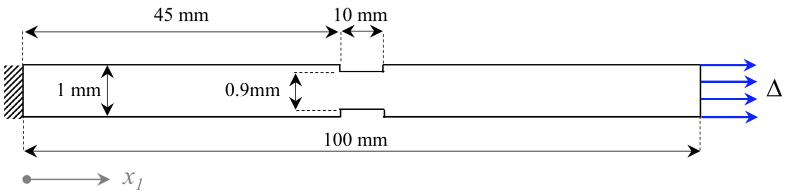

Figure 5.3: Schematic depiction of the uniaxial tensile test simulation. Section view in the longitudinal direction.

compute the isotropic damage variable d_{iso} as a function of the parameter κ:

$$d_{\text{iso}}(\kappa) = \begin{cases} 0 & \text{if } \kappa \leq \kappa^0 \quad , \\ \dfrac{\kappa^F}{\kappa}\dfrac{\kappa - \kappa^0}{\kappa^F - \kappa^0} & \text{if } \kappa^0 \leq \kappa \leq \kappa^F \quad , \\ 1 & \text{if } \kappa > \kappa^F \quad , \end{cases} \tag{5.32}$$

where $\kappa^0 = 1.0^{-4}$ and $\kappa^F = 1.25 \times 1.0^{-2}$. It is worth to mention that, as opposed to the intralaminar damage model presented in [14], in this isotropic damage model the damage-initiation criterion is based solely on the value of the parameter κ compared to κ^0.

Damage localization under *k*-refinement

Isogeometric analysis introduced the concept of *k*-refinement (i.e., see [32]) which allows to *simultaneously* elevate NURBS order as well as the order of inter-knot continuity. Three different discretization are considered for the coupon shown in Figure 5.3: (a) 160 linear C^0 elements; (b) 160 quadratic C^1 elements; (c) 160 cubic C^2 elements. Element size in the longitudinal direction is constant and equal to 0.625 mm. Discretization in the lateral direction is limited to one element. It is worth to mention that linear C^0 NURBS correspond to linear Lagrange polynomials, which are typically adopted as shape functions in the framework of Finite Element analysis.

For this simulation, the parameter κ in (5.32) is defined equal to the local (i.e., non-smooth) axial component of strain $\overline{\mathrm{E}}_1$. No length scale is used in the damage law (5.32) and κ^0 and κ^F represent, respectively, the limit strains at which permanent damage initiates and the material is fully damaged.

Force-displacement curves from numerical simulations are shown in Figure 5.4. Results obtained using linear C^0 NURBS shape functions clearly indicate that bar exhibits almost instantaneous loss of stiffness once damage initiation occurs. This paradoxical result stems from the discontinuous nature of the strain field computed from linear C^0 shape functions, which is discontinuous across the elements. Therefore, strain localizes in the element where damage initiation criterion is initially met, while the remainder of the bar unload elastically. Similar results are reported in [72] for a local damage theory in which a length scale is omitted in the definition of the damage law. In this case, damage localization instability leads, for sufficiently refined meshes and linear C^0 shape functions, to failure without energy dissipation. This results clearly contradicts the principles for verification and validation articulated by Babuška and Oden [7].

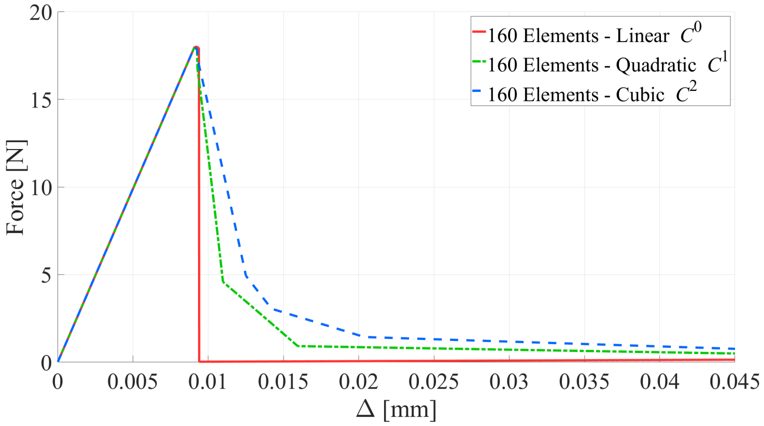

Figure 5.4: Uniaxial tensile test: Local damage model. Force-displacement curves obtained from simulation performed on 160 elements-mesh with progressively higher order and continuity NURBS shape functions.

The problem of damage localization is partially alleviated by employing higher-order continuity shape functions, as shown in Figure 5.5. Because of the higher-order continuity of the strain field, axial strain does not localize in the single element where damage initiates. Instead, axial strain localize over the length corresponding to the support region of those shape functions which also have support in the element where damage is initially detected.

It is worth noting that, if local effects related to the discontinuity of the thickness are neglected, the nominal axial strain is constant in the weak section of the bar. Therefore, damage initiation may theoretically occur anywhere in the region $x \in [45, 55]$ mm. This is the case simulated using linear C^0 NURBS shape functions, which are able to capture the sharp discontinuity of the strain field. However, if higher-order continuous shape functions are employed, damage initiation is triggered in the proximity of the thickness discontinuity due to numerical fluctuations of strain typically associated with Gibbs phenomenon.

Remark 4. In the framework of IGA, the support of a p-th order NURBS shape function spans over p+1 knot intervals, or elements. Therefore, the support of linear (p=1) NURBS extents for two elements, the support of quadratic (p=2) NURBS extents for three elements and the support of cubic (p=3) NURBS extents for four elements. Impact simulations presented in the following section, as

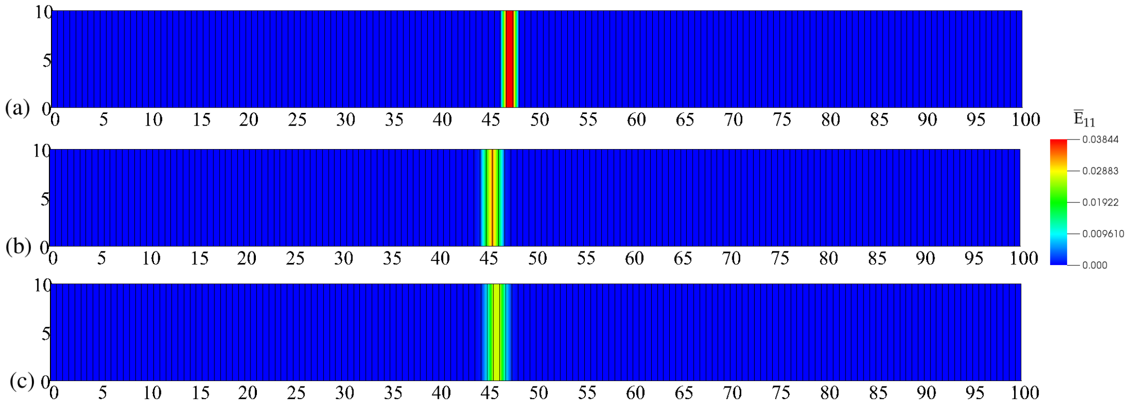

Figure 5.5: Uniaxial tensile test: Local damage model. Simulation results obtained using a discretization of 160 (a) linear C^0, (b) quadratic C^1 and (c) cubic C^2 elements. Contour plot of the local axial strain component $\overline{\mathrm{E}}_{11}$. Results obtained for an applied displacement Δ = 0.045 mm. View from top.

well as results published in [14, 84, 85], require to use, at least, quadratic C^1 shape functions due to the presence of curvature-change strain tensor. Curvature effects are neglected for the uniaxial tensile test.

Convergence using the Gradient-Enhanced nonlocal model

The Gradient-Enhanced method is therefore employed to regularize the strain field, which is used to compute the isotropic damage variable. For this purpose, the parameter κ in (5.32) is defined equal to the smooth axial component of strain $\overline{\overline{\mathrm{E}}}_1$. Convergence is investigated by using four progressively-refined meshes comprised of 40, 80, 160 and 320 elements uniformly distributed in the longitudinal direction. Quadratic C^1 NURBS shape functions are employed, while the smoothing parameter c is set equal to 1 mm^2.

Force-displacement curves obtained from numerical simulations, see Figure 5.6, show that the solution quickly converges under h-refinement and the dissipated energy is independent with respect to mesh discretization.

Figure 5.7 shows the distribution of the istotropic damage variable d_{iso} as a function of the longitudinal coordinate. The simulation performed with a very coarse mesh fails to predict a symmetric distribution of the damage variable. However, results obtained from progressively refined meshes show that the damage distribution converges to a symmetrical solution.

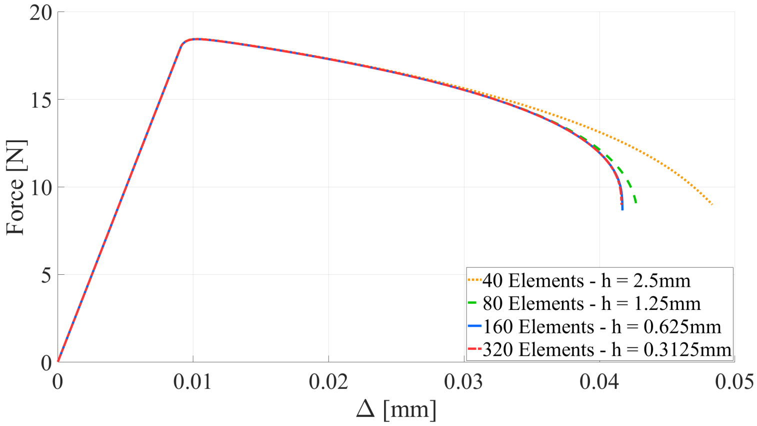

Figure 5.6: Uniaxial tensile test: Gradient-Enhanced nonlocal regularization. Force-displacement curves obtained by using quadratic C^1 NURBS shape functions, progressively refined discretization and a smoothing parameter c = 1 mm^2.

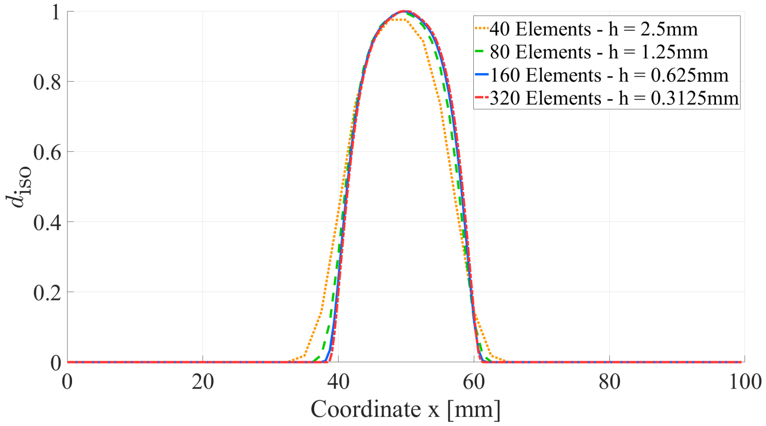

Figure 5.7: Uniaxial tensile test: Gradient-Enhanced nonlocal regularization. Distribution of the isotropic damage variable obtained by using quadratic C^1 NURBS shape functions, progressively refined discretization and a smoothing parameter c = 1 mm^2. Results obtained for an applied displacement Δ = 0.04 mm.

5.5.3 Three-point bending test

A three-point bending test [35] is considered. The dimension of the beam, as shown in Figure 5.10, are 2000 mm and 300 mm in the longitudinal and lateral direction, respectively. The thickness is constant and equal to 50 mm. Simply supported boundary conditions are imposed on the lower corners, while prescribed-displacement boundary conditions are imposed on the upper edge. The material is assumed to be linear isotropic with a Young's modulus $E = 20$ GPa and a Poisson's ratio $\nu = 0.2$. The Poisson's ratio is assumed to remain constant during the damage process. The isotropic softening constitutive law is defined in (5.31). For this simulation, the

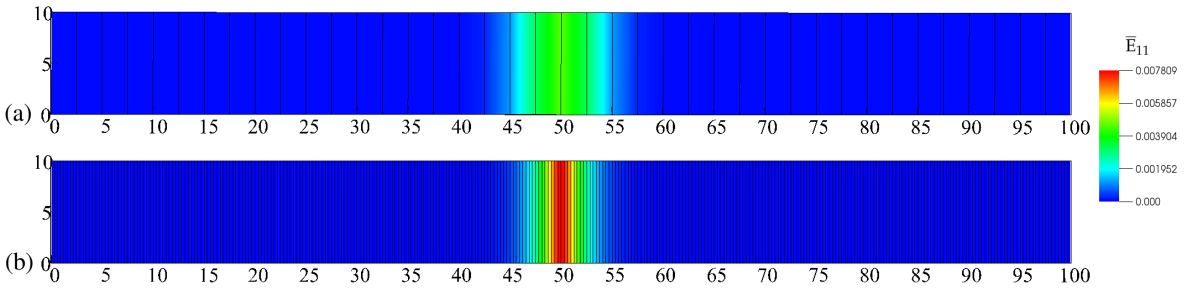

Figure 5.8: Uniaxial tensile test: Gradient-Enhanced nonlocal regularization. Contour plot of the local axial strain component $\overline{E}_{11}$ obtained by using quadratic C^1 NURBS shape functions, smoothing parameter c = 1 mm^2, (a) 40 and (320) elements. Results obtained for an applied displacement Δ = 0.04 mm. View from top.

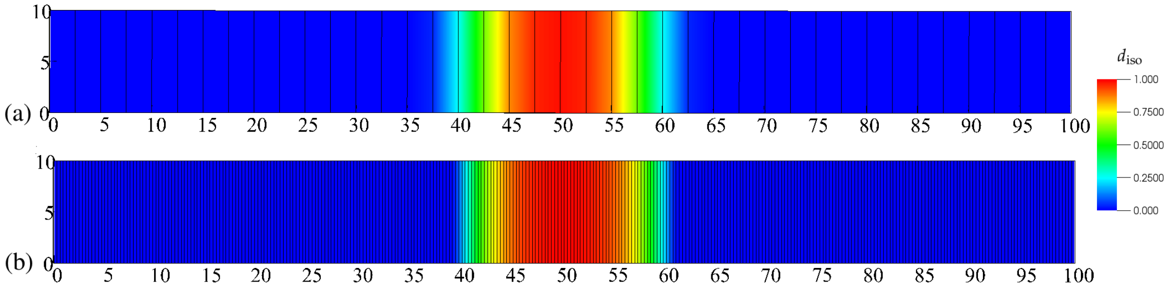

Figure 5.9: Uniaxial tensile test: Gradient-Enhanced nonlocal regularization. Contour plot of the isotropic damage variable d_{iso} obtained by using quadratic C^1 NURBS shape functions, smoothing parameter c = 1 mm^2, (a) 40 and (320) elements. Results obtained for an applied displacement Δ = 0.04 mm. View from top.

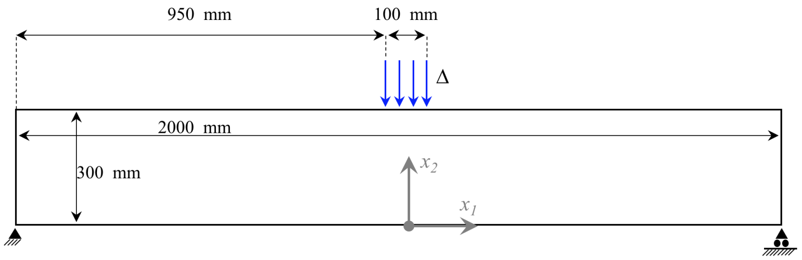

Figure 5.10: Schematic depiction of the three-point bending test simulation.

isotropic damage variable d_{iso} is computed using an exponential damage law that is a function of a history damage variable $\hat{\delta}$:

$$d_{\text{iso}}(\hat{\delta}) = \begin{cases} 0 & \text{if } \hat{\delta} \leq \hat{\delta}^0 \quad , \\ 1 - \dfrac{\hat{\delta}}{\hat{\delta}^0} \left\{ (1-\alpha) + \alpha \exp\left[\beta\left(\hat{\delta}^0 - \hat{\delta}\right)\right] \right\} & \text{if } \hat{\delta} > \hat{\delta}^0 \quad , \end{cases} \tag{5.33}$$

where α and β are material parameters, while $\hat{\delta}^0$ a critical value of the history damage variable at which damage is initiated. For this simulation, the onset of permanent damage is determined by $\hat{\delta}^0 = 10^{-4}$, while material parameters are set to $\alpha = 0.99$ and $\beta = 500$. Equations (5.31) and (5.33) are complemented by a damage loading function:

$$f\left(\eta, \hat{\delta}\right) = \eta - \hat{\delta} \, , \tag{5.34}$$

where η denotes an equivalent strain measure. The damage loading function f and the rate of the history damage variable $\dot{\hat{\delta}}$ satisfy the Kuhn–Tucker conditions which ensures non-reversibility of damage:

$$f\dot{\hat{\delta}} = 0 \, , \; f \leq 0 \, , \; \dot{\hat{\delta}} \geq 0 \, , \tag{5.35}$$

while the equivalent strain measure η used for the damage loading function $f\left(\eta, \hat{\delta}\right)$ is:

$$\eta\left(\overline{\widetilde{\mathbf{E}}}\right) = \sqrt{\left\langle \overline{\widetilde{\mathrm{E}}}_1 \right\rangle^2 + \left\langle \overline{\widetilde{\mathrm{E}}}_2 \right\rangle^2} \, , \tag{5.36}$$

where $\overline{\widetilde{\mathrm{E}}}_1$ and $\overline{\widetilde{\mathrm{E}}}_2$ are the in-plane principal strains expressed in the global orthogonal coordinate system. Macaulay brackets allow for damage growth only for tensile strains.

This three-point bending test is simulated using three different meshes, shown in Figure 5.11 and two values of the Gradient-Enhanced scalar parameter c, which is defined in Equation (5.27). The baseline model uses a regular mesh with rectangular elements whose edges are oriented parallel to global axes. Progressively distorted mesh are then considered to verify the robustness of the Gradient-Enhanced method. Simulations are performed by setting the parameter c = 50 mm^2 and c = 200 mm^2. Distribution of the damage variable along the beam for different meshes and smoothing parameter are shown in Figure 5.12.

The length scale of the damaged area is proportional to the square root of c as defined in Equation (5.26), thus the damaged area for c = 200 mm^2 is expected to be twice as wide as the damaged area for c = 50 mm^2. Results shown in Figure 5.12 are in good agreement with theoretical prediction. It can be observed that differences in the distribution of the damage variable, computed using different meshes, is negligible.

Figure 5.13 shows force-displacement curves from numerical simulations. No significant discrepancies can be observed between the baseline and the skewed symmetrical model. Discrepancy in the maximum predicted force can be observed in simulation performed using the skewed asymmetrical mesh. Compared to the baseline simulation, the model over-predicts the peak force by 0.5%, for a smoothing parameter c = 50 mm^2, and by 3.1% for c = 200 mm^2. It can be inferred that the use of a severely distorted discretization results in the under-estimation of the

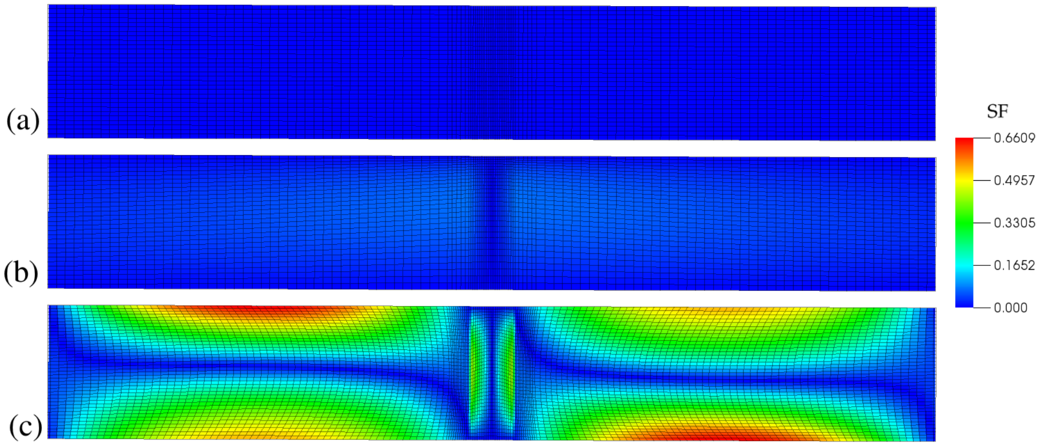

Figure 5.11: Three-point bending test: Meshes used for the simulation. Contour plot of the mesh skew factor for the (a) Regular, (b) Skewed symmetrical and (c) Skewed asymmetrical mesh.

damage. We hypothesize that the cause of this ill behavior is numerical and attributable to the solution of the nonlinear system of equation for each time-step. Small elements located in the area of large damage gradient, have a relative marginal contribution to the global residual. While the Newton-Raphson method iteratively minimizes the global residual, difficulties may arise in the minimization of the local residual since convergence criterion of the iterative nonlinear solver is related to the norm of the global residual. Therefore, small errors in highly-stressed elements can propagate and compromise the overall accuracy of the solution.

Sensitivity of the solution with respect to mesh orientation

The presence of Christoffel symbols in the Gradient-Enhanced formulation assumes relevance when the orientation of covariant basis vectors is not constant over the domain. The three-point bending test simulation is revisited using a simplified version of the Gradient-Enhanced method, in which all the terms associated with the Christoffel symbols in the definition of covariant differentiation (5.8) are neglected. This test allows to assess the sensitivity of the solution in connection to the derivatives of local curvilinear basis vectors with respect to global axis. For this purpose, two meshes are considered: A regular mesh and an asymmetrical skewed mesh, as shown in Figure 5.11 (a) and (c), respectively.

Figure 5.14 shows the comparison of force-displacement curves obtained using both the complete and the simplified Gradient-Enhanced formulation on two different meshes. In case of regular discretization, the local curvilinear coordinate system is aligned with the global Cartesian axes. Therefore, the Christoffel symbols are identically null and results coincide. However, significant discrepancies can be observed by comparing results obtained from simulations performed

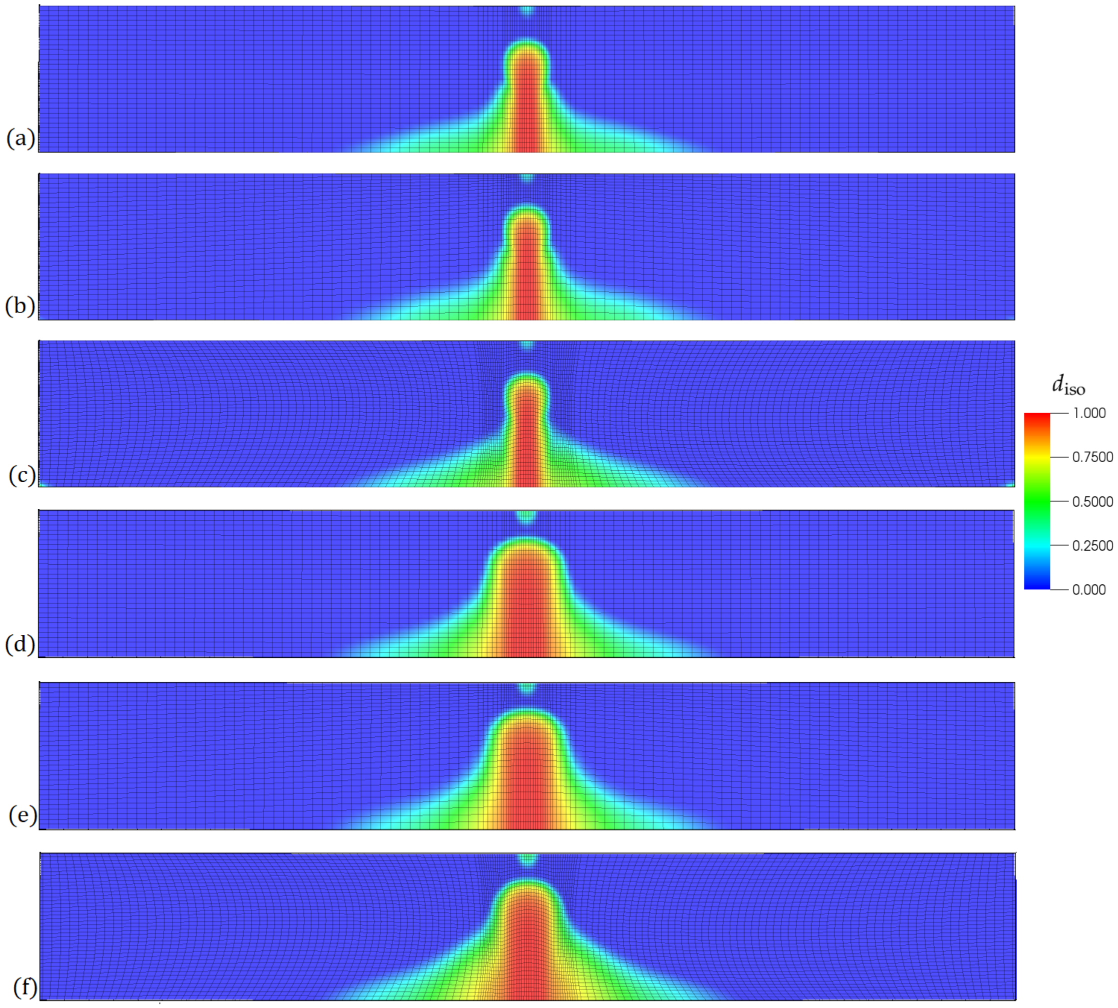

Figure 5.12: Three-point bending test: Gradient-Enhanced nonlocal regularization. Contour plots of isotropic damage variable d_{iso} for three different discretization: (a,d) Regular mesh, (b,e) Skewed symmetrical mesh and (c,f) Skewed asymmetrical mesh. Results (a), (b) and (c) are obtained for a prescribed displacement $\Delta = 0.65$ mm and a parameter $c = 50$ mm^2. Results (d), (e) and (f) are obtained for a prescribed displacement $\Delta = 1.0$ mm and a parameter $c = 200$ mm^2.

on the asymmetrical skewed mesh. Differences are related to the incompleteness of the simplified smoothing formulation, which introduces inaccuracies in the covariant differentiation of the strain field (5.8).

5.5.4 Low-velocity impact on a flat composite laminate

In this section the simulation of a low-velocity impact scenario on a flat composite laminate [85] is revisited in order to compare the effect of the nonlocal regularization technique. The rectangular plate measures 152.4 mm × 101.6 mm. Clamped boundary conditions are enforced on all the sides over a domain that extend for 12.7 mm from the edges. The actual test window

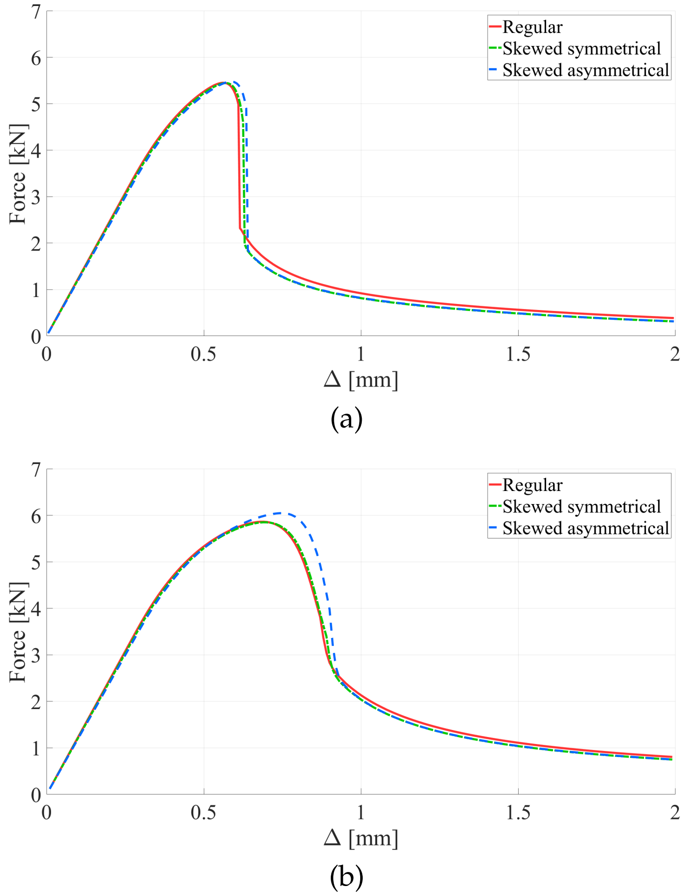

(a)

(b)

Figure 5.13: Three-point bending test: Force-displacement curves computed for three different discretization using the Gradient-Enhanced nonlocal regularization. Results obtained for a smoothing parameter (a) $c = 50$ mm^2 and (b) $c = 200$ mm^2.

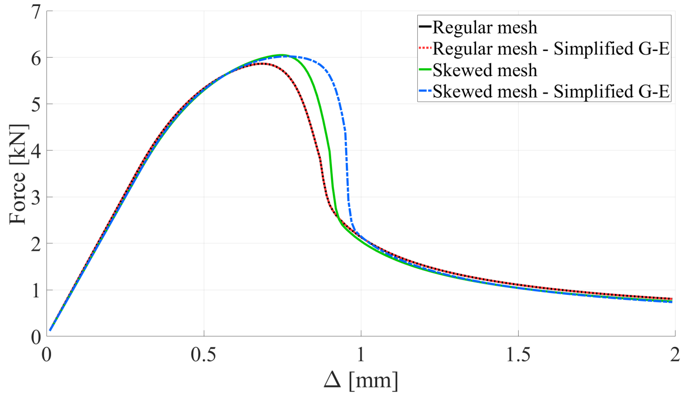

Figure 5.14: Three-point bending test: Force-displacement curves computed for two different discretization. Results obtained using the complete Gradient-Enhanced (G-E) formulation and the simplified counterpart in which all the terms associated with Christoffel symbols are neglected.

at the center of the coupon measures 127 mm × 76.2 mm. The plate is made of 24 unidirectional T800/3900-2 carbon/epoxy plies and the total thickness is 4.809 mm. Laminae are stacked according to the sequence $[0/45/90/\text{-}45]_{3s}$. Material and cohesive properties used for the simulation are reported in [85]. The impacting device has a hemispherical head with a radius of 25.4 mm and the impact energy is 25.1 J. No ply grouping [14] is employed and the plate is modeled ply-by-ply using 24 rectangular NURBS surfaces connected with 23 cohesive interfaces. The Gradient-Enhanced method for strain smoothing is enabled on all the NURBS surfaces. A penalty contact interface [14] is defined between the impactor and the first lamina on top of the plate.

For this simulation we use the same mesh discretization adopted in [85], in which the characteristic element size in the center of the plate is 1 mm, while it gradually increases to 1.5 mm closer to the clamped edges. The cohesive model imposes restriction on the mesh size. As discussed by Turon et al. [105], a fine mesh resolution is required in order to correctly capture the propagation of the delamination front. The local damage model [14] is replaced with the nonlocal version presented in Section 5.3. Isotropic smoothing is employed due to lack of theoretical evidences supporting the adoption of an anisotropic, or orthotropic, smoothing model. As discussed in Section 5.3 we tie the smoothing parameter c to the length-scale L_α of the damage model. Therefore, both the parameters are set equal to the characteristic element length. The model has a total number of 872,430 Degree Of Freedom (DOFs), equally distributed between structural displacements DOFs and smooth-strain DOFs, and the generalized–α method [31] is used to integrate in time the governing equations with a constant time-step of 2 μs.

The impact-force time history, obtained using the Gradient-Enhanced nonlocal regularization method, is shown in Figure 5.15. Results obtained from experimental test [85], as well as from a baseline Isogeometric model based on a local damage model, are also reported for comparison. Numerical result obtained using the Gradient-Enhanced regularization exhibits an excellent correlation with experimental data, as the peak force is over-predicted by 0.3% while no differences can be observed in the impact duration.

As discussed in our recent work [85], the global stability of the analysis performed using a local model was not affected by local instabilities associated with material strain-softening. Differences between local and nonlocal damage formulations stem from regularization of the strain field used to compute damage variables. The adoption of the Gradient-Enhanced regularization improves also the convergence rate of the nonlinear solver. The comparison of normalized convergence rates, computed at every integration time-step, is reported in Figure 5.16. It can be observed that the convergence rate is improved up to a factor of 10 during the stage of maximum damage formation and propagation. It is worth noting that these results were obtained using a *staggered*, or loosely-coupled, approach for the solution of structural and Gradient-Enhanced equations.

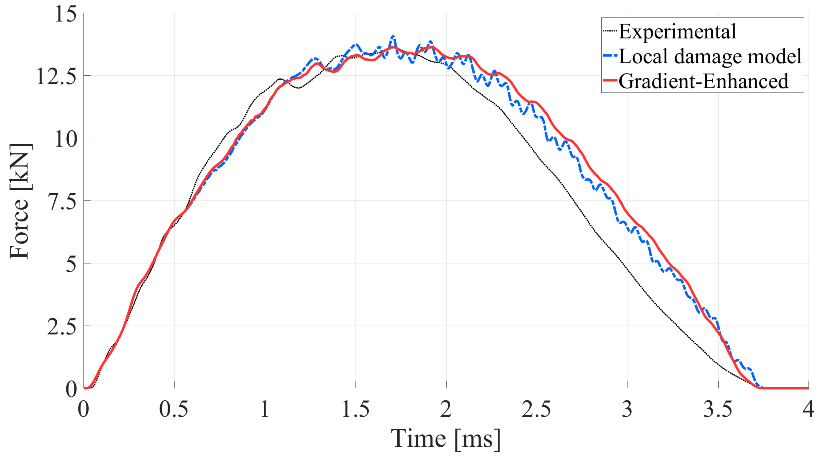

Figure 5.15: Impact on a flat laminate: Simulation result. Correlation of impact-force time history obtained for a 25.1 J impact simulation. Results obtained using the local damage model [85] are reported for comparison.

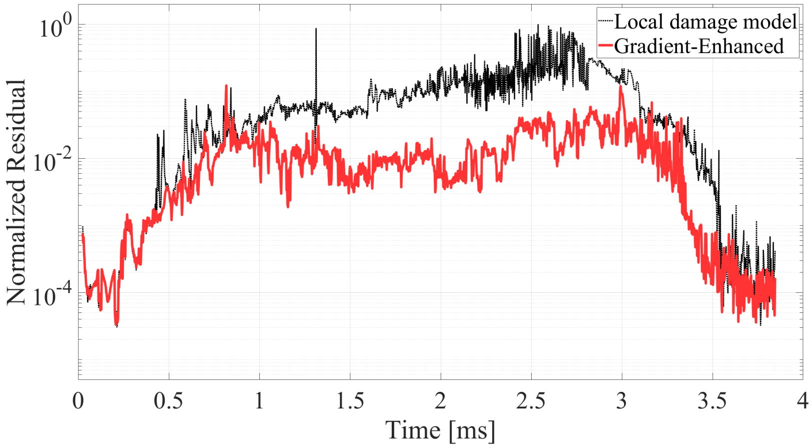

Figure 5.16: Impact on a flat laminate: Comparison of normalized residual obtained for a constant number of nonlinear Newton-Raphson iterations at every integration time-step. Simulation performed using local damage model is used as reference.

Ply-by-ply distribution of matrix damage is shown in Figure 5.17. Results obtained using a local damage model, which are reported for comparison purposes, exhibit spurious damage features. It can be observed that the nonlocal regularization re-establish the symmetry of damage patterns. Symmetrical distribution of predicted damage is in accordance with the symmetric setup of the numerical experiment.

It can also be observed from the interface-by-interface distribution of cohesive damage variable, shown in Figure 5.18, that the adoption of a strain-regularization technique for in-ply damage leads to a symmetric distribution of predicted delamination. While in-ply and interlaminar damage modes are not explicitly coupled through constitutive equations, the interaction of these damage modes is implicitly embedded in the damage mechanics of layered composites, which is correctly captured by the multi-layer analysis framework.

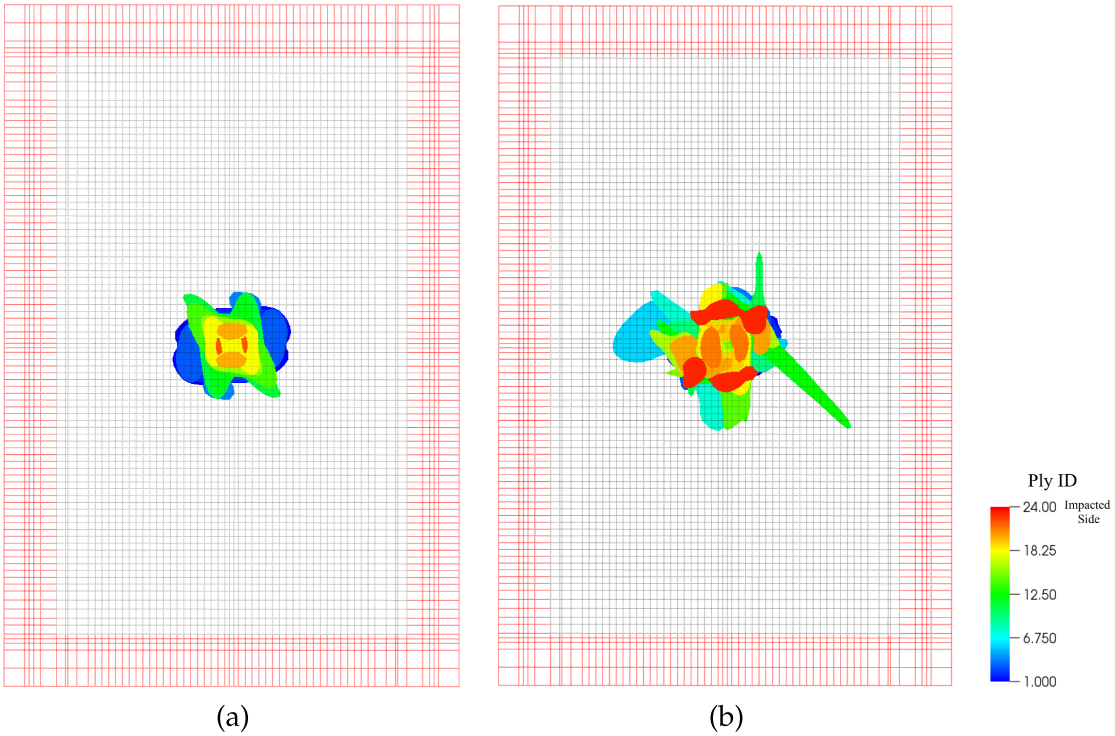

(a) (b)

Figure 5.17: Impact on a flat laminate: Simulation results. Ply-by-ply contour plots of matrix damage: colored areas represent, for each ply, the sub-domain where $d_2 \geq 0.5$. Comparison of results obtained using the (a) nonlocal and the (b) local damage model. Clamped boundary condition enforced on elements highlighted in red.

5.5.5 Low-velocity impact on a stiffener-reinforced composite panel

The last example proposed in this chapter is the simulation of a low-velocity impact on a stringer-reinforced composite panel. Numerical results obtained from a simplified model of the reinforced panel were originally reported in [85]. However, the original modeling approach made use of the ply-grouping technique which precludes to simulate delamination within groups of laminae. This often results in an over-prediction of impact forces. In this section, a full multi-layer model of the stringer-reinforced panel is considered.

The model is comprised of a flat skin panel, a hat-shaped stringer and a single lamina, oriented at 90°, placed between those parts. The panel, shown in Figure 4.5 and 4.6, measures 990.6 mm in the longitudinal direction of the stringers and 1308.1 mm in the lateral direction. The distance between the stringer centerlines is 260.35 mm. The impactor has a hemispherical head

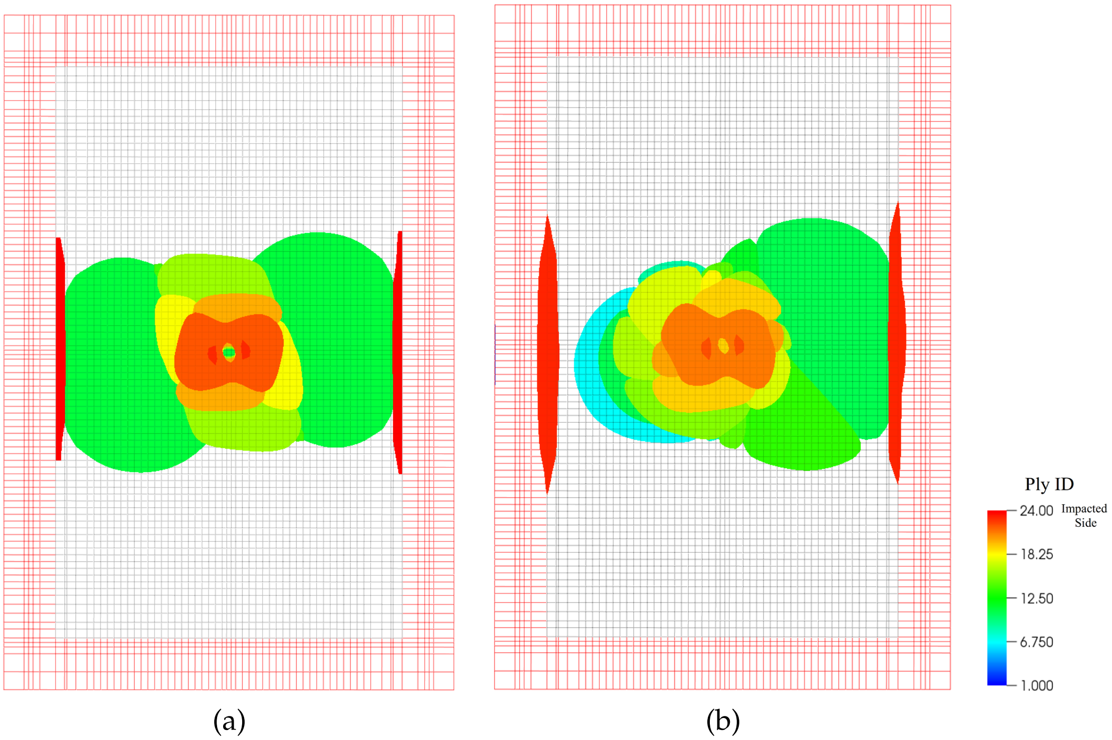

(a) (b)

Figure 5.18: Impact on a flat laminate: Simulation results. Interface-by-interface contour plots of inter-laminar damage: colored areas represent, for each interface, the sub-domain where $d_{\mathrm{coh}} \geq 0.5$. Comparison of results obtained using the (a) nonlocal and the (b) local damage model. Clamped boundary condition enforced on elements highlighted in red.

with a radius of 12.7 mm. The total impacting mass is 5.067 kg and the initial kinetic energy is 30 J. For this full multi-layer simulation, we consider the scenario of an impact occurring on the top of the stringer cap.

The baseline NURBS representation, as shown in Figure 5.19, is comprised of:

- 9 NURBS patches to represent the stringer;
- 5 NURBS patches to represent the skin;
- 3 NURBS patches to represent the single 90° ply;
- 1 NURBS patch to represent the impactor.

Bending strips are employed to connect NURBS patches that belongs to the same lamina. The bending strip technique (i.e., see [67]) was developed for IGA purposes, in combination with the thin-shell element model, in order to transfer bending moment across the boundaries of NURBS patches.

Starting from the baseline geometry, the multi-layer model is constructed using the commercial CAD software Rhinoceros3D [76] by off-setting NURBS surfaces. The lamination sequence for

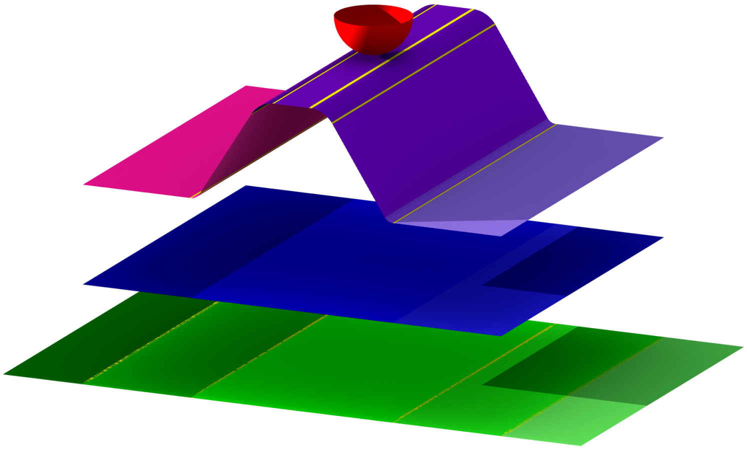

Figure 5.19: Impact on a reinforced panel: Baseline representation of the stringer-reinforced panel. Colored patches identify (green) skin, (blue) extra 90° ply, (purple) stringer and (red) impactor. Yellow narrows bands represent bending strips used to connect separate NURBS patches that belong to the same part.

skin and stringer is $[45/\text{-}45/0/45/90/\text{-}45/0/90]_s$. By taking advantage of the symmetric lamination sequence, the skin and the stringer are both represented by means of 15 distinct layers of NURBS patches. Considering the extra lamina, the complete multi-layer model is comprised of:

- 213 NURBS surfaces to represent skin, stringer and extra 90° ply;
- 182 Bending strips.

A total number of 201 zero-thickness cohesive interfaces are employed to connect laminae of individual parts, as well as for connecting the skin to the 90° ply and the 90° ply to the stringer. Material and cohesive properties used for the analysis are reported in Table 4.1 and Table 4.2, respectively. Clamped boundary conditions are only imposed on the long sides of the panel over a domain that extends for 2.5 mm from the edges. The characteristic element size in the impact area is 1.2 mm. The multi-layer model, shown in Figure 5.20 has a total number of 2,475,726 DOFs, equally distributed between structural displacements and smooth-strain.

Damage predictions for the low-velocity impact case are reported in Figure 5.21 and Figure 5.22. These figures show contour plots of maximum matrix and interlaminar damage obtained from the impact simulation. It can be observed that the damage distribution obtained using the Gradient-Enhanced damage model is continuous across NURBS patches, where displacement field is only C^0 continuous. This stem from the definition of the regularized strain as an independent unknown field. As such, C^0 continuity of the smooth strain is strictly enforced between NURBS patches by merging the corresponding and coincident degrees of freedom on connected patches.

Experimental results for the impact-test setup illustrated in this section are not available

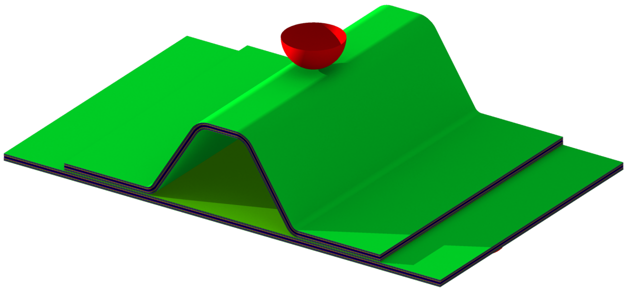

Figure 5.20: Impact on a reinforced panel: Multi-layer representation of the experimental setup for the impact simulation.

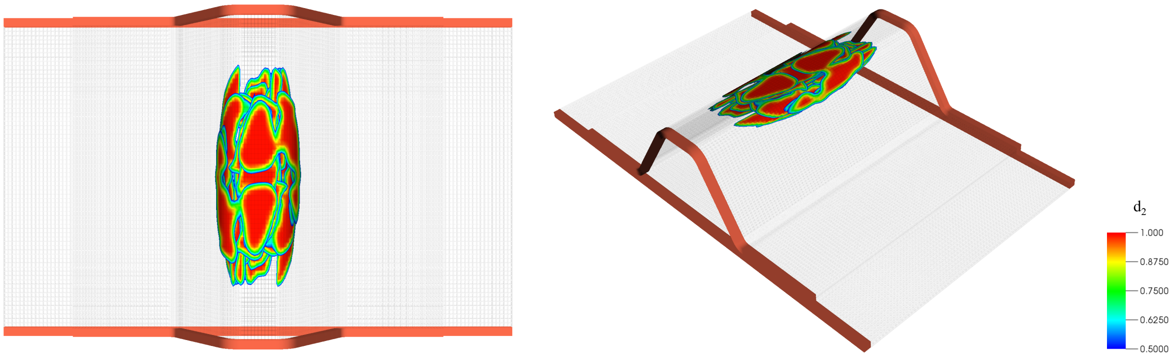

(a) (b)

Figure 5.21: Impact on a reinforced panel: Simulation results. ply-by-ply contour plot of matrix damage variable d_2 obtained using nonlocal damage model. Clamped boundary condition enforced on elements highlighted in red.

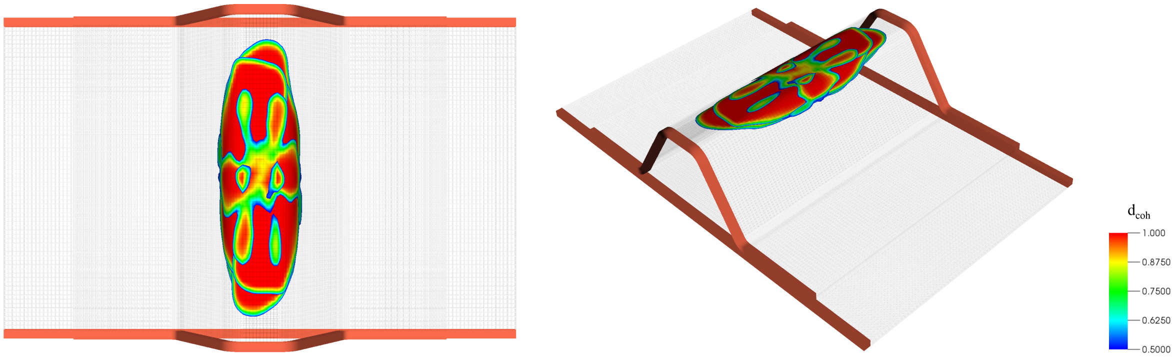

(a) (b)

Figure 5.22: Impact on a reinforced panel: Simulation results. Interface-by-interface contour plot of cohesive damage variable d_{coh} obtained using nonlocal damage model. Clamped boundary condition enforced on elements highlighted in red.

at the time this dissertation is drafted. Correlation of impact forces and damage profiles will be presented in future works.

5.6 Acknowledgments

Chapter 5 is, in full, an edited copy of material included in the manuscript in preparation: *"Gradient-enhanced damage modeling in Kirchhoff–Love shells: Application to isogeometric analysis of composite laminates"*. This manuscript is in preparation and is co-authored by *Marco S. Pigazzini, David Kamensky, Dennis A. P. van Iersel, Joris J.C. Remmers, and Yuri Bazilevs*. The author of this dissertation *(Marco S. Pigazzini)* is the primary investigator and author of this paper.

6 Conclusions and future directions

This dissertation introduces a comprehensive Isogeometric numerical framework for modeling progressive damage in composite laminates. The framework is based on a multi-layer modeling approach, in which each lamina is modeled as a Kirchhoff–Love shell discretized with NURBS surfaces. Multiple shell layers interact via novel zero-thickness cohesive interfaces, which allow representation of transverse shear compliance at the laminate level, and modeling of interlaminar damage and delamination. Continuum Damage Mechanics is used to model intralaminar damage by progressively degrading the elastic properties of the material. The Gradient-Enhanced nonlocal regularization is introduced to re-establish mesh objectivity and to minimize instabilities associated with strain-softening damage models.

Following a comprehensive state-of-the-art review of numerical methods for progressive damage simulations in composite materials, this dissertation explores new modeling techniques enabled by the introduction of the Isogeometric Analysis concept. The foundations of the novel analysis framework are presented and developed in Chapter 2. Starting from the definition of B-Spline and NURBS surfaces, a local curvilinear coordinate system and a metric tensor are defined on the basis of geometry parametrization. Then, the deformation gradient and the nonlinear Green-Lagrange strain tensor are derived. The structural model is based on the kinematic of the Kirchhoff–Love shell, which is computationally efficient and it is suitable to represent thin structural components, such as composite laminae, without exhibiting shear-locking effects. The presence of the curvature-change strain requires the use of shape functions that are, at least, C^1 continuous across the elements. Finally, the introduction of the Kirchhoff-St. Venant constitutive model enable the use of NURBS surfaces for structural analysis, whose governing equations are derived from the principle of virtual work.

The development of the multi-layer Isogeometric Analysis framework is extended in Chapter 3. This chapter summarizes our earlier work on Kirchhoff–Love shells in combination with interlaminar Continuum Damage Mechanics. A new zero-thickness cohesive-interface formulation suitable for Kirchhoff–Love shells is introduced in order to enable ply-by-ply representation of composite laminates. The formulation is validated using standard Mode I and Mode II delamination tests. The proposed formulation showed the ability of the multi-layer model to effectively represent transverse-shear behavior, and thus model thicker laminates. In addition, a thorough discussion of the effect of the cohesive-interface modeling parameters on the computational results is provided at the end of the chapter.

Applications of the Isogeometric Analysis framework are presented in Chapter 4. First, two low-velocity impact scenarios from the literature are used for validation purposes. Excellent agreement with experimental data was obtained for a lower-energy impact case. In case of higher-energy impact simulations, however, numerical results obtained with the IGA- and an in-house FE-based models exhibited some discrepancies with the experimental data. These are likely related to the lack of a plasticity model for the matrix phase and to the use of a symmetric tension-compression constitutive law. A new low-velocity impact simulation of a 24-ply flat coupon is also presented. Experimental test and non-destructive evaluation test [39] were performed by co-authors [85] at NASA Langley Research Center. Simulation results showed good agreement for the impact-force time history and for experimentally measured delamination at each one of the 23 ply interfaces. In addition, from the analysis of individual cohesive interfaces, we observed the expected correlation between matrix damage and delamination, despite them being treated as independent damage modes in the modeling framework. Applications of the multi-layer model to simulate low-velocity impact on a stiffened panel and a hard landing scenario for a novel UAV design are also shown. Results obtained for the low-velocity impact simulation, and, in particular, their comparison with experimental results, clearly demonstrate the accuracy and efficiency of the IGA-based approach to progressive damage modeling in laminated aerospace composite structures. The simulations also demonstrate the ease of going from geometry design to IGA simulations using existing geometry modeling tools.

In this dissertations it is shown that the proposed IGA-based formulation for progressive damage modeling in laminated composite structures, which is developed in the framework of multi-layer modeling using rotation-free Kirchhoff–Love shells, is an accurate and efficient alternative to the more traditional low-order solid-element FE approaches. In particular, the new IGA-based formulation is capable of reproducing impact-damage results using a fraction of the degrees of freedom required for traditional FE analysis. The reasons for this increased efficiency, besides the lack of rotational degrees of freedom in the discrete formulation, are as follows. Rotation-free Kirchhoff–Love shells, unlike solids or shear-deformable shells, do not suffer from transverse-shear locking in the limit of vanishing thickness. This property, in combination with higher-order accurate and smooth representation of the shell midsurface geometry and solution fields, allows one to adopt relatively coarse in-plane discretizations while maintaining good solution accuracy.

The use of NURBS and other type of spline functions allows for accurate and smooth representation of geometrically complex surfaces. NURBS permit a straightforward increase in the approximation order, as well as relatively effortless specification of the degree of continuity of the basis functions across element boundaries. It is precisely the higher-order continuity of these discretizations that enables the use of Kirchhoff–Love shell theory at the ply level, thus increasing computational efficiency and eliminating shear locking, such as seen in traditional FEM discretizations of thin structures, and which requires specialized numerical treatment.

As discussed in our recent work [85], the global stability of the analysis performed using a local damage model was not affected by local instabilities related to material strain-softening. However, further research is required in order to address damage localization issues, especially in the context of IGA-based Kirchhoff–Love shells.

For this purpose, the multi-layer Isogeometric Analysis framework for composite laminates is extended in order to incorporate a nonlocal damage model. The Gradient-Enhanced method is introduced in Chapter 5. This regularization technique aims to re-establish mesh objectivity by introducing a smooth *nonlocal* strain field that drives the Continuum Damage Mechanics model. The Gradient-Enhanced formulation presented in this dissertation was specifically developed for thin shell elements, whose kinematic assumptions require an *ad-hoc* treatment for strain smoothing. Several benchmark simulations are presented to prove the convergence and the accuracy of the nonlocal damage model under *h*- and *k*-refinements. Results show that the Gradient-Enhanced technique allows to re-establish mesh objectivity for damage prediction. Nonlocal regularization improves the stability of the analysis, which leads to a faster convergence rate for the solution of the nonlinear system of equations. This compensate for the additional computational cost required to compute the distribution of the smooth-strain field. It was shown that, due to the implicit coupling of matrix damage and delamination, regularization of in-ply damage leads to a regular distribution of interlaminar damage. Finally, the introduction of the smooth-strain as an additional unknown field, allows to obtain a continuous damage distribution across connected NURBS patches.

6.1 Future research directions

Prediction of post-impact residual strength of composite laminate is paramount, in particular for aerospace and advanced-automotive industries. The reduction of the nominal structural capacity is typically assessed by performing a quasi-static tensile or compression test on a component with a pre-existing damage state. Interlaminar and intralaminar damage can be intentionally introduced in pristine composite components by performing dynamic impact or quasi-static indentation test. In future research efforts we plan to carry out impact and, subsequently, Compression-After-Impact (CAI) analyses of larger-scale stiffened panels in order to assess the ability of the proposed IGA-based formulation to deliver accurate results in this setting.

Preliminary results showed that residual indentations on flat composite coupons are of primary importance for CAI test. Indeed, geometrical out-of-plane imperfections trigger local instabilities, such as lamina buckling, which represent the major failure mode under compressive loading condition. In the current implementation of the multi-layer model, plasticity is neglected. While typical reinforcement materials, such as carbon, exhibit an elastic behavior until failure, this is not the case for polymer matrices which may exhibit a plastic behavior. Accumulation of debris in micro-cracks, formed during the impact stage, is also considered another source of plasticity [21] since cracks cannot close during the unloading stage due to the presence of debris. For this purposes, we consider the introduction of a model for matrix plasticity (i.e., see [28]) in order to predict permanent deformation following impact simulations.

Another interesting development is the coupling of the efficient "equivalent single-layer representation" with the high-fidelity multi-layer modeling approach presented in this dissertation. While the ply-by-ply representation of composite laminates allows for accurate damage prediction, multi-layer modeling may be unfeasible, or extremely inefficient, for large scale components due to the amount of DOFs required to represent individual plies. For this reason, we envision the adoption of an hybrid modeling approach, in which multi-layer modeling is enabled only where delamination is expected to occur. The presence of matrix damage, which can be computed also if ply-grouping is enabled as discussed in Section 3.1.1, is an indicator that interlaminar damage has possibly occurred and a higher-fidelity representation of the laminate is locally required.

Appendix

A.1 Transformation of tensor components

In order to transform the components of a generic tensor $\mathbf{E}$ from the curvilinear basis $\mathbf{G}^\alpha, \mathbf{G}^\beta$ to a Cartesian basis $\overline{\mathbf{e}}_\alpha^{\mathrm{cur}}, \overline{\mathbf{e}}_\beta^{\mathrm{cur}}$, consider first the equivalence:

$$\mathbf{E} = \mathrm{E}_{\alpha\beta}\, \mathbf{G}^\alpha \otimes \mathbf{G}^\beta = \overline{\mathrm{E}}_{\alpha\beta}\, \overline{\mathbf{e}}_\alpha^{\mathrm{cur}} \otimes \overline{\mathbf{e}}_\beta^{\mathrm{cur}} \;, \tag{A.1}$$

where $\mathrm{E}_{\alpha\beta}$ are the covariant components of the tensor $\mathbf{E}$ associated with the contravariant basis $\mathbf{G}^\alpha, \mathbf{G}^\beta$, while $\overline{\mathrm{E}}_{\alpha\beta}$ are the Cartesian components of the tensor $\mathbf{E}$ associated with the Cartesian basis $\overline{\mathbf{e}}_\alpha^{\mathrm{cur}}, \overline{\mathbf{e}}_\beta^{\mathrm{cur}}$. The transformation is obtained by multiplying the left- and right-hand side of Equation (A.1) by $\overline{\mathbf{e}}_\kappa^{\mathrm{cur}}$ and $\overline{\mathbf{e}}_\gamma^{\mathrm{cur}}$:

$$\begin{aligned}
\mathrm{E}_{\alpha\beta}\overline{\mathbf{e}}_\kappa^{\mathrm{cur}} \left(\mathbf{G}^\alpha \otimes \mathbf{G}^\beta\right) \overline{\mathbf{e}}_\gamma^{\mathrm{cur}} &= \overline{\mathrm{E}}_{\alpha\beta}\overline{\mathbf{e}}_\kappa^{\mathrm{cur}} \left(\overline{\mathbf{e}}_\alpha^{\mathrm{cur}} \otimes \overline{\mathbf{e}}_\beta^{\mathrm{cur}}\right) \overline{\mathbf{e}}_\gamma^{\mathrm{cur}} \;, \\
\mathrm{E}_{\alpha\beta} \left(\overline{\mathbf{e}}_\kappa^{\mathrm{cur}} \cdot \mathbf{G}^\alpha\right) \left(\mathbf{G}^\beta \cdot \overline{\mathbf{e}}_\gamma^{\mathrm{cur}}\right) &= \overline{\mathrm{E}}_{\alpha\beta} \left(\overline{\mathbf{e}}_\kappa^{\mathrm{cur}} \cdot \overline{\mathbf{e}}_\alpha^{\mathrm{cur}}\right) \left(\overline{\mathbf{e}}_\beta^{\mathrm{cur}} \cdot \overline{\mathbf{e}}_\gamma^{\mathrm{cur}}\right) \;, \\
\mathrm{E}_{\alpha\beta} \left(\overline{\mathbf{e}}_\kappa^{\mathrm{cur}} \cdot \mathbf{G}^\alpha\right) \left(\mathbf{G}^\beta \cdot \overline{\mathbf{e}}_\gamma^{\mathrm{cur}}\right) &= \overline{\mathrm{E}}_{\alpha\beta}\delta_\kappa^\alpha \delta_\gamma^\beta \;, \\
\mathrm{E}_{\alpha\beta} \left(\overline{\mathbf{e}}_\kappa^{\mathrm{cur}} \cdot \mathbf{G}^\alpha\right) \left(\mathbf{G}^\beta \cdot \overline{\mathbf{e}}_\gamma^{\mathrm{cur}}\right) &= \overline{\mathrm{E}}_{\kappa\gamma} \;.
\end{aligned} \tag{A.2}$$

In Equation (A.2) we introduce the Kronecker Delta symbol in order to simplify the notation. Due to the orthogonality of the Cartesian basis $\overline{\mathbf{e}}_\beta^{\mathrm{cur}} \cdot \overline{\mathbf{e}}_\gamma^{\mathrm{cur}} = \delta_\gamma^\beta$.

In general, the transformation between two curvilinear basis follows the same rule. Consider, for example, the equivalence:

$$\mathbf{E} = \mathrm{E}_{\alpha\beta}\, \mathbf{G}^\alpha \otimes \mathbf{G}^\beta = \mathrm{E}^{\alpha\beta}\, \mathbf{G}_\alpha \otimes \mathbf{G}_\beta \;. \tag{A.3}$$

Again, by multiplying the left- and right-hand side of Equation (A.1) by $\mathbf{G}^\kappa$ and $\mathbf{G}^\gamma$:

$$\mathrm{E}_{\alpha\beta} \left(\mathbf{G}^\kappa \cdot \mathbf{G}^\alpha\right) \left(\mathbf{G}^\beta \cdot \mathbf{G}^\gamma\right) = \mathrm{E}^{\kappa\gamma} \;, \tag{A.4}$$

where the equation is simplified due to the orthogonality property of reciprocal basis $\mathbf{G}^{\beta} \cdot \mathbf{C}_{\gamma} = \delta^{\beta}_{\gamma}$. In a similar way, it is possible to derive all the following transformation rules:

$$\begin{aligned}
\mathrm{E}^{\alpha\beta}\left(\mathbf{G}^{\kappa} \cdot \mathbf{G}_{\alpha}\right)\left(\mathbf{G}_{\beta} \cdot \mathbf{G}^{\gamma}\right) &= \mathrm{E}^{\kappa\gamma}\ , \\
\mathrm{E}^{\alpha\beta}\left(\mathbf{G}_{\kappa} \cdot \mathbf{G}_{\alpha}\right)\left(\mathbf{G}_{\beta} \cdot \mathbf{G}_{\gamma}\right) &= \mathrm{E}_{\kappa\gamma}\ , \\
\mathrm{E}_{\alpha\beta}\left(\mathbf{G}_{\kappa} \cdot \mathbf{G}^{\alpha}\right)\left(\mathbf{G}^{\beta} \cdot \mathbf{G}^{\gamma}\right) &= \mathrm{E}_{\kappa\gamma}\ .
\end{aligned} \tag{A.5}$$

A.2 Simplification of the cohesive variational form

Equation (3.24) involves the dot products $\delta\delta_n \cdot \delta_n$ and $\delta\delta_\tau \cdot \delta_\tau$, which may be expressed as:

$$\begin{aligned}
\delta\delta_n \cdot \delta_n &= \delta\left[\left(\tilde{\mathbf{n}} \otimes \tilde{\mathbf{n}}\right)\delta\right]^{\mathrm{T}}\left(\tilde{\mathbf{n}} \otimes \tilde{\mathbf{n}}\right)\delta \\
&\approx \delta\delta^{\mathrm{T}}\left(\tilde{\mathbf{n}} \otimes \tilde{\mathbf{n}}\right)^{\mathrm{T}}\left(\tilde{\mathbf{n}} \otimes \tilde{\mathbf{n}}\right)\delta \\
&= \delta\delta^{\mathrm{T}}\left(\tilde{\mathbf{n}} \otimes \tilde{\mathbf{n}}\right)\delta \\
&= \delta\delta \cdot \delta_n\ ,
\end{aligned} \tag{A.6}$$

and

$$\begin{aligned}
\delta\delta_\tau \cdot \delta_\tau &= \delta\left[\left(\mathbf{I} - \tilde{\mathbf{n}} \otimes \tilde{\mathbf{n}}\right)\delta\right]^{\mathrm{T}}\left(\mathbf{I} - \tilde{\mathbf{n}} \otimes \tilde{\mathbf{n}}\right)\delta \\
&\approx \delta\delta^{\mathrm{T}}\left(\mathbf{I} - \tilde{\mathbf{n}} \otimes \tilde{\mathbf{n}}\right)^{\mathrm{T}}\left(\mathbf{I} - \tilde{\mathbf{n}} \otimes \tilde{\mathbf{n}}\right)\delta \\
&= \delta\delta^{\mathrm{T}}\left[\mathbf{I}^{\mathbf{T}}\mathbf{I} - 2\mathbf{I}^{\mathrm{T}}\left(\tilde{\mathbf{n}} \otimes \tilde{\mathbf{n}}\right) + \left(\tilde{\mathbf{n}} \otimes \tilde{\mathbf{n}}\right)^{\mathrm{T}}\left(\tilde{\mathbf{n}} \otimes \tilde{\mathbf{n}}\right)\right]\delta \\
&= \delta\delta \cdot \left(\mathbf{I} - \tilde{\mathbf{n}} \otimes \tilde{\mathbf{n}}\right)\delta \\
&= \delta\delta \cdot \delta_\tau\ ,
\end{aligned} \tag{A.7}$$

where, going from first to second line, we neglect the variation of the equivalent normal vector.

A.3 Variation of the normal vector

In what follows we make use of the Einstein summation convention. In the current configuration, the unit outward normal vector $\mathbf{n}$ coincides with the third covariant basis vector $\mathbf{g}_3$ given by

Eq. (2.14). As a result, the variation $\delta\mathbf{n}$ may be computed as follows:

$$\begin{aligned}\delta\mathbf{n} &= \delta\left(\frac{\mathbf{x}_{,\xi_1}\times\mathbf{x}_{,\xi_2}}{\|\mathbf{x}_{,\xi_1}\times\mathbf{x}_{,\xi_2}\|}\right)\\ &= \frac{\delta\left(\mathbf{x}_{,\xi_1}\times\mathbf{x}_{,\xi_2}\right)\|\mathbf{x}_{,\xi_1}\times\mathbf{x}_{,\xi_2}\| - \left(\mathbf{x}_{,\xi_1}\times\mathbf{x}_{,\xi_2}\right)\delta\|\mathbf{x}_{,\xi_1}\times\mathbf{x}_{,\xi_2}\|}{\|\mathbf{x}_{,\xi_1}\times\mathbf{x}_{,\xi_2}\|^2}\\ &= \frac{\left(\delta\mathbf{x}_{,\xi_1}\times\mathbf{x}_{,\xi_2}\right)+\left(\mathbf{x}_{,\xi_1}\times\delta\mathbf{x}_{,\xi_2}\right)}{\|\mathbf{x}_{,\xi_1}\times\mathbf{x}_{,\xi_2}\|}\\ &\quad - \left(\mathbf{x}_{,\xi_1}\times\mathbf{x}_{,\xi_2}\right)\frac{\left(\delta\mathbf{x}_{,\xi_1}\times\mathbf{x}_{,\xi_2}\right)+\left(\mathbf{x}_{,\xi_1}\times\delta\mathbf{x}_{,\xi_2}\right)}{\|\mathbf{x}_{,\xi_1}\times\mathbf{x}_{,\xi_2}\|^3}\ .\end{aligned} \tag{A.8}$$

The cross product is expressed using index notation by taking advantage of the Levi–Civita symbol ϵ_{klm} as:

$$\mathbf{a}\times\mathbf{b} = \epsilon_{klm}a_l b_m \boldsymbol{e}_k\ . \tag{A.9}$$

Therefore, the variation $\delta\mathbf{n}$ may be expressed using index notation as:

$$\delta\mathrm{n}_k = \frac{1}{\|\epsilon_{pqr}\mathrm{x}_{q,\xi_2}\mathrm{x}_{r,\xi_1}\|}\left(\mathrm{I}_{kj}-\mathrm{n}_k\mathrm{n}_j\right)\left[\left(\epsilon_{jil}\mathrm{x}_{l,\xi_2}\delta\mathrm{x}_{i,\xi_1}\right)+\left(\epsilon_{jli}\mathrm{x}_{l,\xi_1}\delta\mathrm{x}_{i,\xi_2}\right)\right]\ , \tag{A.10}$$

where $\mathbf{I}$ is the identity matrix. The derivatives of the coordinate vector $\mathbf{x}_{,\xi_\alpha}$ can be expressed in terms of the derivatives of the shape function by introducing the IGA discretization:

$$\mathrm{x}_{i,\xi_\alpha} = \sum_{A=1}^{n_{sh}}\mathrm{N}_{A,\xi_\alpha}\mathrm{d}_{A_i}\ . \tag{A.11}$$

Finally, the derivative of the *k-th* component of the normal vector $\mathbf{n}$ w.r.t. the degree of freedom d_{A_i} is

$$\begin{aligned}\frac{\partial\mathrm{n}_k}{\partial\mathrm{d}_{A_i}} &= \frac{1}{\|\epsilon_{pqr}\mathrm{x}_{q,\xi_2}\mathrm{x}_{r,\xi_1}\|}\left(\mathrm{I}_{kj}-\mathrm{n}_k\mathrm{n}_j\right)\left(\epsilon_{jil}\mathrm{x}_{l,\xi_2}\frac{\partial\mathrm{x}_{i,\xi_1}}{\partial\mathrm{d}_{A_i}}\right)\\ &\quad+\frac{1}{\|\epsilon_{pqr}\mathrm{x}_{q,\xi_2}\mathrm{x}_{r,\xi_1}\|}\left(\mathrm{I}_{kj}-\mathrm{n}_k\mathrm{n}_j\right)\left(\epsilon_{jli}\mathrm{x}_{l,\xi_1}\frac{\partial\mathrm{x}_{i,\xi_2}}{\partial\mathrm{d}_{A_i}}\right)\ .\end{aligned} \tag{A.12}$$

In order to simplify notation, we introduce the terms:

$$\begin{aligned}\mathrm{A}_{ki} &= \frac{1}{\|\epsilon_{pqr}\mathrm{x}_{q,\xi_2}\mathrm{x}_{r,\xi_1}\|}\left(\mathrm{I}_{kj}-\mathrm{n}_k\mathrm{n}_j\right)\left(\epsilon_{jil}\mathrm{x}_{l,\xi_2}\right)\ ,\\ \mathrm{B}_{ki} &= \frac{1}{\|\epsilon_{pqr}\mathrm{x}_{q,\xi_2}\mathrm{x}_{r,\xi_1}\|}\left(\mathrm{I}_{kj}-\mathrm{n}_k\mathrm{n}_j\right)\left(\epsilon_{jli}\mathrm{x}_{l,\xi_1}\right)\ ,\end{aligned} \tag{A.13}$$

and compactly rewrite the derivative of the normal vector as:

$$\frac{\partial\mathrm{n}_k}{\partial\mathrm{d}_{A_i}} = \mathrm{A}_{ki}\mathrm{N}_{A,\xi_1}+\mathrm{B}_{ki}\mathrm{N}_{A,\xi_2}\ . \tag{A.14}$$

A.4 Integration over the cohesive interface

Transformation of integrals from the physical to parametric domain requires the evaluation of the surface Jacobian J^{Γ^S} that is given by

$$J^{\Gamma^S} = \|\mathbf{x}_{,\xi_1} \times \mathbf{x}_{,\xi_2}\| \,. \tag{A.15}$$

Analogously, the transformation of the integrals over the the cohesive interface requires the evaluation of the surface Jacobian $J^{\Gamma^{\mathrm{coh}}}$ that is given by

$$J^{\Gamma^{\mathrm{coh}}} = ||\mathbf{x}^{\mathrm{P}}_{,\xi_1} \times \mathbf{x}^{\mathrm{P}}_{,\xi_2}|| \,, \tag{A.16}$$

where $\mathbf{x}^{\mathrm{P}}$ is defined according to Eq. (3.29). We introduce Eq. (3.29) into Eq. (A.16) and compute:

$$\begin{aligned}
\mathbf{x}^{\mathrm{P}}_{,\xi_1} \times \mathbf{x}^{\mathrm{P}}_{,\xi_2} &= \left(\mathbf{x}_{,\xi_1} + \frac{h_{\Gamma^S}}{2}\mathbf{n}_{,\xi_1}\right) \times \left(\mathbf{x}_{,\xi_2} + \frac{h_{\Gamma^S}}{2}\mathbf{n}_{,\xi_2}\right) \\
&= \mathbf{x}_{,\xi_1} \times \mathbf{x}_{,\xi_2} + \frac{h_{\Gamma^S}}{2}\left(\mathbf{x}_{,\xi_1} \times \mathbf{n}_{,\xi_2} + \mathbf{n}_{,\xi_1} \times \mathbf{x}_{,\xi_2}\right) + \frac{h^2_{\Gamma^S}}{4}\left(\mathbf{n}_{,\xi_1} \times \mathbf{n}_{,\xi_2}\right) \\
&= \mathbf{x}_{,\xi_1} \times \mathbf{x}_{,\xi_2} + \frac{h_{\Gamma^S}}{2}\left(-\mathbf{x}_{,\xi_1\xi_2} \times \mathbf{n} - \mathbf{n} \times \mathbf{x}_{,\xi_1\xi_2}\right) + \frac{h^2_{\Gamma^S}}{4}\left(\mathbf{n}_{,\xi_1} \times \mathbf{n}_{,\xi_2}\right) \\
&= \mathbf{x}_{,\xi_1} \times \mathbf{x}_{,\xi_2} + \frac{h^2_{\Gamma^S}}{4}\left(\mathbf{n}_{,\xi_1} \times \mathbf{n}_{,\xi_2}\right) \,.
\end{aligned} \tag{A.17}$$

The above equation implies

$$\mathbf{x}^{\mathrm{P}}_{,\xi_1} \times \mathbf{x}^{\mathrm{P}}_{,\xi_2} = \mathbf{x}_{,\xi_1} \times \mathbf{x}_{,\xi_2} + \mathcal{O}(h^2_{\Gamma^S}) \,, \tag{A.18}$$

which gives the following relationship between the surface Jacobians,

$$J^{\Gamma^{\mathrm{coh}}} = J^{\Gamma^S} + \mathcal{O}(h^2_{\Gamma^S}) \approx J^{\Gamma^S} \,, \tag{A.19}$$

and justifies performing the integration of the cohesive-interface terms over the corresponding shell midsurface.

A.5 Comparison of strain-smoothing and damage-smoothing formulations

Reference [35] discusses a family of gradient damage models in which damage variable rather than strain is smoothed by a PDE. Such models closely-resemble the phase field fracture models that have recently become popular, and a thorough comparison is made in [35]. However, as suggested by Jirásek's earlier work on strongly-nonlocal models [62], damage smoothing may give rise to a "stress locking" phenomenon, in which the material is incapable of complete failure, thus limiting the model's range of applicability. For additional discussion on strong and weak models and effects of different smoothing schemes, see [9]. The results presented in this appendix indicate that Jirásek's conclusions apply also to weakly-nonlocal damage-smoothing models.

In particular, we consider a damage-smoothing formulation that softens material using smoothed damage indices $\{\widetilde{d}_\aleph\}$, $\aleph \in \{1,2,6\}$, satisfying the PDEs: Find $\widetilde{d}_\aleph \in \mathcal{V}_d$, $\aleph \in \{1,2,6\}$, such that, for all $s_\aleph \in \mathcal{V}_d$,

$$\int_{\Gamma_0} \left(c\widetilde{d}_{\aleph,\alpha}\, G^{\alpha\beta} s_{\aleph,\beta} + \left(\widetilde{d}_\aleph - d_\aleph\right) s_\aleph \right)\, d\Gamma_0 = 0\,, \tag{A.20}$$

where $\{d_\aleph\}$ are the locally-computed damage indices from the formulation of [14] and the space $\mathcal{V}_d$ of trial and test functions is *scalar*-valued, i.e., $\aleph$ does not refer to a 2D (Greek letter) or 3D (Roman letter) tensor index. As in the strain-smoothing case, we discretize the PDEs (A.20) by Galerkin's method and couple them with the displacement subproblem in a staggered fashion.

In case the Gradient-Enhanced method is used to regularize damage variables, Cartesian components of the local strain tensor $\overline{\mathrm{E}}_{\alpha\beta}$ replace their smooth counterpart in the definition of equivalent displacements $\hat{\delta}_i$ in Equations (5.22), as described in [14]. The definition of tangent moduli in the residual-stiffness approach [14, Section 3] is also modified and the material stiffness matrix $\widetilde{\mathbf{C}}$, expressed in local material axes, is parametrized as a function of nonlocal damage variables computed from (A.20):

$$\widetilde{\mathbf{C}} = \frac{1}{D} \begin{bmatrix} E_1\left(1-\widetilde{d}_1\right) & E_1\nu_{21}\left(1-\widetilde{d}_1\right)\left(1-\widetilde{d}_2\right) & 0 \\ E_1\nu_{21}\left(1-\widetilde{d}_1\right)\left(1-\widetilde{d}_2\right) & E_2\left(1-\widetilde{d}_2\right) & 0 \\ 0 & 0 & G_{12}D\left(1-\widetilde{d}_6\right) \end{bmatrix}, \tag{A.21}$$

where $D = 1 - \nu_{21}\nu_{12}\left(1-\widetilde{d}_1\right)\left(1-\widetilde{d}_2\right)$. In case of isotropic constitutive law, all the components of the tensor of tangent moduli are scaled proportionally to a single isotropic damage variable. It follows that:

$$\mathbf{S} = \left(1 - \widetilde{d}_{\mathrm{iso}}\right) \mathbf{C} : \mathbf{E}\,. \tag{A.22}$$

In order to compare differences, we apply the modified Gradient-Enhance model (A.20) to simulate the uniaxial tensile test presented in Section 5.5.2. Two discretization of 80 and 160 elements are considered and quadratic C^1 NURBS are used as shape functions. The smoothing parameter c is set equal to 1 mm^2. Results obtained numerical analysis are shown in Figure A.2 and A.1. The distribution of $\widetilde{d}_{\mathrm{iso}}$ as a function of the axial coordinates shows that, compared to the *local* counterpart, the smooth damage variable does not reach the limit of one anywhere in the bar.

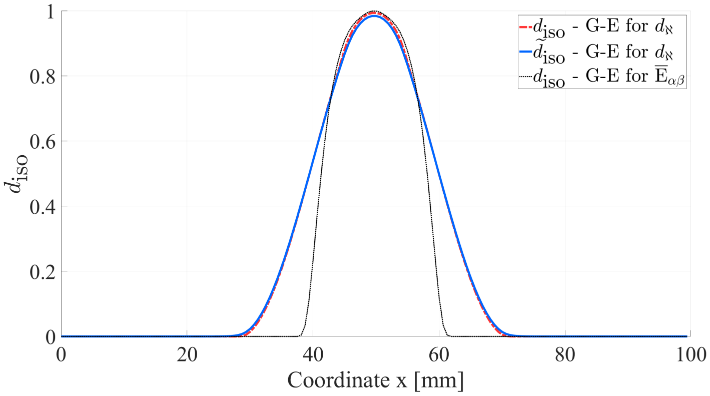

Figure A.1: Uniaxial tensile test: Gradient-Enhanced nonlocal regularization. Distribution of the (d_{iso}) local and ($\widetilde{d}_{\mathrm{iso}}$) nonlocal isotropic damage variable obtained using the modified Gradient-Enhanced on a mesh of 160 elements. Results obtained for an applied displacement $\Delta = 0.045$ mm. Result from the baseline Gradient-Enhanced method is reported for comparison.

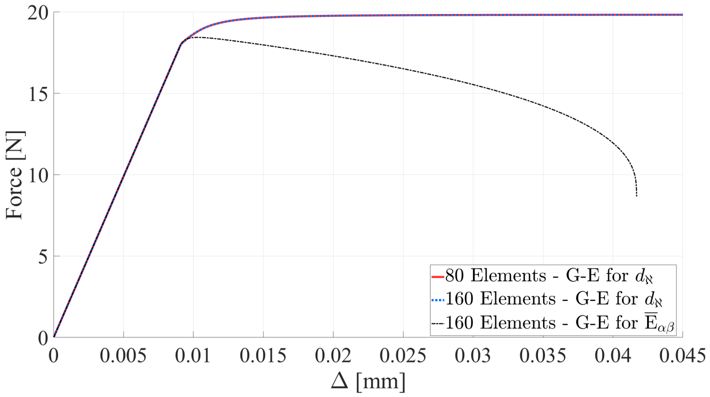

Figure A.2: Uniaxial tensile test: Gradient-Enhanced nonlocal regularization. Force-displacement curves obtained using the modified Gradient-Enhanced method. Result from the baseline Gradient-Enhanced method is reported for comparison.

While the damage area extend for a larger portion of the domain, the force-displacement curve does not exhibit the expected strain-softening response. These results corroborate the stress-locking effect predicted in [62].

A.6 Acknowledgments

The Appendix is, in full, an edited reprint of the material as it appears in:

- *"A new multi-layer approach for progressive damage simulation in composite laminates based on isogeometric analysis and Kirchhoff–Love shells. Part I: basic theory and modeling of delamination and transverse shear"*, published on-line in *"Computational Mechanics"* on November 30th 2017

and co-authored by *Marco S. Pigazzini, Yuri Bazilevs, Andrew C. Ellison, and Hyonny Kim*. This article is currently in press. The author of this dissertation *(Marco S. Pigazzini)* is the primary investigator and author of this paper.

- *"A new multi-layer approach for progressive damage simulation in composite laminates based on isogeometric analysis and Kirchhoff–Love shells. Part II: impact modeling"*, published on-line in *"Computational Mechanics"* on November 24^{th} 2017 and co-authored by *Marco S. Pigazzini, Yuri Bazilevs, Andrew C. Ellison, and Hyonny Kim*. This article is currently in press. The author of this dissertation *(Marco S. Pigazzini)* is the primary investigator and author of this paper.
- *"Gradient-enhanced damage modeling in Kirchhoff–Love shells: Application to isogeometric analysis of composite laminates"*. This manuscript in preparation is co-authored by *Marco S. Pigazzini, David Kamensky, Dennis A. P. van Iersel, Joris J.C. Remmers, and Yuri Bazilevs*. The author of this dissertation *(Marco S. Pigazzini)* is the primary investigator and author of this paper.

Bibliography

[1] O. Allix and P. Ladevéze. Interlaminar interface modelling for the prediction of delamination. *Composite Structures*, 22:235–242, 1992.

[2] O. Allix, P. Ladevéze, and A. Corigliano. Damage analysis of interlaminar fracture specimens. *Composite Structures*, 31:61–74, 1995.

[3] M. Ambati, T. Gerasimov, and L. De Lorenzis. A review on phase-field models of brittle fracture and a new fast hybrid formulation. *Computational Mechanics*, 55(2):383–405, 2015.

[4] F. Amiri, D. Millán, Y. Shen, T. Rabczuk, and M. Arroyo. Phase-field modeling of fracture in linear thin shells. *Theoretical and Applied Fracture Mechanics*, 69(Supplement C):102–109, 2014. Introducing the new features of Theoretical and Applied Fracture Mechanics through the scientific expertise of the Editorial Board.

[5] P. Areias, T. Rabczuk, and M. A. Msekh. Phase-field analysis of finite-strain plates and shells including element subdivision. *Computer Methods in Applied Mechanics and Engineering*, 312(Supplement C):322–350, 2016. Phase Field Approaches to Fracture.

[6] F. Auricchio, L. Beirao da Veiga, T.J.R. Hughes, A. Reali, and G. Sangalli. Isogeometric collocation for elastostatics and explicit dynamics. *Computer Methods in Applied Mechanics and Engineering*, 249-252:2–14, 2012.

[7] I. Babuška and J. T. Oden. Verification and validation in computational engineering and science: basic concepts. *Computer Methods in Applied Mechanics and Engineering*, 193(36–38):4057–4066, 2004.

[8] E.J. Barbero. *Finite Element Analysis of Composite Materials Using Abaqus*. CRC Press, 2013.

[9] Z. P. Bažant and M. Jirásek. Nonlocal integral formulations of plasticity and damage: Survey of progress. *Journal of Engineering Mechanics*, 128(11):1119–1149, 2002.

[10] Z. P. Bažant and B.H. Oh. Crack band theory for fracture of concrete. *Materials and Structures*, 16:155–177, 1983.

[11] Z. P. Bažant and G. Pijaudier-Cabot. Nonlocal continuum damage, localization instability and convergence. *Journal of Applied Mechanics*, 55:287–293, 1988.

[12] Y. Bazilevs, V. M. Calo, J. A. Cottrell, J. A. Evans, T. J. R. Hughes, S. Lipton, M. A. Scott, and T. W. Sederberg. Isogeometric analysis using T-splines. *Computer Methods in Applied Mechanics and Engineering*, 199:229–263, 2010.

[13] Y. Bazilevs, M.-C. Hsu, and M. A. Scott. Isogeometric fluid–structure interaction analysis with emphasis on non-matching discretizations, and with application to wind turbines. *Computer Methods in Applied Mechanics and Engineering*, 249-252:28–41, 2012.

[14] Y. Bazilevs, M. S. Pigazzini, A. Ellison, and H. Kim. A new multi-layer approach for progressive damage simulation in composite laminates based on isogeometric analysis and kirchhoff–love shells. Part I: Basic theory and modeling of delamination and transverse shear. *Computational Mechanics*, –:–, 2017. In press.

[15] Y. Bazilevs, K. Takizawa, and T. E. Tezduyar. *Computational fluid-structure interaction: Methods and applications*. Wiley, 2013.

[16] D.J. Benson, Y. Bazilevs, M.-C. Hsu, and T.J.R. Hughes. Isogeometric shell analysis: the Reissner–Mindlin shell. *Computer Methods in Applied Mechanics and Engineering*, 199:276–289, 2010.

[17] D.J. Benson, Y. Bazilevs, M.-C. Hsu, and T.J.R. Hughes. A large deformation, rotation-free, isogeometric shell. *Computer Methods in Applied Mechanics and Engineering*, 200:1367–1378, 2011.

[18] M.L. Benzeggagh and M. Kenane. Measurement of mixed-mode delamination fracture toughness of unidirectional glass/epoxy composites with mixed-mode bending apparatus. *Composites Science and Technology*, 56:439–449, 1996.

[19] M. Bischoff, K.U. Bletzinger, W.A. Wall, and E. Ramm. Models and finite elements for thin-walled structures. *Encyclopedia of Computational Mechanics*, 2:59–137, 2004.

[20] M. J. Borden, C. V. Verhoosel, M. A. Scott, T. J. R. Hughes, and C. M. Landis. A phase-field description of dynamic brittle fracture. *Computer Methods in Applied Mechanics and Engineering*, 217–220:77–95, 2012.

[21] C. Bouvet, S. Rivallant, and J.J. Barrau. Low velocity impact modeling in composite laminates capturing permanent indentation. *Composites Science and Technology*, 72:19771988, 2012.

[22] A. Buffa, J. Rivas, G. Sangalli, and R. Vázquez. Isogeometric discrete differential forms in three dimensions. *SIAM Journal on Numerical Analysis*, 49(2):818–844, 2011.

[23] A. Buffa, G. Sangalli, and R. Vázquez. Isogeometric analysis in electromagnetics: B-splines approximation. *Computer Methods in Applied Mechanics and Engineering*, 199(17):1143–1152, 2010.

[24] P.P. Camanho, C.G. Dàvila, and F.M. de Moura. Numerical simulation of mixed-mode progressive delamination in composite materials. *Journal of Composite Materials*, 37(16):1415–1438, 2003.

[25] A. Carpinteri. Softening and snap-back instability in cohesive solids. *International Journal for Numerical Methods in Engineering*, 28:1521–1537, 1989.

[26] N.V. De Carvalho, B.Y. Chen, S.T. Pinho, J.G. Ratcliffe, P.M. Baiz, and T.E. Tay. Modeling delamination migration in cross-ply tape laminates. *Composites: Part A*, 71:192–203, 2015.

[27] J.L. Chaboche. Continuum damage mechanics: Present state and future trends. *Nuclear Engineering and Design*, 105:19–33, 1987.

[28] J. F. Chen, E. V. Morozov, and K. Shankar. A combined elastoplastic damage model for progressive failure analysis of composite materials and structures. *Composite Structures*, 94(12):3478–3489, 2012.

[29] H.Y. Choi and F.-K. Chang. A model for predicting damage in graphite/epoxy laminated composites resulting from low-velocity point impact. *Journal of Composite Materials*, 26(14):2134–2169, 1992.

[30] H.Y. Choi, R.J. Downs, and F.-K. Chang. A new approach toward understanding damage mechanisms and mechanics of laminated composites due to low-velocity impact: part I-experiments. *Journal of Composite Materials*, 25:992–1011, 1991.

[31] J. Chung and G. M. Hulbert. A time integration algorithm for structural dynamics with improved numerical dissipation: The generalized-α method. *Journal of Applied Mechanics*, 60:371–75, 1993.

[32] J. A. Cottrell, T. J. R. Hughes, and Y. Bazilevs. *Isogeometric Analysis. Toward Integration of CAD and FEA*. Wiley, 2009.

[33] C.G. Dàvila and P.P. Camanho. Failure criteria for FRP laminates in plane stress. Technical Report NASA/TM-2003-212663, Langley Research Center, Hampton, Virginia, November 2003.

[34] C.G. Dàvila, P.P. Camanho, and A. Turon. Cohesive elements for shells. Technical Report 214869, NASA Langley Research Center, 2007.

[35] R. de Borst and C. V. Verhoosel. Gradient damage vs phase-field approaches for fracture: Similarities and differences. *Computer Methods in Applied Mechanics and Engineering*, 312:78–94, 2016.

[36] X. Deng, A. Korobenko, J. Yan, and Y. Bazilevs. Isogeometric analysis of continuum damage in rotation-free composite shells. *Computer Methods in Applied Mechanics and Engineering*, 284:349–372, 2015.

[37] M.V. Donadon, L. Iannucci, B.G. Falzon, J.M. Hodgkinson, and S.F.M. de Almeida. A progressive failure model for composite laminates subjected to low velocity impact damage. *Computers and Structures*, 86:12321252, 2008.

[38] G. Duvaut and J.L. Lions. *Inequalities in Mechanics and Physics*. Springer Berlin Heidelberg, 1976.

[39] A. Ellison and H. Kim. Computed tomography informed composite damage state model generation. *Journal of Composite Materials*, –:–, 2018. In press.

[40] J. A. Evans. *Divergence-free B-spline Discretizations for Viscous Incompressible Flows*. Ph.D. thesis, University of Texas at Austin, Austin, Texas, United States, 2011.

[41] A. Faggiani and B.G. Falzon. Predicting low-velocity impact damage on a stiffened composite panel. *Composite: Part A*, 41:737–749, 2010.

[42] M.L. Falk, A. Needleman, and J.R. Rice. A critical evaluation of cohesive zone models of dynamic fracture. *Journal de Physique IV*, 11:43–50, 2001.

[43] Z. Guan and C. Yang. Low-velocity impact and damage process of composite laminates. *Journal of Composite Materials*, 36(7):851–871, 2002.

[44] P. Hansbo, M. G. Larson, and K. Larsson. Analysis of Finite Element Methods for Vector Laplacians on Surfaces. *ArXiv e-prints*, October 2016.

[45] P.W. Harper and S.R. Hallett. Cohesive zone length in numerical simulations of composite delamination. *Engineering Fracture Mechanics*, 75:4774–4792, 2008.

[46] Z. Hashin. Failure criteria for unidirectional fiber composites. *Journal of Applied Mechanics*, 47:329–334, 1980.

[47] Z. Hashin and A. Rotem. A fatigue failure criterion for fiber-reinforced materials. *Journal of Composite Materials*, 7:448–464, 1973.

[48] H.B. Hellweg and M.A. Crisfield. A new arc-length method for handling sharp snap-backs. *Computers & Structures*, 66(5):704709, 1998.

[49] H. M. Hilber, T. J. R. Hughes, and R. L. Taylor. Improved numerical dissipation for time integration algorithms in structural dynamics. *Earthquake Engineering and Structural Dynamics*, 5:283–292, 1977.

[50] N. Hongkarnjanakul, C. Bouvet, and S. Rivallant. Validation of low velocity impact modelling on different stacking sequences of CFRP laminates and influence of fibre failure. *Composite Structures*, 106:549–559, 2013.

[51] S. Hosseini, J. J. C. Remmers, and R. de Borst. The incorporation of gradient damage models in shell elements. *Computer Methods in Applied Mechanics and Engineering*, 98:391–398, 2014.

[52] S. Hosseini, J.J.C. Remmers, C.V. Verhoosel, and R. de Borst. An isogeometric solid-like shell element for non-linear analysis. *International Journal for Numerical Methods in Engineering*, 95:238–256, 2013.

[53] S. Hosseini, J.J.C. Remmers, C.V. Verhoosel, and R. de Borst. An isogeometric continuum shell element for non-linear analysis. *Computer Methods in Applied Mechanics and Engineering*, 271:1–22, 2014.

[54] S. Hosseini, J.J.C Remmers, C.V. Verhoosel, and R. de Borst. Propagation of delamination in composite materials with isogeometric continuum shell elements. *International Journal for Numerical Methods in Engineering*, 102:159–179, 2015.

[55] M.-C. Hsu, D. Kamensky, Y. Bazilevs, M. S. Sacks, and T. J. R. Hughes. Fluid–structure interaction analysis of bioprosthetic heart valves: significance of arterial wall deformation. *Computational Mechanics*, 54:1055–1071, 2014.

[56] M.-C. Hsu, C. Wang, A. J. Herrema, D. Schillinger, A. Ghoshal, and Y. Bazilevs. An interactive geometry modeling and parametric design platform for isogeometric analysis. *Computers and Mathematics with Applications*, 70:1481–1500, 2015.

[57] T. J. R Hughes. *The Finite Element Method. Linear Static and Dynamic Finite Element Analysis*. Prentice-Hall, Englewood Cliffs, New Jersey, 1987.

[58] T. J. R. Hughes, J. A. Cottrell, and Y. Bazilevs. Isogeometric analysis: CAD, finite elements, NURBS, exact geometry, and mesh refinement. *Computer Methods in Applied Mechanics and Engineering*, 194:4135–4195, 2005.

[59] ABAQUS Inc. *ABAQUS 2016 User's manual*. Providence, RI, USA, 2016.

[60] T. Jankuhn, M. A. Olshanskii, and A. Reusken. Incompressible fluid problems on embedded surfaces: Modeling and variational formulations. *ArXiv e-prints*, February 2017.

[61] W.-G. Jiang, S.R. Hallett, B.G. Green, and M.R. Wisnom. A concise interface constitutive law for analysis of delamination and splitting in composite materials and its application to scaled notched tensile specimens. *International Journal for Numerical Methods in Engineering*, 69:1982–1995, 2007.

[62] M. Jirásek. Nonlocal models for damage and fracture: Comparison of approaches. *International Journal of Solids and Structures*, 35(31):4133–4145, 1998.

[63] F.A. Leone Jr. Deformation gradient tensor decomposition for representing matrix cracks in fiber-reinforced materials. *Composite: Part A*, 76:334–341, 2015.

[64] L.M. Kachanov. *Introduction to Continuum Damage Mechanics*. Springer Netherlands, 1986.

[65] D. Kamensky, M.-C. Hsu, D. Schillinger, J. A. Evans, A. Aggarwal, Y. Bazilevs, M. S. Sacks, and T. J. R. Hughes. An immersogeometric variational framework for fluid-structure interaction: Application to bioprosthetic heart valves. *Computer Methods in Applied Mechanics and Engineering*, 284:1005–1053, 2015.

[66] J. Kiendl, M. Ambati, L. De Lorenzis, H. Gomez, and A. Reali. Phase-field description of brittle fracture in plates and shells. *Computer Methods in Applied Mechanics and Engineering*, 312(Supplement C):374–394, 2016. Phase Field Approaches to Fracture.

[67] J. Kiendl, Y. Bazilevs, M.-C. Hsu, R. Wüchner, and Kai-Uwe Bletzinger. The bending strip method for isogeometric analysis of Kirchhoff–Love shell structures comprised of multiple patches. *Computer Methods in Applied Mechanics and Engineering*, 199:2403–2416, 2010.

[68] J. Kiendl, K.-U. Bletzinger, J. Linhard, and R. Wüchner. Isogeometric shell analysis with Kirchhoff–Love elements. *Computer Methods in Applied Mechanics and Engineering*, 198(49):3902–3914, 2009.

[69] J. Kiendl, M.-C. Hsu, M.C.H. Wu, and A. Reali. Isogeometric KirchhoffLove shell formulations for general hyperelastic materials. *Computer Methods in Applied Mechanics and Engineering*, 291:280–303, 2015.

[70] A. Korobenko, M.-C. Hsu, I. Akkerman, J. Tippmann, and Y. Bazilevs. Structural mechanics modeling and FSI simulation of wind turbines. *Mathematical Models and Methods in Applied Sciences*, 23:249–272, 2013.

[71] P. Ladevéze and E. Le Dantec. Damage modelling of the elementary ply for laminated composites. *Composites Science and Technology*, 43:257–267, 1992.

[72] I. Lapczyk and J. A. Hurtado. Progressive damage modeling in fiber-reinforced materials. *Composites: Part A*, 38:2333–2341, 2007.

[73] C. C. Long, A. L. Marsden, and Y. Bazilevs. Shape optimization of pulsatile ventricular assist devices using FSI to minimize thrombotic risk. *Computational Mechanics*, 54:921–932, 2014.

[74] J. E. Marsden and T. J. R. Hughes. *Mathematical Foundations of Elasticity*. Dover Civil and Mechanical Engineering Series. Dover, 1994.

[75] A. Matzenmiller, J. Lubliner, and R.B. Taylor. A constitutive model for anisotropic damage in fiber-composites. *Mechanics of Materials*, 20:125–152, 1995.

[76] R. McNeel and Associates. *Rhinoceros 5 User's Guide*. Seattle, WA, USA, 2014.

[77] Y. Mi, A. Crisfield, and G.A.O. Davies. Progressive delamination using interface elements. *Journal of Composite Materials*, 32(14):1246–1272, 1998.

[78] A. D. Nguyen, M. Stoffel, and D. Weichert. A gradient-enhanced damage approach for viscoplastic thin-shell structures subjected to shock waves. *Computer Methods in Applied Mechanics and Engineering*, 217-220(Supplement C):236–246, 2012.

[79] V.P. Nguyen, P.Kerfriden, and S.P.A. Bordas. Two-and three-dimensional isogeometric cohesive elements for composite delamination analysis. *Composites: Part B*, 60:193–212, 2014.

[80] R. H. J. Peerlings, W. A. M. Brekelmans, R. de Borst, and M. G. D. Geers. Gradient-enhanced damage modelling of high-cycle fatigue. *International Journal for Numerical Methods in Engineering*, 49(12):1547–1569, 2000.

[81] R. H. J. Peerlings, R. de Borst, W. A. M. Brekelmans, and M. G. D. Geers. Localisation issues in local and nonlocal continuum approaches to fracture. *European Journal of Mechanics - A/Solids*, 21(2):175–189, 2002.

[82] R.H.J. Peerlings, R. De Borst, W.A.M. Brekelmans, and J.H.P. De Vree. Gradient enhanced damage for quasi-brittle materials. *International Journal for Numerical Methods in Engineering*, 39:3391–3403, 1996.

[83] L. Piegl and W. Tiller. *The NURBS Book (Monographs in Visual Communication), 2nd ed.* Springer-Verlag, New York, 1997.

[84] M. S. Pigazzini, Y. Bazilevs, A. Ellison, and H. Kim. A new multi-layer approach for progressive damage simulation in composite laminates based on isogeometric analysis and kirchhoff–love shells. Part II: Impact modeling. *Computational Mechanics*, –:–, 2017. In press.

[85] Marco S. Pigazzini, Yuri Bazilevs, Andrew Ellison, and Hyonny Kim. Isogeometric analysis for simulation of progressive damage in composite laminates. *Journal of Composite Materials*, –:–, 2018. In press.

[86] G. Pijaudier-Cabot and Z. P. Bažant. Nonlocal damage theory. *Journal of Engineering Mechanics*, 113:1512–1533, 1987.

[87] S.T. Pinho, L. Iannucci, and P. Robinson. Physically-based failure models and criteria for laminated fibre-reinforced composites with emphasis on fibre kinking: part I: development. *Composites: Part A*, 37:6373, 2006.

[88] S.T. Pinho, L. Iannucci, and P. Robinson. Physically-based failure models and criteria for laminated fibre-reinforced composites with emphasis on fibre kinking: part II: FE implementation. *Composites: Part A*, 37:766777, 2006.

[89] A. Pucka and H. Schürmann. Failure analysis of FRP laminates by means of physically based phenomenological models. *Composites Science and Technology*, 62:16331662, 2002.

[90] J.N. Reddy. *Mechanics of Laminated Composite Plates and Shells: Theory and Analysis*. CRC Press, 2003.

[91] J.J.C. Remmers, G.N. Wells, and R. de Borst. A solid-like shell element allowing for arbitrary delaminations. *International Journal for Numerical Methods in Engineering*, 58:2013–2040, 2003.

[92] M.O.W. Richardson and M.J. Wisheart. Review of low-velocity impact properties of composite materials. *Composite: Part A*, 27A:1123–1131, 1996.

[93] S. Rivallant, C. Bouvet, and N. Hongkarnjanakul. Failure analysis of CFRP laminates subjected to compression after impact: fe simulation using discrete interface elements. *Composite: Part A*, 55:83–93, 2013.

[94] M. E. Rognes, D. A. Ham, C. J. Cotter, and A. T. T. McRae. Automating the solution of PDEs on the sphere and other manifolds in FEniCS 1.2. *Geoscientific Model Development*, 6(6):2099–2119, 2013.

[95] C.A. Rose, C.G. Dàvila, and F.A. Leone Jr. Analysis methods for progressive damage of composite structures. Technical Report 218024, NASA Langley Research Center, 2013.

[96] T. W. Sederberg, J. Zheng, A. Bakenov, and A. Nasri. T-splines and T-NURCCS. *ACM Transactions on Graphics*, 22(3):477–484, 2003.

[97] I. Shahid and F.-K Chang. An accumulative damage model for tensile and shear failures of laminated composite plates. *Journal of Composite Materials*, 29:926–981, 1995.

[98] S. A. Silling. Reformulation of elasticity theory for discontinuities and long-range forces. *Journal of the Mechanics and Physics of Solids*, 48(1):175–209, 2000.

[99] K. Takizawa, T. E. Tezduyar, and T. Terahara. Ram-air parachute structural and fluid mechanics computations with the space–time isogeometric analysis (ST-IGA). *Computers & Fluids*, 141:191–200, 2016.

[100] R. Talreja. Damage development in composites: mechanisms and modelling. *The Journal of Strain Analysis for Engineering Design*, 24(4):215–222, 1989.

[101] W. Tan, B.G. Falzon, L.N.S. Chiu, and M. Price. Predicting low velocity impact damage and Compression-After-Impact (CAI) behaviour of composite laminates. *Composites: Part A*, 71:212–226, 2015.

[102] I. Temizer, P. Wriggers, and T.J.R. Hughes. Three-dimensional mortar-based frictional contact treatment in isogeometric analysis with nurbs. *Computer Methods in Applied Mechanics and Engineering*, 209:115 – 128, 2012.

[103] A. Turon, P.P. Camanho, J. Costa, and C.G. Dàvila. A damage model for the simulation of delamination in advanced composites under variable-mode loading. *Mechanics of Materials*, 38:1072–1089, 2006.

[104] A. Turon, P.P. Camanho, J. Costa, and J. Renart. Accurate simulation of delamination growth under mixed-mode loading using cohesive elements: definition of interlaminar strengths and elastic stiffness. *Composite Structures*, 92:1857–1864, 2010.

[105] A. Turon, C.G. Dàvila, P.P. Camanho, and J. Costa. An engineering solution for mesh size effects in the simulation of selamination using cohesive zone models. *Engineering Fracture Mechanics*, 74:1665–1682, 2007.

[106] C. Wang, M. C.-H. Wu, F. Xu, M.-C. Hsu, and Y. Bazilevs. Modeling of a hydraulic arresting gear using fluid–structure interaction and isogeometric analysis. *Computers & Fluids*, 2015. Published online. doi:10.1016/j.compfluid.2015.12.004.

[107] P. Wriggers. Finite element algorithms for contact problems. *Archives of Computational Methods in Engineering*, 2:1–49, 1995.

[108] J. Xie, A.M. Waas, and M. Rassaian. Estimating the process zone length of fracture tests used in characterizing composites. *International Journal of Solids and Structures*, 100-101:111–126, 2016.

[109] J. Yan, B. Augier, A. Korobenko, J. Czarnowski, G. Ketterman, and Y. Bazilevs. FSI modeling of a propulsion system based on compliant hydrofoils in a tandem configuration. *Computers and Fluids*, 2015. Published online. doi:10.1016/j.compfluid.2015.07.013.

[110] J. Yan, A. Korobenko, X. Deng, and Y. Bazilevs. Computational free-surface fluid-structure interaction with application to floating offshore wind turbines. *Computers & Fluids*, 2016. Published online. doi:10.1016/j.compfluid.2016.03.008.

[111] Q.D. Yang and B.N. Cox. Cohesive models for damage evolution in laminated composites. *International Journal of Fracture*, 133:107–137, 2005.

[112] Q.D. Yang and B.N. Cox. Fracture length scales in human cortical bone: the necessity of nonlinear fracture models. *Biomaterials*, 27:2095–2113, 2006.

[113] Y. Zhang, P. Zhu, and X. Lai. Finite element analysis of low-velocity impact damage in composite laminated plates. *Materials and Design*, 27:513–519, 2006.